AN ABSTRACT OF THE THESIS OF

Kyle A. Rozman for the degree of

Master of Science in

Materials Science presented

on March 10, 2011

Title: Corrosion and Fatigue of Oil Well Drilling Steels

Abstract approved:

_____

Jamie J. Kruzic

Oil drilling requires that miles of steel drill pipe, called the drill string, be exposed to fatigue loading and corrosive environments. Furthermore, it has been reported that pitting corrosion is responsible for initiating catastrophic drillstring failure. Pitting corrosion is responsible for initiating fatigue cracks, with pits acting as local stress raisers. This project investigates the pitting corrosion susceptibility and influence on fatigue life of high strength low alloy drillstring steels S-135 and UD-165 in a simulated drilling completion fluid, 6.7 M $CaCl_2$.

Immersion test results show that both alloys are susceptible to pitting corrosion and a non-protective film of hydrated rust (FeOOH) was found. Non-metallic inclusions are well known to initiate pits in carbon steels. Preliminary testing of S-135 shows inclusions rich in Mn and S, while UD-165 shows inclusions rich in either Fe, Al and O, or Nb and C.

Potentiodynamic scans of both alloys show active dissolution. Cyclic voltrammetry results shows a repassivation potential in the cathodic region. Through potentiostatic testing pit growth was found to be independent of anodic polarization time, meaning pit growth was unachievable through anodic polarization. Shallow, wide pits (3-5μm deep, 10-50μm wide) were only observed after the potentiostatic anodic polarization.

Fatigue testing was performed on three surface treatments: 1) virgin 2) pitted by galvanostatic methods, and 3) pitted by galvanostatic methods, dried and left in the laboratory (20°C, 20-40% humidity) for 14 days. Statistical testing by Student's t-tests showed that UD-165 had a statistically significant drop in fatigue life for 1) virgin samples against 2) pitted samples while no significant drop was found for S-135. Both UD-165 and S-135 showed no statistically significant

drop in fatigue life for 1) virgin samples against 3) samples pitted and left in the laboratory for 14 days.

Corrosion and Fatigue of Oil Well Drilling Steels

by

Kyle A. Rozman

A THESIS

submitted to

Oregon State University

in partial fulfillment of

the requirements for the

degree of

Master of Science

Presented March 10, 2011

Commencement June 2011

<u>Master of Science</u> thesis of <u>Kyle A. Rozman</u> presented on <u>March 10, 2011</u>.

APPROVED:

_____

Major Professor, representing Materials Science

_____

Director of the Materials Science Program

_____

Dean of the Graduate School

I understand that my thesis will become part of the permanent collection of Oregon State University libraries. My signature below authorizes release of my thesis to any reader upon request.

_____

Kyle A. Rozman, Author

ACKNOWLEDGEMENTS

TABLE OF CONTENTS

TABLE OF CONTENTS (Continued)

TABLE OF CONTENTS (Continued)

TABLE OF CONTENTS (Continued)

LIST OF FIGURES

LIST OF FIGURES (Continued)

LIST OF FIGURES (Continued)

LIST OF FIGURES (Continued)

LIST OF FIGURES (Continued)

LIST OF EQUATIONS

LIST OF EQUATIONS (Continued)

LIST OF TABLES

1. INTRODUCTION

As fossil fuel resources are being depleted, new harder to reach wells are supplying the much needed fossil fuels. Methods such as ultra deep drilling (UDD) are being explored. UDD is a new method for the industry that brings new challenges.

Drilling started in a vertical manner. Due to environmental, political and economic reasons the oil industry has adopted extended reach drilling where the drill string departs thousands of feet in the horizontal direction from the initial drilling point. Extended reach drilling has helped decrease the total amount of drill sites. However oil resources are depleting and to recover new oil from the earth one must drill deeper into the earth's crust.

As one drills deeper into the earth's crust the ambient temperature and pressure increase. Offshore drilling is already experiencing temperatures of 250^oF (121^oC) and pressures of 10000 psi (69 MPa) at depths greater than 25000 feet (7.6 Km) (1). Elevated pressures and temperatures lead to accelerated corrosion, fatigue and stress corrosion cracking, all of which can lead to accelerated failure of drilling equipment.

Sour environments (containing H_2S in the operating environment) are also observed in high temperature and pressure environments. Hydrogen sulfide is a known contributor to Hydrogen Embrittlement (HE) and Sulfide Stress Cracking (SSC) which are special cases of, Environmentally Assisted Cracking (EAC). EAC is a phenomenon where catastrophic failure in materials can be attributed to the operating environment.

At depths of 25,000 feet of drill pipe, greater external pressures and higher temperature require increased strength drilling materials that can withstand corrosive, high pressure and high temperature environments. Often to make materials stronger, a sacrifice of ductility is encountered. Ductile materials will plastically deform before final fracture, opposed to brittle materials which tend to suddenly fracture.

Along with high strength and corrosion resistance it is desirable for materials to have high fracture toughness. Fracture toughness is a mechanical property that determines a materials resistance to fracture.

1.1 UDD Well

UDD wells are defined as wells greater than 25000 ft deep with a vertical displacement to horizontal departure ratio of less than 0.25 (2). UDD wells are typically drilled with High Strength Low Alloy (HSLA) steel drill pipes ranging in diameter from 5-12 inches and wall thicknesses of 0.375" to 2". At the bottom of a well one would find the bottom hole assembly which houses the drill bit that removes the earth. The bottom hole assembly is made of thicker pipe than the rest of the well and is left in compression to force the drill bit into the earth. The pipe above the bottom hole assembly is held in tension. If the greater than 5 mile long drill string was left to freely sit in the well, the pipe would buckle due to the enormous weight of the pipe. Because the drill pipes are held in tension to counteract the bucking force of gravity, UDD is a high tension low torsion drilling process (2). Figure 1 shows a diagram of a UDD well.
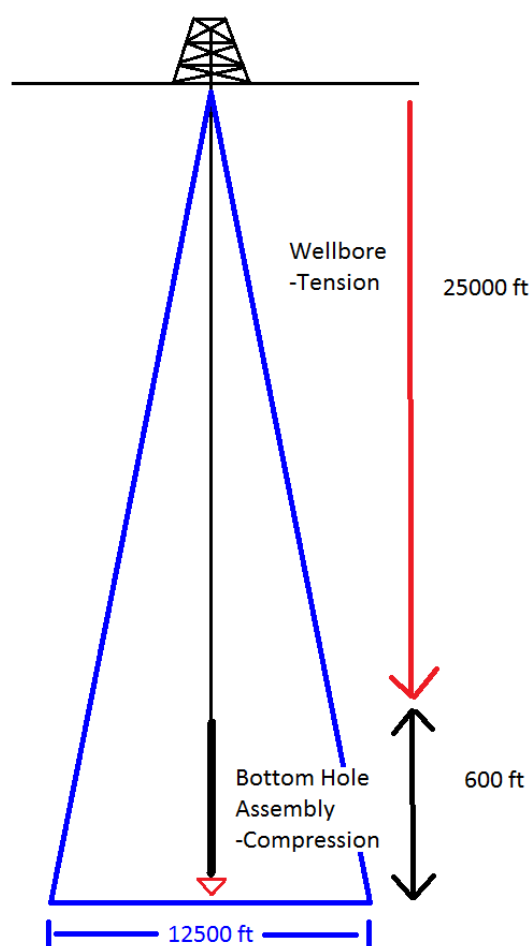
Figure 1- Diagram of a UDD Well

Drilling consists of concentric pipes: the static outer casing and rotating inner drill pipe. Drilling mud is pumped though the inner pipe and out the gap in-between the inner and outer pipe. The drilling mud lubricates the drill head and removes cuttings from the well. Figure 2 shows a diagram of a drillstring in operation.
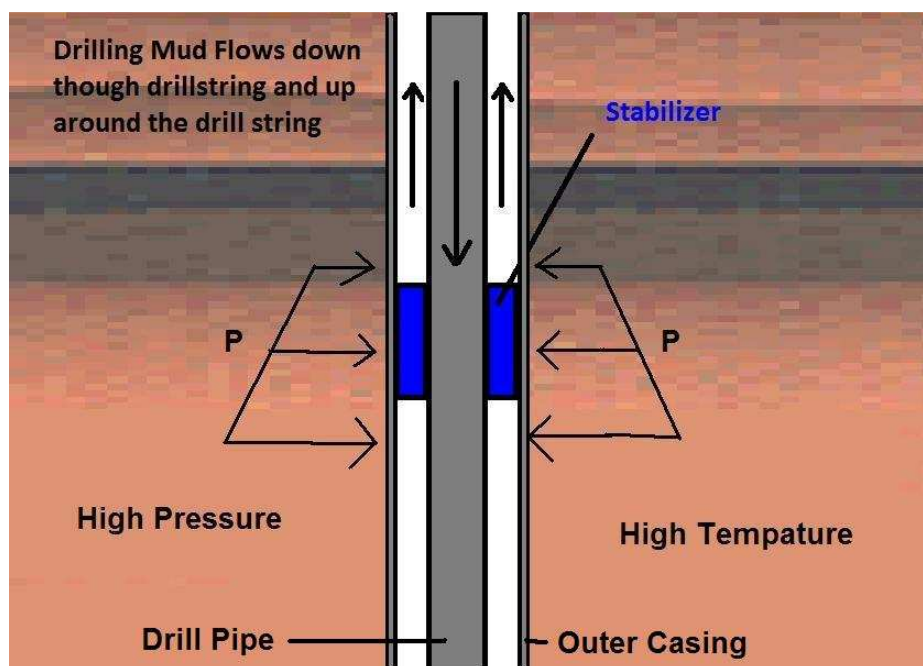
Figure 2 - Diagram of a drill string

Once the well has reached oil, the well is flushed out with a brine solution (saturated aqueous chloride ion), which removes particulate matter from the well which would damage pumps if not removed. However, brine solutions are highly corrosive and can initiate pitting corrosion on the surface of the drill pipes.

Multiple drill pipe sections fastened together make a drillstring. Drillstrings can be a few thousand feet in length to multiple ten thousands of feet in length. Drillstrings bend as necessary at approximately 3-5° per 100 ft of drillsting (3).
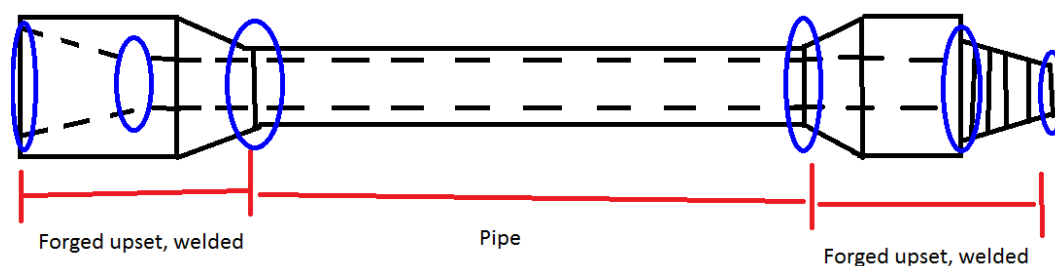
Figure 3 - Diagram of Drillpipe

Drillpipe sections are 30 feet long from threaded engagement to threaded engagement, with the male and female ends forged and friction welded to the pipe. Failure prone areas are circled in blue in Figure 3.

1.2 Materials Used to Drill Oil Wells

Historically, drilling has been done with steel pipe but other metals and composite materials have been investigated for drilling purposes. The American Petroleum Institute (API) was developed in World War I to insure the United States Armed Forces got petroleum products quickly and efficiently. The API worked to standardize drilling practices so oil could be acquired quickly and efficiently (4).

Carbon fiber drill pipes offer high strength to weight ratios, superior corrosion resistance, fatigue resistance and non-magnetic properties. However compared to steel pipe, carbon fiber alternative is about 3 times as expensive. To support the torsional loading in UDD carbon drill pipes may be up to 2x as thick as conventional steel pipes. This decreases the hydraulic efficiency of the carbon drill pipe significantly (2).

Titanium drill pipe is about 7-10x more expensive than conventional steel drill pipes, however titanium offers higher strength to weight ratios, good fatigue resistance and strong corrosion resistance. However due to the decreased modulus of elasticity in titanium compared to steel, titanium will deform approximately twice that of steel (2). This is useful where short bending radii are needed but enhanced deformation is not useful in high tension low torque applications such as UDD (2). Reduced hydraulic efficiencies also contribute to titanium as a poor choice for UDD applications.

An alternative to titanium is aluminum. Aluminum is approximately twice the cost of conventional drill pipe, offering corrosion resistance, and non-magnetic properties. Like titanium

aluminum has a lower modulus of elasticity than steel, therefore requiring greater wall thicknesses which limits fluid dynamics in the well (2).

Due to the required increase in wall thickness and cost for carbon fiber, titanium and aluminum alloys, HSLA steel is the best candidate for UDD wells (2)**.**

1.3 Stresses Encountered in Oil Wells

UDD is a high tension low torque drilling process (3). Due to the enormous weight of miles of pipe all but the last few hundred feet of the pipe are held in tension. Figure 4 shows a free body diagram of the stresses the drillstring and drill pipe experience under operation.
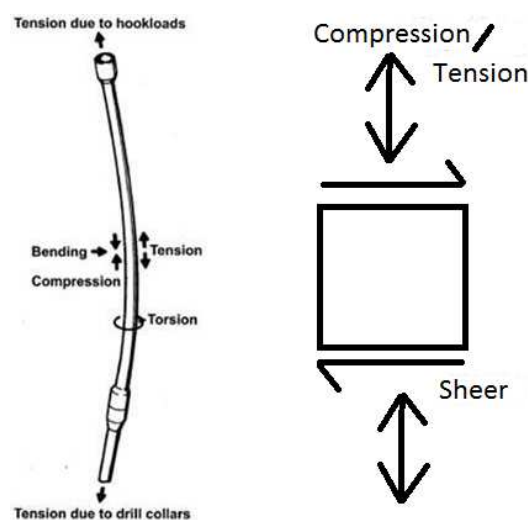
Figure 4 - Free body diagram of drillstring

The fatigue loading conditions for drill strings are typically rotating bend stress of about 1-3 Hz (Figure 4), and vibration loading in the lateral and axial directions of 1-10 Hz, and in the torsional direction from 0.05-0.5 Hz (5). The most common region where failure occurs is at the threaded connections between drill pipe and in the forged upset section of the drill pipe (3) (6).

1.4 Observed Industry Failures

There are two main types of failures in drillstings; washouts and complete twistoff failures. Washout failures, as shown in Figure 5 happen when a pit is formed and subsequent cracking though the thickness of the pipe occurs. Once the crack has penetrated though the thickness of the pipe a rapid erosion attack takes place leaving a void in the thickness of the pipe.
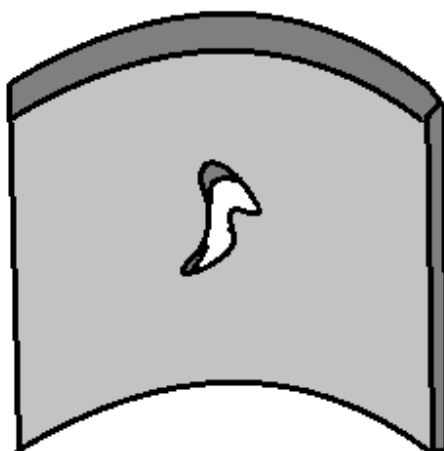
Figure 5 - Diagram of a washout failure

Complete twistoff failures, as shown in Figure 6 initiate similar to washout failures. A pit is formed and cracking ensues; however, the pipe rapidly fractures instead of eroding away. This is likely due to some form of EAC. Complete twistoff failures are very expensive to the oil drilling industry as the pipe below the fracture is not recoverable and often times a parallel well needs to be drilled. It is reported that twist off failures are approximately 10 times as expensive as washout failures (3).
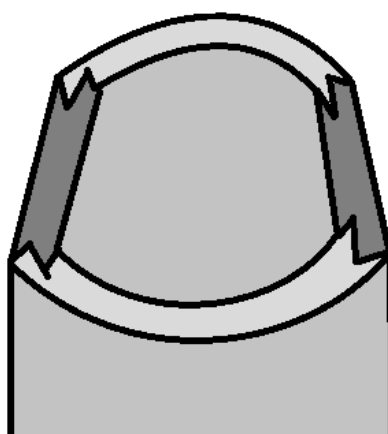
Figure 6 - Diagram of a complete twistoff failure

It is important to note that these failures can be initiated due to pitting corrosion. Pitting corrosion is a known problem in steel. While drillpipes are protected by a coating, the coating

may locally debond from the pipe surface leaving small cavity for the service environment to come in and initiate the pitting process.

1.5 Problem Statement

It has been reported that drillstrings are failing due to fatigue and corrosion fatigue. Inadequate research has been done on the effects pitting corrosion has on fatigue life of drillstrings. While most of the drilling process uses a water based mud with added corrosion inhibitors, a brine solution is used when the well has tapped oil. This brine solution flushes the well of debris and particulates which could be harmful to the pumping systems. This brine solution is highly corrosive. Therefore the goal of this research is to quantify the pitting corrosion degradation of various drilling alloys in a simulated brine completion fluid and to determine pitting corrosion's effect on fatigue performance.

This research investigated the susceptibility of pitting corrosion of various drillstring alloys by immersion testing. Upon the affirmation of pitting corrosion, polarization techniques such as potentiodynamic and cyclic voltammetry were employed to quantify the effects of brine solution on the pitting corrosion resistance of selected drillstring alloys. Potentiostatic and galvanostatic techniques were employed to initiate and attempt to grow pits to various sizes on the drillstring alloys.

Upon the affirmation and quantification of pitting corrosion, investigations of the fatigue lifetimes for various drillsting alloys were tested. Samples were fatigued to failure to construct a fatigue lifetime curve for each drillstring alloy and the effect of pitting corrosion was investigated.

2 Corrosion

Corrosion is the destructive result of a chemical reaction between a metal or alloy and the operating environment (7). Corrosion of metals occurs in an ionically conductive environment such as water. Corrosion happens because there is a lowering of Gibbs free energy for the chemical species participating. For the corrosion process the change in Gibbs free energy is less than zero. For the iron-water system these participating species are the iron metal ions and dissolved oxygen as shown in Figure 7. The study of this energy change is called Thermodynamics and will be presented in section 2.1 Corrosion Thermodynamics.
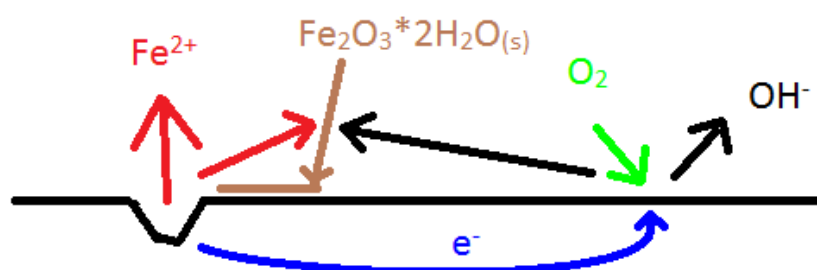
Figure 7 - Oxygen concentration cell

Corrosion acts to dissolve a metal into its ions, effectively lowing the Gibbs free energy of the system (7). In general the chemical reaction will look like Equation 1. Equation 1 will change depending temperature, pH and oxygen concentration.

$$2Fe_{(s)} + O_2 + 2H_2O_{(l)} \rightarrow 2Fe^{2+}_{(aq)} + 4OH^-_{(aq)}$$
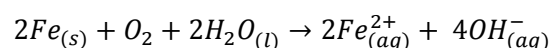
Equation 1 - Corrosion reaction for Iron in pH 7 water with dissolved oxygen

Equation 1 can be separated into the oxidation reaction (Equation 2) which occurs on the anode and the reduction reaction (Equation 3), which occurs at the cathode.

$$2Fe_{(s)} \rightarrow 2Fe^{2+}_{(aq)} + 4e^-$$
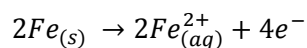
Equation 2 - Anodic oxidation reaction

$$O_2 + 2H_2O_{(l)} + 4e^- \rightarrow 4OH^-_{(aq)}$$
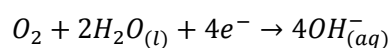
Equation 3 - Cathodic reduction reaction

Corrosion can occur in many forms such as, general, galvanic, crevice, environmentally induced cracking, hydrogen damage, intergranular, dealloying, erosion and pitting (7).

2.1 Corrosion Thermodynamics

To determine if a system has enough energy to corrode, one would analyze the change of Gibbs free energy of the system. If the change in Gibbs free energy is negative, then the system will spontaneously corrode. If the change in Gibbs free energy is positive, then an energy input will be needed for corrosion to occur (7). Consider the following half cell reaction,

$$aA + mH^+ + ne^- \rightarrow bB + dH_2O$$
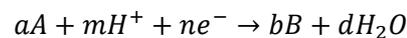
Equation 4 - Half cell reaction

The change in Gibbs free energy is the following:

$$\Delta G - \Delta G^o = RTln\frac{[B]^b[H_2O]^d}{[A]^a[H^+]^m}$$

Equation 5 - Gibbs free energy change

Using Faraday's relations, $\Delta G = -nFe$ (7), Equation 5 transforms into the Nernst equation, Equation 6

$$e = e^o - \frac{RT}{nF}ln\frac{[B]^b[H_2O]^d}{[A]^a[H^+]^m}$$

Equation 6 - Nernst equation - Where: e = potential of the half-cell reaction; e^o = reduction potential of the half cell reaction; R = standard gas constant; T = temperature; n = number of electrons; F = Faraday's constant.

Equation 6 is used to create the Pourbaix diagram which is used to find the thermodynamically stable state of an element in water. Pourbaix diagrams are similar to a phase diagram for metals. Pourbaix diagram shows the stable state given an half-cell potential and pH of solution. Figure 8 - Diagram of the Pourbaix diagram for Iron shows the approximate Pourbaix diagram for iron. See (8) for an accurate Pourbaix diagram.
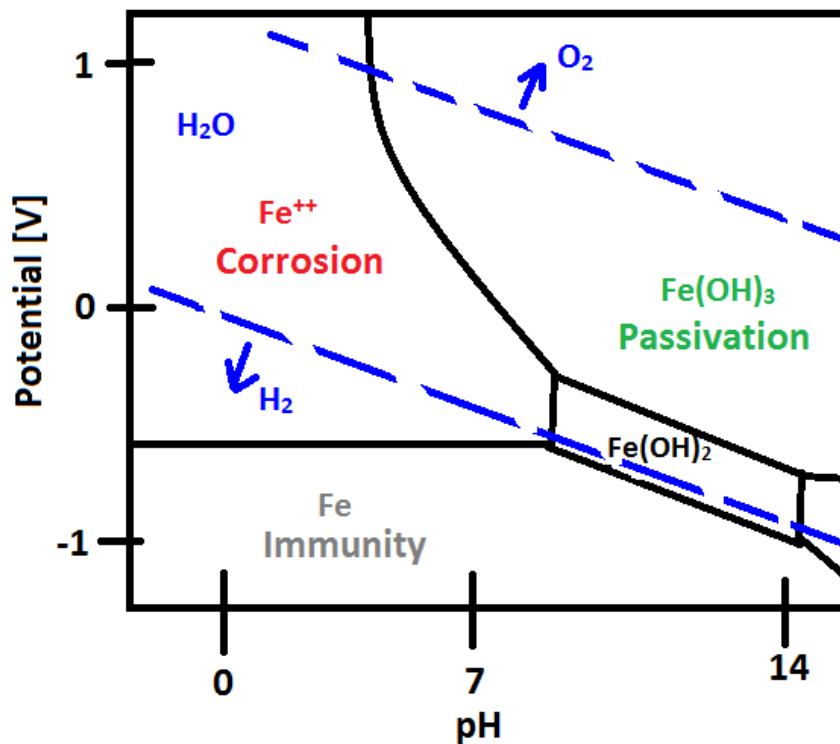
Figure 8 - Diagram of the Pourbaix diagram for Iron

Pourbaix diagrams are useful for predicting the thermodynamically stable component of a system. Pourbaix diagram's tell the user under which conditions iron will be immune to electrochemical corrosion, form a passive oxide film or corrode.

Pourbaix diagrams also show the stability of water. Above the upper dashed blue line in Figure 8 water is no longer stable and separates into H^+ ions and O_2 gas ($2H_2O \rightarrow 4H^+ + O_2 + 4e^-$). Below the lower dashed blue line in Figure 8 water is no longer stable and H_2 gas and OH^- ions are formed ($2H_2O + 2e^- \rightarrow H_2 + 2OH^-$). In-between the dashed blue lines water is stable.

The Pourbaix diagram however shows nothing about the kinetics of the reactions and only shows standard conditions (temperature 298K, pressure 1 bar, ion concentration 10^{-6}M). A further limitation to the use of Pourbaix diagram are that they may predict the wrong species under non-standard or non-equilibrium conditions.

2.2 Corrosion Kinetics

Because corrosion reactions of an electrochemical nature produce and consume electrons, the rate limiting step in the corrosion reaction is the flow electrons. Corrosion rates are measured using Faraday's Law (Equation 7) (7).

$$m = \frac{Ita}{nF}$$

Equation 7 - Mass loss due to corrosion -Where: m = mass reacted, I = corrosion current, F = Faraday's constant , n = number of equivalents exchanged , a = atomic weight , t = time

Polarization, η, is the potential change from the equilibrium half-cell potential caused by the surface reaction rate for the half-cell reaction. Activation polarization also referred to overpotential can be described by the following reactions, Equation 8 and Equation 8Equation 9 for anodic and cathodic polarization respectively (7).

$$\eta_a = \beta_a \log \frac{i_a}{i_o}$$

Equation 8 - Anodic overpotential. Where η_a = Anodic overpotential; β_a = Anodic Tafel constant; i_a = anodic current; i_o = corrosion current

$$\eta_c = \beta_c \log \frac{i_c}{i_o}$$

Equation 9 - Cathodic overpotential. Where η_c = Cathodic overpotential; β_c = Cathodic Tafel constant; i_c = Cathodic current; i_o = corrosion current

β_a and β_c are the Tafel constants for the half cell reaction as depicted in Figure 9. The overall reaction current and overall reaction potential can be found at the intersection of the anodic and cathodic Tafel slopes for each half-cell reaction (7).
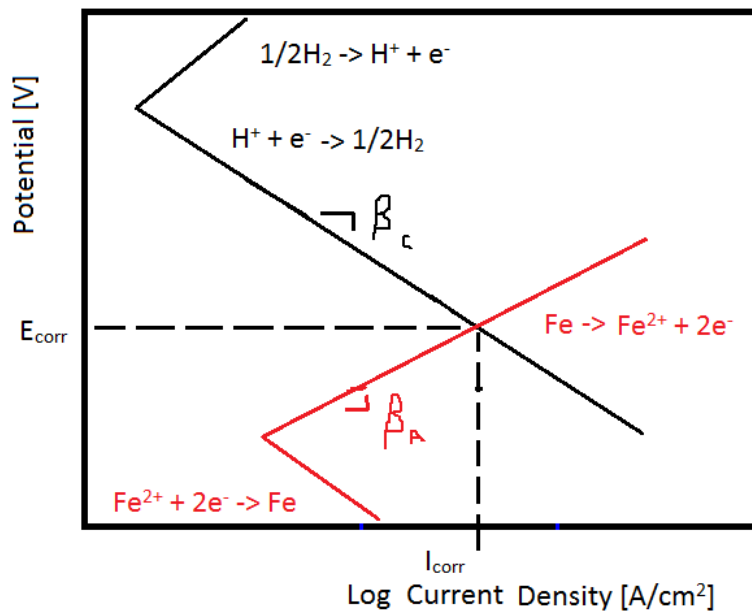
Figure 9 - Example Evans diagram.

At high corrosion rates cathodic reduction can deplete the local reducing species. Depletion of the reducing species has the effect of limiting the reaction rate (7). It is assumed that the anode (oxidizing metal) has near infinite atoms to be oxidized therefore the limiting reaction is the reduction reaction. Dissolved Oxygen has around 8 parts per million at room temperature (7). See Figure 10 for a diagram of the effects of concentration polarization.
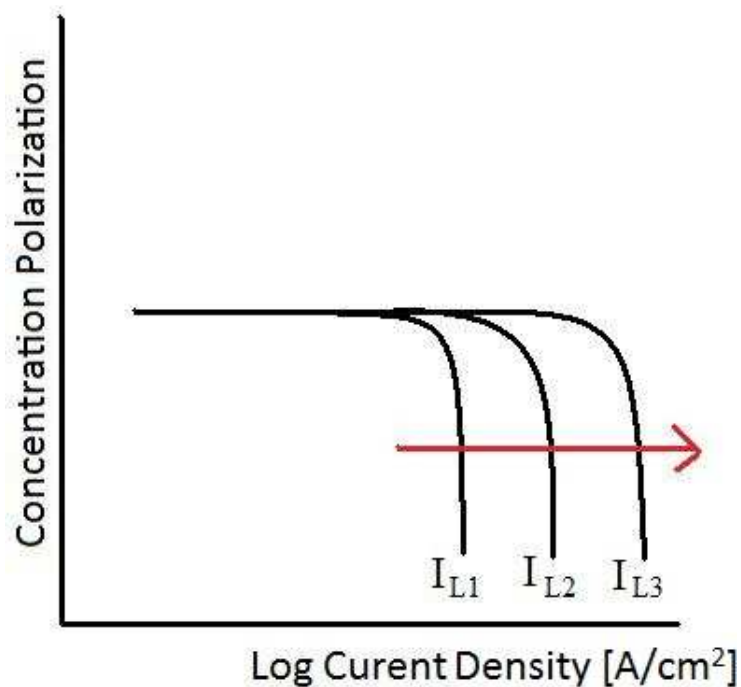
Figure 10 – Diagram of the effect of concentration polarization. Arrow indicates increasing temperature, velocity and concentration of solution.

When temperature, velocity and concentration of solutions are increased the limiting current is increased ($I_{L1}<I_{L2}<I_{L3}$ in Figure 10). The limiting current increases because the diffusion of the reduction species to the cathode increases.

The total polarization is an algebraic sum of the activation polarization and concentration polarization, see Equation 10 (7).

$$\eta_{total} = \beta_c \log\frac{i_c}{i_o} + \frac{2.3RT}{nF}\left[1 - \frac{i_c}{i_L}\right]$$

Equation 10 - Total Polarization. Where: η$_{total}$ = total polarization; β$_c$ = Tafel constant; i$_c$ = cathodic current; i$_o$ = corrosion current; R = standard gas constant; T = tempature; n = number of electrons; F = Faraday's constant; i$_L$ = limiting current

2.3 Erosion Corrosion

Removal of protective surface films by erosion of flowing liquid resulting in accelerated corrosion is called erosion-corrosion. Erosion corrosion is especially detrimental where fluid flow changes directions. Erosion corrosion may take the form of grooves, waves, gullies, and

teardrop shaped pits in the surface. The hydrodynamics of erosion corrosion is not well understood (7).

The proposed mechanism for erosion corrosion involves surface defects which disturb the laminar flow of the system. Eddy currents form around these defects which abrade the protective surface film and allow for corrosion. The protective film will reform and the Eddy currents will further erode the film. Soon a large pit forms in the surface. See Figure 11.
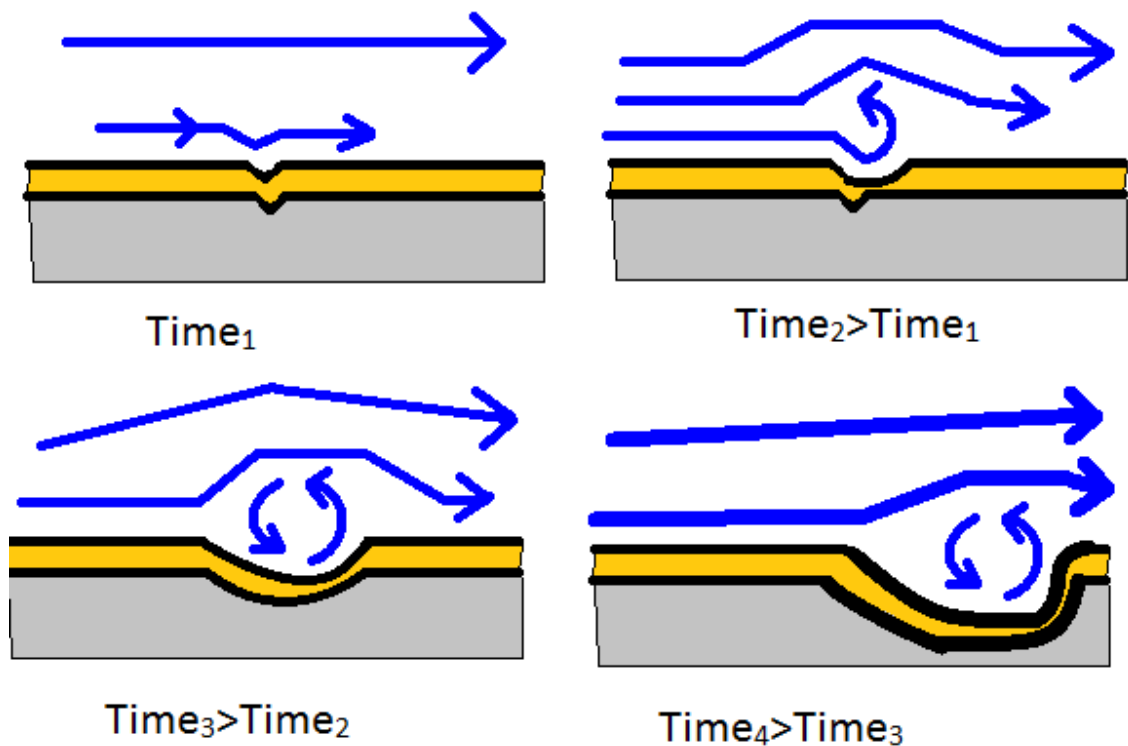
Figure 11- Proposed mechanism for erosion corrosion. Yellow indicates passive film while gray indicates base metal. Blue indicates fluid flow lines.

2.4 Pitting Corrosion

Pits are small micron to millimeter size voids that are formed on the surface due to corrosion phenomena. Pits are caused by the failure of a passive oxide film for passivating materials (7).

Localized corrosion, such as pitting, is an unwanted phenomenon. Pitting can be attributed to many mechanical failures throughout industry (3). A pit is a small defect that forms on the surface of a metal. Pit can take many shapes and sizes. According to ASTM Standard G46-76 (9), pits are categorized by 7 cross sections: Narrow and deep, Elliptical, Shallow and wide, Sub-

Surface, Undercutting, Horizontal and Vertical. See Figure 12 for an example of pit cross sections.
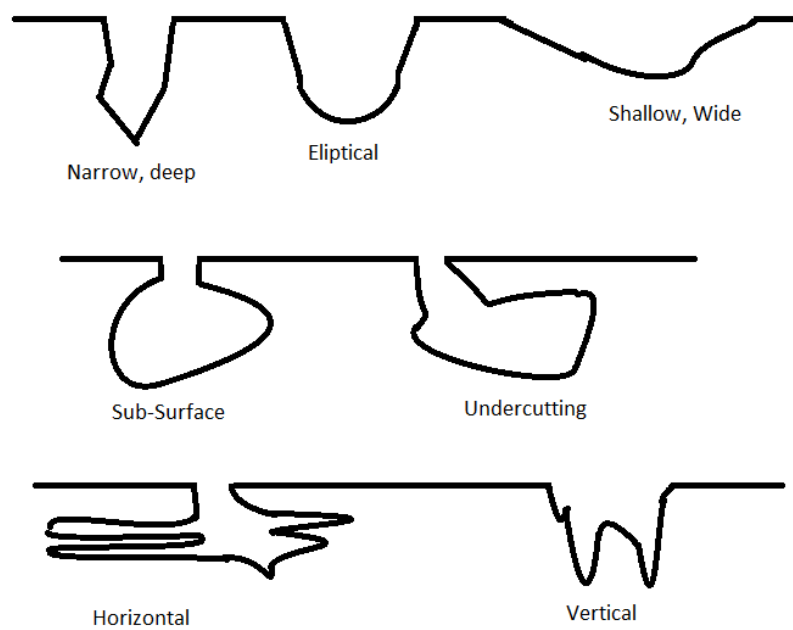
Figure 12 - Diagram showing various pit cross sections

It is well known that pits initiate at sulfide inclusions in carbon steel. How exactly pits form is debated in the literature. Presented in this paper are the mechanisms for pitting corrosion proposed by Wranglen (10) first and Gainer (11) second.

Wranglen found in carbon steels the sulfide inclusions are more noble than the surrounding matrix in chloride ion containing solutions. The sulfur from the nonmetallic inclusion is leached into the surrounding steel matrix. This sulfur contaminated matrix was found to be more anodic than the surrounding matrix, leading to preferential attack of the surrounding sulfur contaminated matrix and formation of a concentration cell as shown in Figure 13 (10) (12). The left column of Figure 13 shows how micro-pits grow into a pit which may continue the growth process in an autocatalytic reaction as depicted in Figure 14. If there are not enough active sulfides to provide a desirable geometry for an autocatalytic reaction then the pit will cease growth.

Wranglen stated that active sulfides depended on size and proximity. Smaller sulfides dissolved more easily into the solution and became activated while larger sulfides were unable to dissolve into the solution and were left dormant (10).
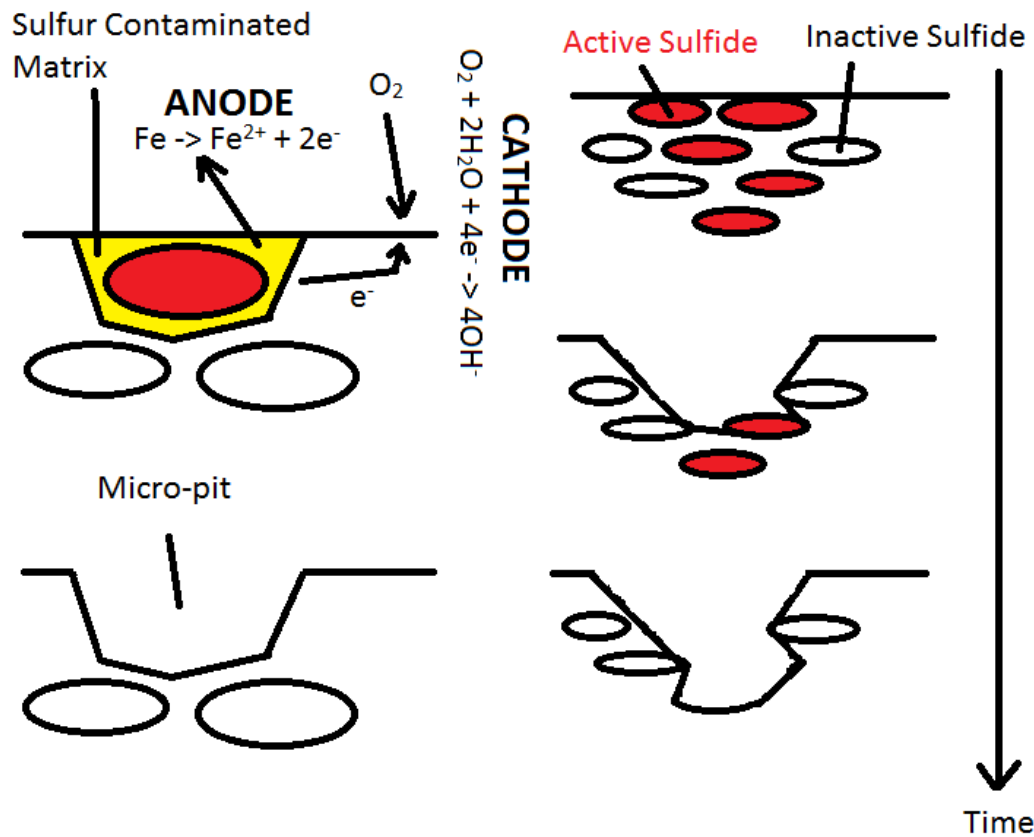
Figure 13 - Showing pit initiation as proposed by Wranglen

As iron is anodically dissolved (in the sulfur contaminated matrix) as in Equation 2, it undergoes hydrolysis and generates H+ ions in the following reaction:

$$Fe^{2+} + H_2O \rightarrow FeOH^+ + H^+$$
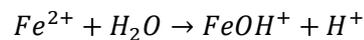
Equation 11 - Hydrolysis of Iron Ions

This acidification chemically dissolves the sulfide inclusion, leaving hydrogen sulfide through the following equation:

$$MnS + 2H^+ \rightarrow H_2S + Mn^{2+}$$
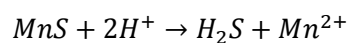
Equation 12 - Acid reaction with MnS inclusion

However, Gainer and Wallwork found that sulfide inclusions were anodic with respect to the matrix in chloride ion solutions. Gainer and Wallwork found micro pits form from actively

dissolving sulfide sites. These micro pits coalesce to form pits in much the same way Wranglen described (10).

Gainer and Wallwork provided no chemistry for their proposed mechanism. Studies (10) have shown that pure MnS is more noble than iron, suggesting that Gainer may have come to an incorrect conclusion. Both Gainer and Wranglen agree that FeS enhances pitting (10) (11) (13). No studies on chemistry of a mixture of FeS and MnS were found. It is possible that a mixture of FeS and MnS will be more detrimental to the steel.

Wranglen found that micro-pits would grow in an autocatalytic reaction under the precipitation of magnetite. The driving force behind this autocatalytic pit growth is the oxygen concentration cell. It is imperative to keep the concentration of oxygen low inside the pit for growth to occur. The autocatalytic conditions are created by 1) preventing passivation inside the pit by oxidation of iron hydrate, 2) formation of a hydrate blister in pit mouth which limits O_2, H^+ and Cl^- ion diffusion, and 3) retarding the general corrosion rate around the pit by cathodically protecting the surrounding surface (10).

Preventing passivation inside the pit was done in part by hydrolysis of the Fe^{2+} ions, Equation 13. Once the iron ions hydrolyzed they would further be oxidized, consuming the local O_2, and hence preventing passivation within the pit, Equation 14. Hydrolysis of Fe^{2+} ions increase the local pH inside the pit, which increases corrosion rates and dissolves any remaining sulfide compounds.

$$Fe^{2+} + H_2O \rightarrow FeOH^+ + H^+$$
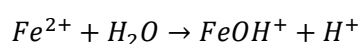
Equation 13 - Hydrolysis of the Iron ions

$$2FeOH^+ + \frac{1}{2}O_2 + 2H^+ \rightarrow 2FeOH^{2+} + H_2O$$
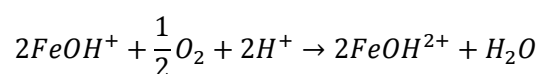
Equation 14 - Oxidation of the Iron hydrate

$$2FeOH^{2+} + Fe^{2+} + 2H_2O \rightarrow Fe_3O_4 + 6H^+$$
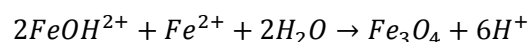
Equation 15 - Precipitation of magnetite

The precipitation of magnetite, Equation 15, "caps" the pit preventing oxygen and Cl^- ions from defusing inwards and limiting diffusion of H^+ out of the pit. This limiting of ions diffusing freely, combined with the acid generation from the precipitation of magnetite, creates the reactants for

further magnetite precipitation and hence the autocatalytic reaction. See Figure 14 for a visual diagram of these reactions.
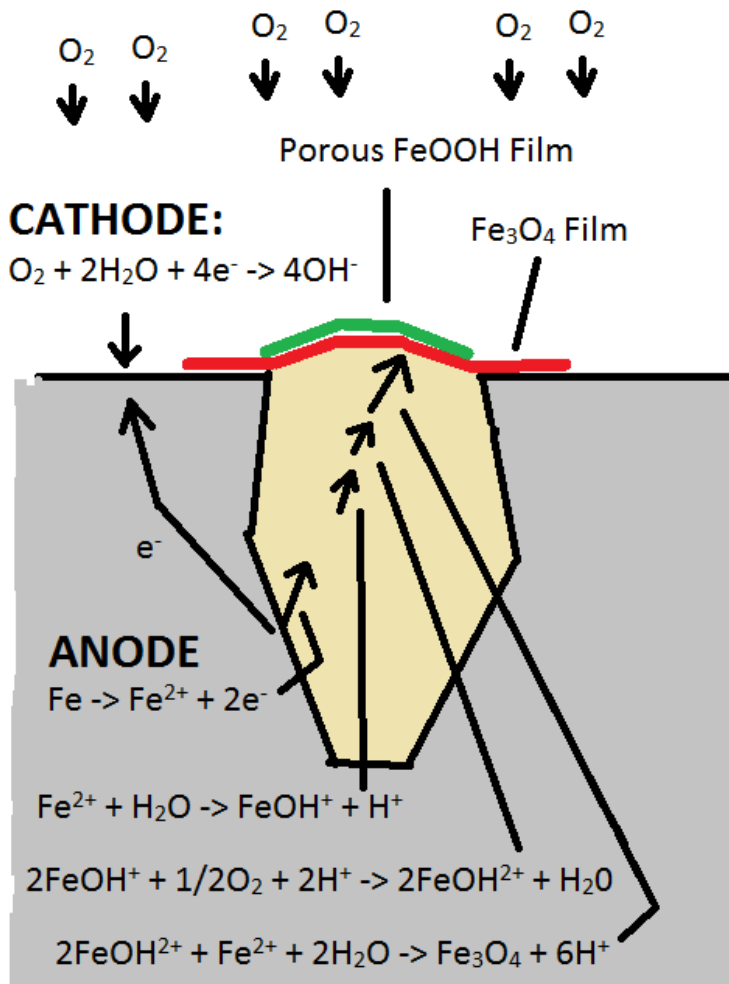
Figure 14 - Diagram of the autocatalytic electrochemical reactions taking place during pit growth proposed by Wranglen's model

In the absence of Fe_3O_4, FeOOH will be formed though the following equations, Equation 16-Equation 17.

$$FeOH^{2+} + H_2O \rightarrow Fe(OH)_2^+ + H^+$$
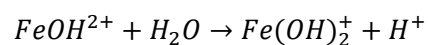
Equation 16 - Iron hydrate formation

$$Fe(OH)_2^+ + OH^- \rightarrow FeOOH + H_2O$$
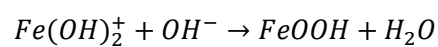
Equation 17 - FeOOH formation

Chlorides are observed to exacerbate the pitting process but the mechanism is debated (14). Multiple authors have established the adsorption of chloride ions on metal surfaces. The adsorption, however, is not uniform but tends to concentrate at surface irregularities (15). It is argued by Heusler that the formation of chloride islands on the surface of metals precedes pit nucleation (16). Seyes showed that local acidification occurs prior to pit formation (17).

However, Flis argues that current pit nucleation theories fail to explain the role of chlorine ions in pit initiation. Flis suggests that the role of chloride ions is to form a chloride salt which prevents repassivation of the pit. This chloride salt is situated at the bottom of the pit (14).

2.5 Corrosion Protection

There are various methods to retard or prevent corrosion. Each method has its own advantages and disadvantages. Various methods to protect against corrosion are presented in the following sections.

2.5.1 Cathodic Protection

To cathodicaly protect a surface, an imposed cathodic current is applied to the former anode. Cathodic protection works by flooding a system with electrons so the anodic reaction will cease or slow down considerably (7). Consider the following half cell reactions,

$$Fe \rightarrow Fe^{2+} + 2e^-$$
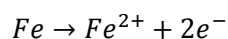
Equation 18 - Anode reaction

$$2H_2O + 2e^- \rightarrow H_2 + 2OH^-$$
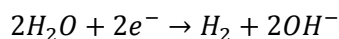
Equation 19 - Cathode reaction

Having an excess of electrons will shift the equilibrium to the left for Equation 18 and to the right for Equation 19.

$1/2H_2 \rightarrow H^+ + e^-$

$H^+ + e^- \rightarrow 1/2H_2$

E_{corr}

E_{app}

$Fe \rightarrow Fe^{2+} + 2e^-$

$Fe^{2+} + 2e^- \rightarrow Fe$

I_a I_{corr} I_c

Log Current Density [A/cm^2]
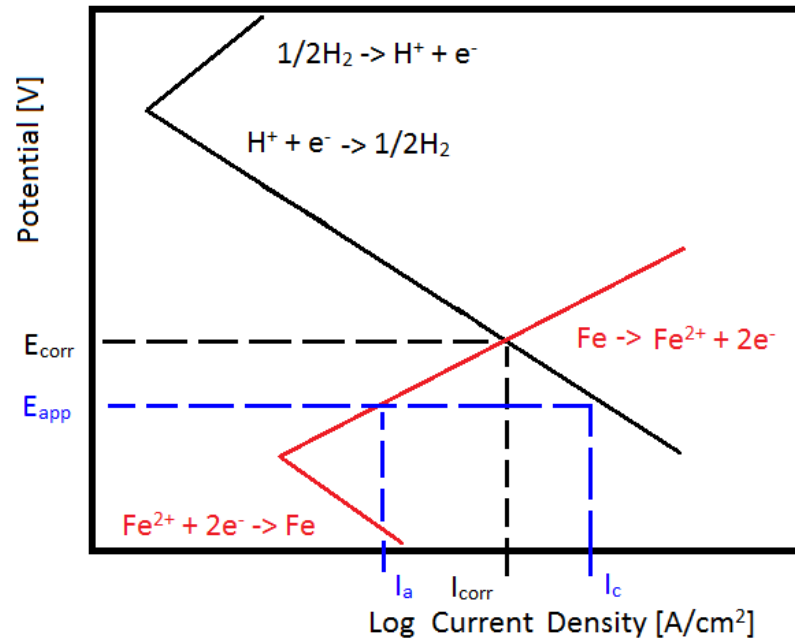
Potential [V]

Figure 15 - Diagram showing corrosion rates in iron-water system

Applying a cathodic protection potential can reduce the corrosion current experienced by the anode by orders of magnitude from, I_{corr} to I_a (see in Figure 15). However the cathodic current is also increased by orders of magnitude from I_{corr} to I_c (7).

The disadvantage to this method of protection is under oxygen void solutions, hydrogen is generated that could possibly embrittle the metal intended to protect.

2.5.2 Sacrificial Anode:

The sacrificial metal is more active (more negative reduction potential) than the coupled metal, therefore, the sacrificial metal will corrode before the protected metal (7).
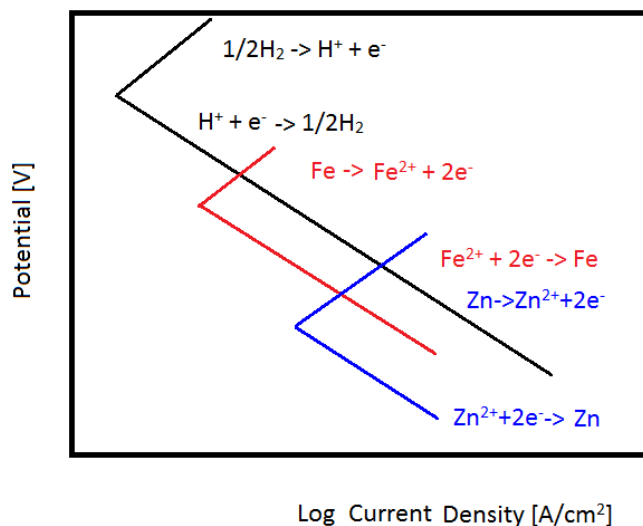
Figure 16 - Diagram showing effect of coupling a metal to another. In this figure Iron is protected by a sacrificial anode of Zinc

If one had a cell where iron is coupled with iron then the anode and cathode reactions, represented by the red and black lines in Figure 16 would be:

Anode: $Fe \rightarrow Fe^{2+} + 2e^-$

Cathode: $2H^+ + 2e^- \rightarrow H_2$
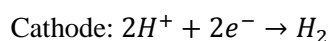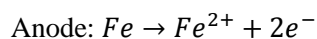
However when a more noble metal like zinc is coupled with iron, iron is now the cathode and switches from dissolution to deposition, represented by the red and blue lines in Figure 16

Anode: $Zn \rightarrow Zn^{2+} + 2e^-$

Cathode: $Fe^{2+} + 2e^- \rightarrow Fe$
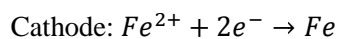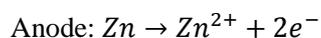
The main disadvantage to sacrificial anode protection method is that the sacrificial anode must be periodically replaced. Sacrificial anodes do not work in oil wells because the well pipe would have to be periodically removed and the depleted sacrificial anode replaced.

2.5.3 Corrosion Inhibitors

Corrosion inhibitors are substances which lower the corrosion rate by retarding the anodic and cathodic processes (18). Anodic inhibitors retard the anodic dissolution rate while cathodic inhibitors retard the cathodic rate. Mixed inhibitors retard both anodic and cathodic processes. The risk of using a anodic inhibitor is that a large cathodic area and small anodic area may arise if there is not enough anodic inhibitor. This relatively small anodic area may lead to pitting corrosion. See Figure 17 - The effect of corrosion inhibitors for a diagram of how inhibitors effect corrosion rates.
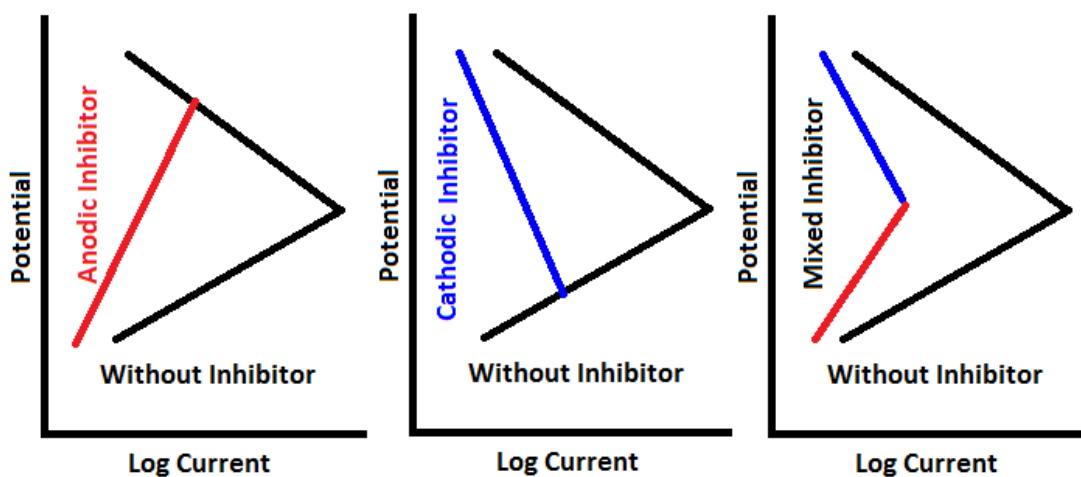
Figure 17 - The effect of corrosion inhibitors

Typical corrosion inhibitors include chromate, nitrite, molybdate, tungstate, and silicate benzoate for anodic inhibitors. Cathodic inhibitors include polyphosphate, aminoethylene phosphonate and zinc sulfate. Mixed inhibitors include organics containing amines, triazols thiazols and alkylthioureas. Inorganic mixed inihbitors include arsenite, arsenate and selenate.

2.6 Corrosion Investigation Methods

Combining the knowledge from sections 2.1 Corrosion Thermodynamics and 2.2 Corrosion Kinetics one can attempt to measure, control and predict corrosion.

2.6.1 Immersion Testing

Immersion testing is immersing a sample in an environment and periodically checking on the corrosion progress of the material. Immersion testing will reveal what form of corrosion is

observed and can reveal the corrosion rate of the material if weight of the sample is measured before and after immersion. See Figure 18 for a schematic of an immersion test.
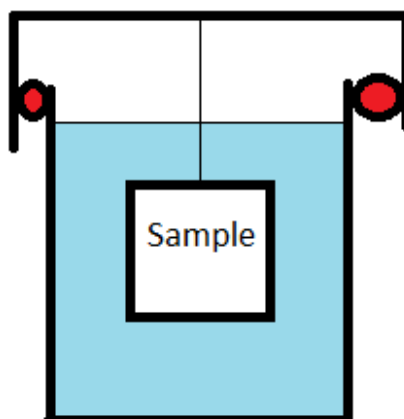
Figure 18 - Diagram of immersion test

2.6.2 Dynamic Corrosion Control Methods

Polarization curves are a useful method to determine important corrosion information such as mechanisms, dissolution corrosion rates and susceptibility of materials to specific corrosion types.

Polarization curves are generated using an electrochemical cell and a potentiostat. The potentiostat has the ability to hold the electrode at a specific voltage and measure current, or hold the electrode at a specific current and measure the voltage. The potentiostat also has the ability to measure the voltage difference between two electrodes when no current is applied. This is referred to as Open Circuit Potential (OCP). The potentiostat is programmed with cell area, which it used to calculate current density. Scan rates vary from 0.6 volts per hour to 60 volts per hour (19).
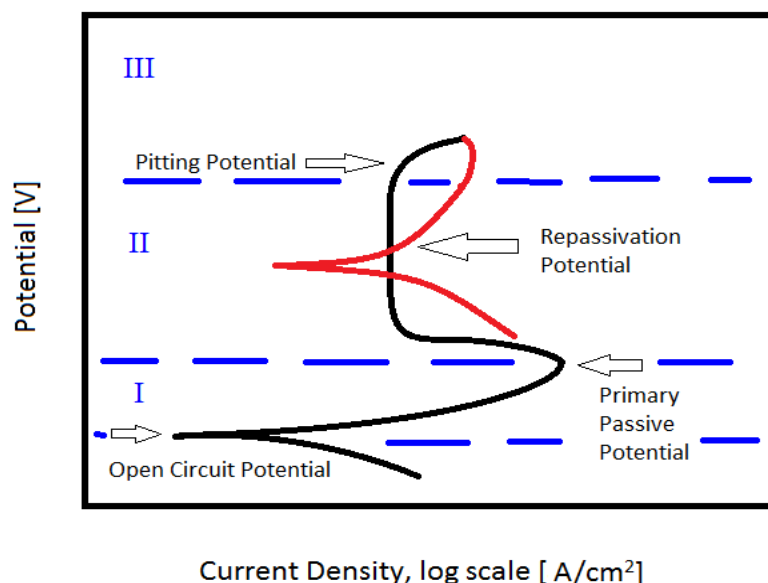
Figure 19 - Example cyclic voltammogram for an active-passive alloy. Forward scan in black, reverse scan in red

With regards to Figure 19, the scan is initiated below the OCP in the cathodic region. As the potential is increased, a correlating decrease in anodic current density is observed. In region I active dissolution is occurring. As we increase the potential further into region II, a decrease in current density followed by no change in current density is observed. Chemical passivation is taking place in region II. If we further increase the potential, a transpassive region is observed in region III. Pitting corrosion may be observed in this transpassive region III. If hysteresis is found between the forward scan (black) and reverse scan (red) in Figure 19 then the alloy is susceptible to pitting corrosion.

As of 1991 the most current scientific explanation of the pitting potential is expressed by Videm (5) which states that the pitting potential is the potential above which the repassivation rate is lower than the dissolution rate. The onset of pitting corrosion is observed to happen at the pitting potential. Above the pitting potential, the system has enough energy to nucleate new pits. The pitting potential is an empirically found value dependent on material and solution.

The repassivation potential is the potential below which the protective passive film is stable. The repassivation potential is an empirically found value dependent on material and solution.

Materials may passivate due to a electrochemical reaction with oxygen forming a stable protective film such as is the case for Al. Aluminum reacts with oxygen to form a protective Al_2O_3 surface film. Other materials may mechanically passivate.

Mechanical passivation is a process where the corrosion product reaches its saturation limit in solution and precipitates on the surface of the material. An example of mechanical passivation is iron (II) Oxide. Iron will dissolve until the saturation limit of Fe_2O_3 has been reached. Upon saturation, Fe_2O_3 will precipitate on the surface of the material.

2.6.3 Static Corrosion Control Methods

Static methods can be useful to control pitting corrosion, and investigate solution and sample surface consistencies.

Above the pitting potential the system has enough energy to pit. Therefore, to pit samples a cell is held at a pitting voltage to nucleate pits. To grow pits the cell is then held between the pitting and repassivation potentials as found on the potentiodynamic polarization curve, Figure 19. Below the repassivation potential a protective passive film is stable, and above the repassivation potential the protective film will not form. This allows for further corrosion; however, there is not enough energy for pit nucleation.

Monitoring the open circuit potential (OCP) can reveal the constancy of a sample's surface conditions in the cell. If open circuit potentials are different between samples then the sample surface conditions may vary from experiment to experiment. Having a different electrochemical surface from sample to sample will interfere in the reproducibility of experiments. Small amounts of corrosion damage may be responsible for inconsistencies in OCP as well as changes in solution preparation and daily temperature variations.

3 Fatigue

Fatigue is the progressive and localized structural damage that occurs when a material is subjected to cyclic loading. Repeated cyclic loading leads to different amounts of slip on different glide plains in polycrystalline materials. Some of this slip is irreversible for various reasons, and leads to microscopic roughening of the surface. The roughening emerges as microscopic "valleys" where slip bands emerge on the surface. The surface roughening acts to add micro-notches on the surface effectively raising the local stress concentration (20).
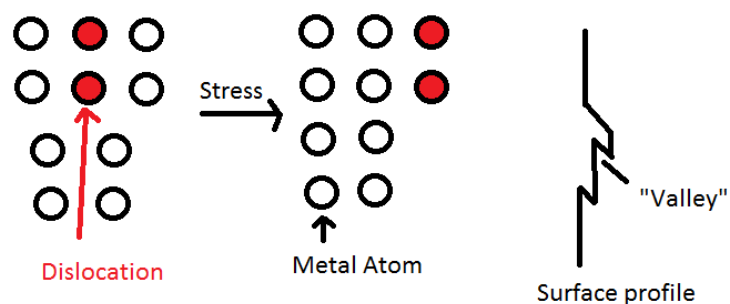
Figure 20 - Diagram of a dislocation and dislocation movement

As seen in Figure 20 dislocations are responsible for deformations on the atomic scale. If enough dislocations deform a material in a specific area a microscopic valley may form, inducing a stress concentration. This stress concentration acts as a site for crack nucleation. The stress concentration also amplifies the local stress field which, if increased past the threshold stress intensity for crack growth, causes a crack to grow, leading to material failure. The process of dislocation slip forming a micro-valley, as shown in Figure 20 applies to an ideal laboratory situation for Face Centered Cubic (FCC) metals only.

For multigrain Body Centered Cubic (BCC) steels, crack initiation is observed at non-metallic inclusions. BCC materials such as iron, have higher Peierls-Nabarro stresses than FCC metals hence dislocation movement is harder in BCC materials (21). Dislocations tend to pile up around nonmetallic inclusions and initiate a crack around or through an inclusion as shown in Figure 21.
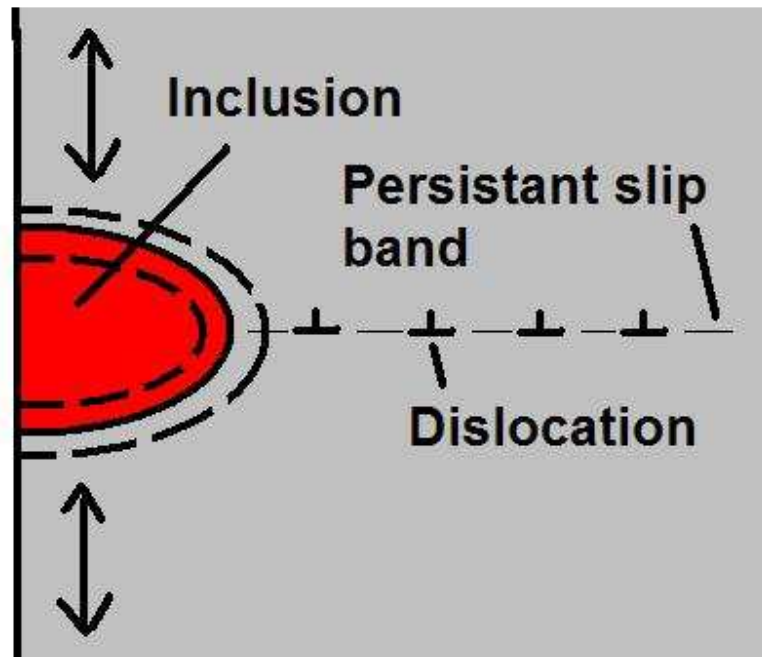
Figure 21 - Diagram showing crack initiation in BBC steels.

The non-metallic inclusion tends to have higher modulus of elasticity and higher coefficients of thermal expansion (22) (23) (24) (25). The difference in modulus of elasticity causes different expansion rates under stress, which acts to amplify the stress felt in the matrix. When dislocations are introduced around this nonmetallic inclusion the stress felt by the inclusion is greatly increased. This amplification of stress can lead to a local debonding of the inclusion from the matrix, leaving a surface for crack nucleation to occur. The inclusion itself can also crack.

3.1 Fatigue Lifetime Approach

To quantify how materials fatigue over their lifetimes a stress-cycle, or S-N curve, is empirically found. S-N curves plot the cycles to failure against the stress amplitude. The "S" in S-N curve stands for stress amplitude, while the "N" stands for the number of cycles to cause failure. Stress amplitudes can be fully reversed (σ_{min} = -500 MPa, σ_{max} = 500 MPa, R=-1), tension only (σ_{min} = 0 MPa, σ_{max} = 500 MPa, R=0) or any other loading cycle desired. The "R" value, or loading ratio is found by dividing the minimum stress by the maximum stress.

Ferrous alloys often show an endurance limit in ambient air. The alloy is not observed to fail for stresses under the endurance limit. Aluminum and some high strength steels do not exhibit an endurance limit. For alloys where no apparent endurance limit is observed a stress correlating to

10^7 cycles is the commonly accepted fatigue strength of the material (20). The accepted fatigue strength of the material can change depending on the cycled frequency. For low frequencies it is common to set the fatigue strength to 10^6 cycles, while at higher frequencies 10^8 or 10^9 cycles may be the set fatigue strength. See Figure 22 for an example of the S-N curve.
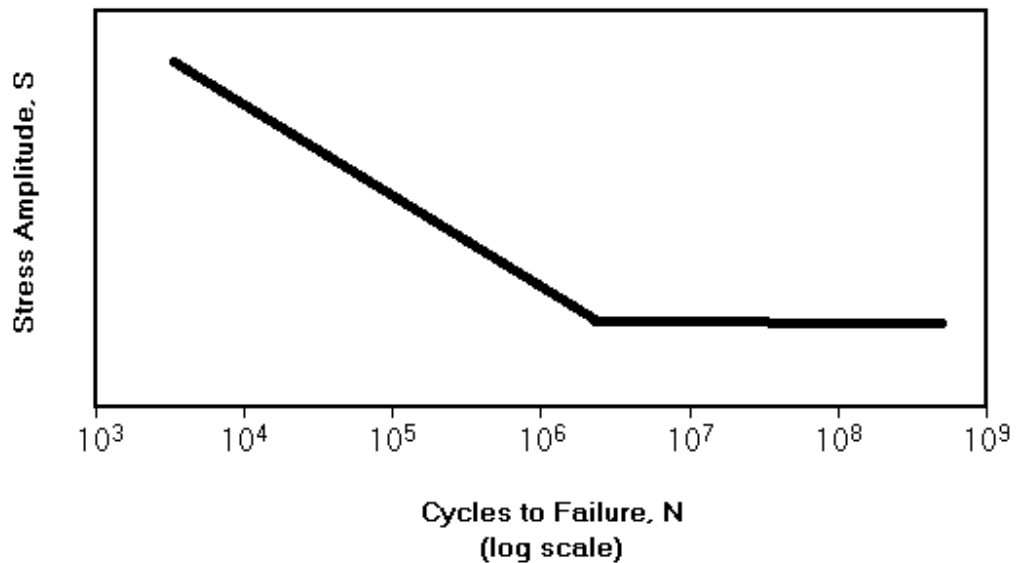
Figure 22 - Diagram of the stress - cycles (S-N) curves for ferrous alloys

3.1.1 Fatigue Statistics

To construct a S-N curve many samples must be used due to the sample to sample variability. It is not uncommon to have wide variation in failure cycles. Sources of variation include inconstancies in the surface finish and the digital controller fatiguing the specimens. The spread in fatigue life follows a normal distribution for each stress level measured. The normal distribution is commonly referred to as a "bell curve." The normal distribution graphically represents the variability of data. The features of a normal distribution are that 68% of the gathered data will fall within one standard deviation from the mean value. See Figure 23 for a diagram of the normal distribution.
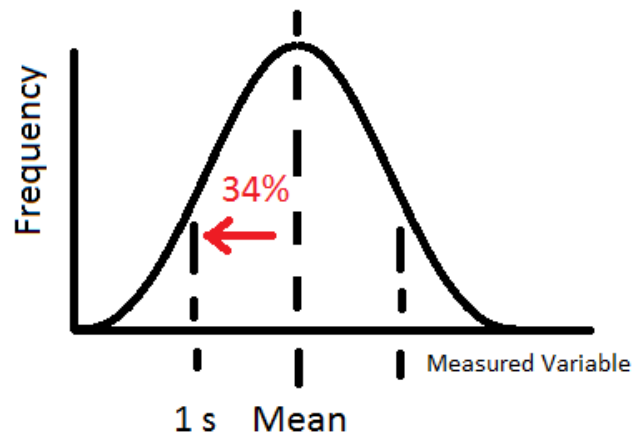
Figure 23 - Diagram of the normal distribution

S-N data is typically reported by mean failure at a tested stress level with error bars of +- one standard deviation. The mean is the sum of all cycles to failure for a particular stress level divided by the number of samples measured. Standard deviation is the measurement of variability of the cycles to failure for a particular stress level. Standard deviation "s" is measured by the following Equation 20.

$$s = \sqrt{\frac{1}{N}\sum_{i=1}^{N}(x_i - X)^2}$$

Equation 20 - Standard deviation - Where: s = standard deviation; N = number of samples; x_i = cycles to failure for specific sample; X = mean cycles to failure

3.1.2 Fatigue Statistics Mean Comparison

To see if a treatment affected the S-N curve a statistical analysis called the "Student's T Test" is used (26). Student's T test compares the means and variations of the mean for two testing conditions. The Student's T test allows one to say with a confidence interval that the means are statistically different. In general two different means with small standard deviations are likely statistically significantly different, where two different means with large distributions are not likely statistically significant. See Figure 24 for an schematic of testing conditions which are statistically significant and non-statistically significant.
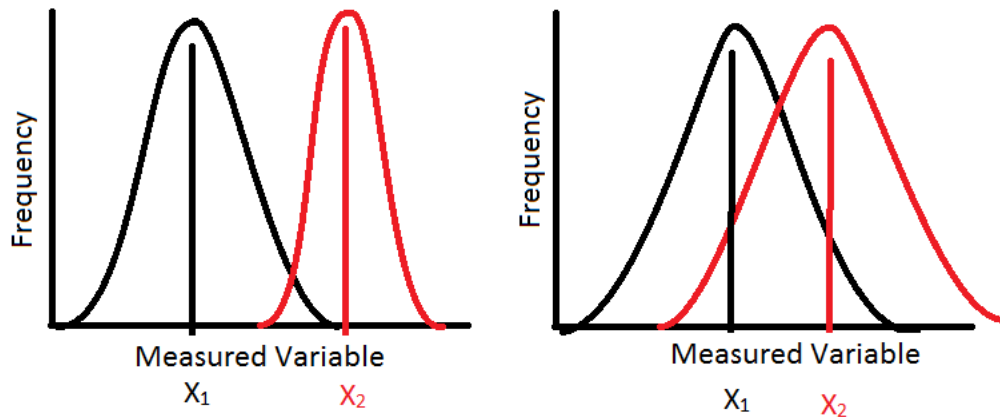
Figure 24 - Diagram showing two normally distributed samples. Left - samples have statistically different means. Right - samples have statistically insignificant means

To calculate the T value the following formula is used, Equation 21

$$t = \frac{X_1 - X_2}{\sqrt{\left(\frac{\sum X_1{}^2 - \frac{(\sum X_1)^2}{N_1} + \sum X_2{}^2 - \frac{(\sum X_2)^2}{N_2}}{N_1 + N_2 - 2}\right)\left(\frac{1}{N_1} + \frac{1}{N_2}\right)}}$$

Equation 21 - Formula for T value - Where: X$_1$ = mean of population 1; X$_2$ = mean of population 2; N$_1$ = size of population 1; N$_2$ = size of population 2

After calculating the T value one can compare the T value with the degrees of freedom ($N_1 + N_2 - 2$) to a table listing the T distribution found in any statistical textbook to see if the result is 99.9, 99, 98 or 95 percent confident the means are different (26). If the confidence interval is less than 95% then the means are considered statically insignificant.

3.2 Linear Elastic Fracture Mechanics

Linear Elastic Fracture Mechanics (LEFM) was developed to help explain why glass fibers were breaking at orders of magnitude less than what they theoretically should have. It was postulated that microscopic defects were responsible for this discrepancy. LEFM does not describe how cracks initiate but describes how cracks grow and provides estimates on the expected lifetimes of materials containing defects.

There are two main theories of LEFM. The energy criterion approach and the stress intensity approach (27). The energy criterion states that fracture occurs when the energy available for crack growth exceeds the energy to create a new surface and the energy lost to plastic deformation (27).

The stress intensity approach states that fracture occurs when the stress-intensity factor is equal to an empirically found stress-intensity material constant. The stress intensity method measures a fracture constant, K_{Ic} , and defines this as the material toughness. Generally, a form of Equation 22 is then used to calculate the K_I value. The K_I is then compared to an empirically found material constant K_{Ic}. If K_{Ic} is met or exceeded fracture will occur (27).

$$K_I = Y\sigma\sqrt{\pi a}$$

Equation 22 - Formula for stress intensity - Where: K_I = mode 1 stress intensity; Y = dimensionless constant dependent on loading mode and geometry; σ = applied stress; a = applied crack length

LEFM only applies to cases where there is limited plastic behavior experienced by the material. LEFM can be used to approximate real behavior in metals assuming the yield stress is not met or exceeded, except for a small region near the crack tip.

The stress intensity factor is unique to a geometry. Mode I (K_I) is representative of tension, while Mode II (K_{II}) is representative of in plane shear. Mode III (K_{III}) is representative of out of plane sheer. See Figure 25 for a diagram of the different modes of cracking (27).
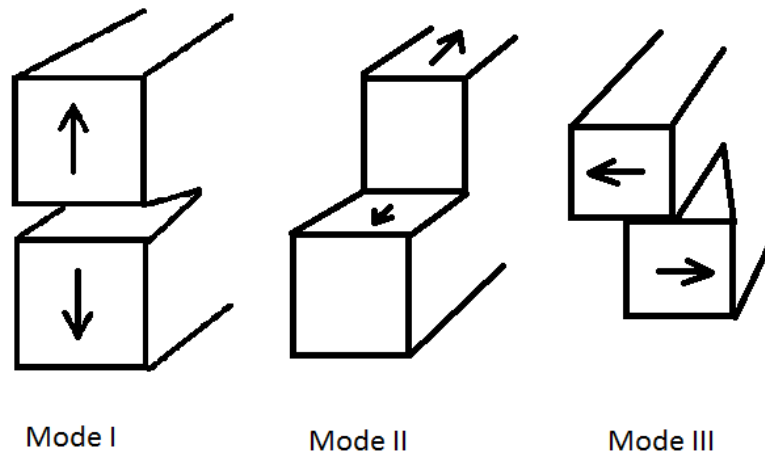
Figure 25 - Diagram showing the different modes of cracking

The stress ahead of the crack tip in the growth direction for mode I is:

$$\sigma = \frac{K_I}{\sqrt{2\pi r}}$$

Equation 23 - Stress ahead of crack tip - Where: r = Distance from the crack tip

The major flaw with the stress intensity approach is that infinite stresses are predicted at the crack tip (27). However, plastic deformation causes the stresses to remain finite.

3.2.1 LEFM - Crack Growth

Drill pipes are designed to undergo cyclic stresses which can introduce cracks. Cracks will grow if the stress intensity is below the fracture stress intensity (K_c) and above the threshold fatigue crack growth stress intensity (K_{th}).

Crack growth rates are plotted with the stress intensity against the growth per cycle as seen in Figure 26. Both variables are on a log scale. When crack growth is plotted this way three phases of crack growth are observed. In the first region of Figure 26 crack growth is not observed until a threshold stress intensity (ΔK_{th}) is reached. In the second region of Figure 26 crack growth by a power law is observed. The second region of crack growth is often referred to as the Paris region as Paris and Erdogan (28) were the first to discover the power law relationship, Equation 24**,** in

the second region of Figure 26. In the third region on Figure 26 crack growth is seen to accelerate until final fracture.
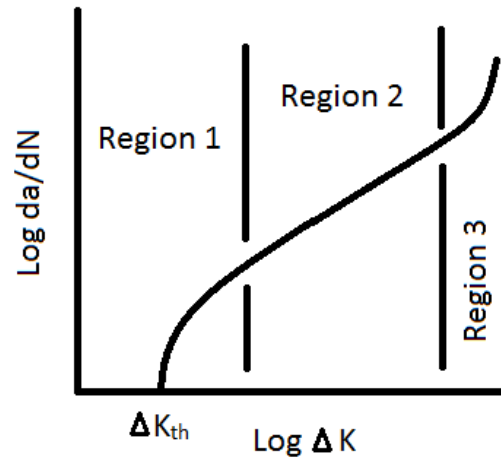
Figure 26 - Diagram of the three phases of crack growth

$$\frac{da}{dN} = C\Delta K^m$$

Equation 24 - Where: da/dN = crack growth rate per cycle; C = material constant; m = material constant; ΔK = stress intensity range

4 Environmentally Assisted Cracking

EAC is a persistent problem in the oil industry. EAC is a general term relating to corrosion fatigue problems. EAC may refer to any of the following types of cracking due to the environment (27):

- Stress Corrosion Cracking (SCC)

- Hydrogen Embrittlement (HE)

- Corrosion Fatigue (CF)

SCC is a problem for materials that passivate, like Al and Stainless Steels (27). During SCC stress causes the passive film to rupture, leading to anodic dissolution and reformation of the passive film. Stress causes further rupture of this film and further corrosion. Crack propagation is accelerated due to anodic dissolution at the crack tip.

The mechanism for HE is under debate; however the most commonly accepted model for HE is that atomic hydrogen lowers the metallic bond strength between metal atoms (27). HE has the effect of lowering a materials fracture toughness and subcritical crack growth is observed.

CF is defined as the acceleration of crack growth due to the interaction with the environment. CF is defined in the following Sections 4.1 and 4.2

4.1 Corrosion Fatigue - Crack Initiation

As reported in section 3.1 Fatigue Lifetime Approach, cracks are experimentally observed to nucleate at nonmetallic inclusions intersecting a Persistent Slip Band (PSB). As reported in section 2.4 Pitting Corrosion non-metallic inclusions are seen to anodically dissolve in chlorine ion containing solutions leaving a pit. When this fatiguing process and corrosion process occur simultaneously it is called corrosion fatigue. This combination is synergistic and leads to material failure before the effects of pitting damage or fatigue alone.

For steel fatigued in chlorine ion containing solution, Wang found that corrosion assisted plasticity by electrochemically removing the barriers inhibiting dislocation movement (25). Cracks were observed to initiate at inclusions which intersected with a PSB. The PSBs provide a continuous source of fresh iron to anodically dissolve. This dissolution removes the barriers to further slip, enhancing the localization of both deformation and further dissolution, leading to a crack initiation.

Murtaza (23) described corrosion fatigue as a three step process. Step 1) Pit development, Step 2) Environmentally assisted short crack growth controlled by strain assisted dissolution, and Step 3)

Environmentally assisted long crack growth. Murtaza studied martensitic spring steel fatigued at 5hz and R=-1 and found that cracks initiated in mode II sheer in both air and in a 0.6 M NaCl environment at room temperature. The transition from mode II (short crack growth) to mode I (long crack growth) happened when the crack reached 4x the prior austenite grain size (PAGS) for air fatigue and 1x the PAGS for corrosion fatigue.

The specific mechanisms for crack initiation assisted by the environment are likely to be highly dependent on the corrosive solutions, material and geometry.

4.2 Corrosion Fatigue - Effects on Crack Growth

The effect of the environment on crack growth rates is largely determined by the ability of the corrosive species to diffuse to the crack tip. The corrosive environment may accelerate crack growth and decrease the threshold stress intensity (Figure 27). In other cases a time dependent effect is observed, where the effects of the corrosion species are not observed until an amount of time has passed (27). See Figure 27.
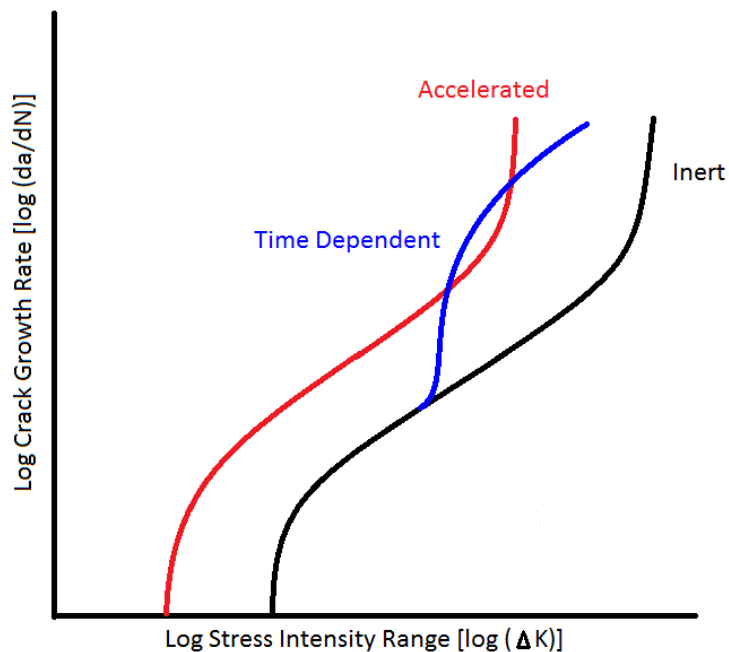
Figure 27 - Diagram of the various effects a corrosive environment has on crack growth rates

For accelerated corrosion fatigue, there is a synergistic effect of mechanical fatigue and the environment. This effect causes crack growth below the threshold stress intensity (K_{th}) to cause

Stress Corrosion Cracking (SCC) under static loads in the corrosive environment and fatigue crack growth under cyclic loads in an inert environment (29). Accelerated behavior can happen in environments that do not result in significant SCC under static loads. Also, transport of the corrosive species and electrochemical reaction rates must be very rapid (27).

For time dependent corrosion fatigue, crack growth rates are observed to correlate to the inert case and then after some time has passed accelerated crack growth occurs with respect to the inert case. A possible explanation for this lag in accelerated crack growth is that diffusion and reaction rates of the corrosion species are slow and time is needed for the corrosion species to diffuse to the crack tip and react electrochemically. Time dependent corrosion is frequency dependent and at higher frequencies the time dependency phenomena disappears as faster loading frequencies do not allow time for corrosion products to diffuse and chemically react with the metal. (27). Most materials exhibit both accelerated and time dependent corrosion fatigue.

4.3 Pit to Crack Modeling

One method to model the pit to crack transition is to model a pit as a mechanical notch. LEFM is then used to calculate a critical pit depth where crack growth is observed.

LEFM can be a useful tool to describe when a crack will grow and the dynamics of the crack growth. Attempts have been made to use LEFM to model crack growth from a pit, substituting the pit depth for an initial "crack" size and defining a threshold stress intensity range (ΔK_{th}) where the pit transitions into a crack, i.e., crack growth is observed.

Lu (22) and Akid (24) question the ability to use a threshold stress intensity (ΔK_{th}) to model pit to crack transition as much plasticity is involved. Lu and Akid argue because there is plasticity involved in the pit to crack transition, LEFM is invalid as LEFM assumes limited plasticity.

Akid attempted to model a threshold stress intensity taking into account plasticity and electrochemical behavior using Equation 25 (24). Akid based his equation on experiments using 316L stainless steel in 0.05% $FeCl_3$ solution.

$$a = \left[\frac{3MI_{PO}}{2\pi nF\rho} exp\left(-\frac{\Delta H}{RT}\right) t_{pit} + a_0^3 \right]^{1/3} \ where \ a \leq a_{tr}$$

Equation 25- Modified crack length - where - M = Atomic weight of Fe; n = number of electrons transferred; ΔH = Activation enthalpy; F = Faraday constant; R =

Universal gas constant; I_{po} = Pit current; t_{pit} = time for pit to reach threshold size; a_0 = initial pit depth; T = Temperature; ρ = density

After solving for "a" in Equation 25, one can use the "a" calculated from Equation 25 to find the modified threshold stress intensity:

$$\Delta K_{th} = Y\Delta\sigma\sqrt{\pi a}$$

Equation 26 - Where: Y = Geometric factor; $\Delta\sigma$ = Applied stress range

Akid noted that his calculation was based on a single defect controlling the lifetime of the material. This is not always reality (24). Akid also remarked the equation does not take into account the effect of cyclic frequency. At high frequencies corrosive chemicals may not have time to diffuse to the crack tip, negating the effects of corrosion fatigue.

Other methods of investigation in pit to crack transition involve electrochemical methods. For 316L stainless steel alloys Akid found that a sudden drop in corrosion current density marked the pit to crack transition (24). This critical current density can be used in part to determine the threshold stress intensity for the material. See Figure 28.
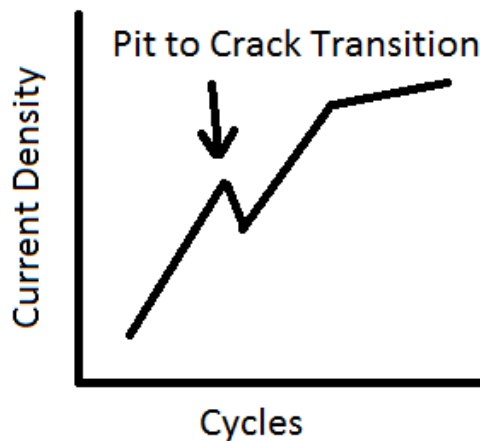
Figure 28 - Diagram of pit to crack transition. Diagram shows corrosion current of material.

5 Experimental Procedure

In this section the experimental procedures and equipment used are described. This project was split into two sections, the first studying the corrosion properties of the selected drillstring alloys and the second studying the fatigue properties for the selected drillstring alloys. The selected drillstring alloys are explained in section 6.1 Selected Materials

5.1 Flat Sample Preparation

Samples measuring 1.2 inches by 1.2 inches by 0.4 inches (3.05 x 3.05 x 1.02 cm) were machined from the drillpipe for S-135. Samples measuring 1.2 inches by 1.2 inches by 0.25 inches (3.05 x 3.05 x 0.63 cm) were machined from the drillpipe for UD-165. Samples were then ground from 60 to 1200 grit using silicon carbide sanding papers. The succession from 60 to 1200 grit was as follows: 60, 120, 240, 400, 600, 800, 1200 (SI: p2400). Flat samples were ground in this manner before each polarization experiment. Only the one face 1.2" x 1.2" face was polished. Flat samples were used for polarization measurements and pit growth experiments.

5.1.1 Immersion Sample Procedure

Flat samples were polished on all sides using the procedure from section 5.1 Flat Sample Preparation. A small 0.1 inch hole was drilled into a corner of the samples and the interior of the hole was covered with microstop. The samples were then weighed. One sample of each alloy was hung using thread in a 1 L plastic bottle, filling the bottle with 0.9 L of 6.7 M $CaCl_2$ solution. Samples were fully immersed for 8 weeks. After 8 weeks corrosion deposits were scraped off using a plastic spatula and placed in labeled containers. After noting locations of the corrosion products, samples were then cleaned by rinsing in Deionized Water (DIW) and acetone. Ultrasonic cleaning in methanol followed acetone rinsing. A final weight and dimension measurements were taken after ultrasonic cleaning.

5.2 Electrolyte Preparation

To prepare the electrolyte, 99.5% purity $CaCl_2$ pellets were mixed with DIW to a final concentration of 6.7 M. Because the adsorption of $CaCl_2$ in water is exothermic mixing was done in two steps. First 1 L DIW 375g $CaCl_2$ was mixed with the DIW and left to cool under a fume hood. After cooling for 5 hours another 375g of $CaCl_2$ was mixed in the solution for a final concentration of 6.7 M. This solution was left to cool overnight and was decanted the next morning.

Also, experiments were also conducted with a mix of 0.023 M Ca(OH)$_2$ with 0.067 M CaCl$_2$. To prepare this solution, 1.7 grams of 99.5% purity Ca(OH)$_2$ pellets was weighed and added to 1 L DIW. 7.5 g of 99.5% purity CaCl$_2$ pellets were then dissolved in the solution.

5.3 Experimental Setup for Polarization Experiments

Polarization curves were generated using a Schlumler SI 1286 Electrochemical Interface potentiostat. The potentiostat holds the electrochemical electrodes at a specific voltage and measures current flowing though the cell or vice versa. The potentiostat measures voltage against a reference electrode and counter electrode and the sample to be measured; for this project the reference cell used was the Saturated Calomel Electrode (SCE) and a platinum electrode functioned as the counter electrode. The potentiostat sweeps through set potential limits to form a potentiodynamic curve. Scan rates used were 60 V/hr and 0.6 V/hr.

The potentiostat was controlled via a PC using Corrware v2.9b2 software. See Figure 29 for a diagram of the experimental setup.
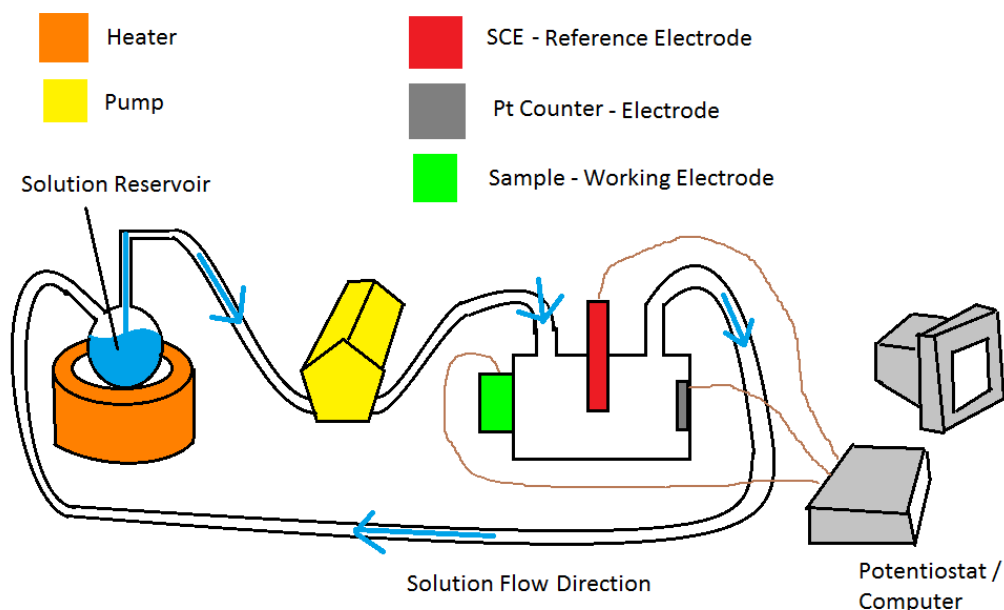
Figure 29 - Diagram of experimental setup for polarization curves

5.3.1 Electrochemical Experimental Parameters

The effect on scan rate, oxygen content and temperature on the pitting potential in saturated CaCl$_2$ (6.7 M) was investigated in this project. This leaves eight parameters to be measured for each alloy. See Table 1 for a table of the experimental parameters.

PITTING POTENTIALS		OPEN AIR		DEAERATED	
		0.6 [V/hr]	60 [V/hr]	0.6 [V/hr]	60 [V/hr]
S-135	20 [°C]				
	80 [°C]				
UD-165	20 [°C]				
	80 [°C]				

Table 1 - Table showing the experimental parameters

5.3.2 Polarization Experiments Procedure

To measure polarization curves, a procedure similar to ASTM standard G5 (30) was adopted. Polished flat samples were inserted into the Modified Avesta Head (MAH) cell with a 1 cm^2 exposed area (working electrode in Figure 29). Solution pumped though the cell at a rate of 0.4 L/min. DIW flowed though the MAH at a rate of 0.2 mL/hr to stop crevice corrosion. A cathodic polarization was applied to the samples for 30 seconds upon immersion into solution to remove any air formed film on the sample surface. The Open Circuit Potential (OCP) was measured by the potentiostat for 55 minutes prior to polarization measurements. Heating using a Omega CSC32 temperature controller and argon deaeration took place as needed during this 55 minute measurment of the OCP. Solution deaeration was achieved by bubbling argon gas in the solution reservoir in Figure 29. The pH of the solution was recorded before and after polarization experiments in the solution reservoir by Oyster Model 6012B pH probe.

There were two polarization curves generated for each experiment, each requiring a fresh sample. For Potentio-Dynamic (PD) curves, the potentiostat was programmed to begin measuring at 0.10 V below OCP and stop measuring at 0 V against SCE. For Cyclic Voltrammgrams (CV), the potentiostat was programmed to measure from 0.1 V below OCP to 0.1 V above the pitting potential back down to 0.1 V against SCE below OCP. Pitting potentials were determined from PD scans by finding the potential that correlated to a current density of 0.001 A/cm^2. See Figure 30**.**
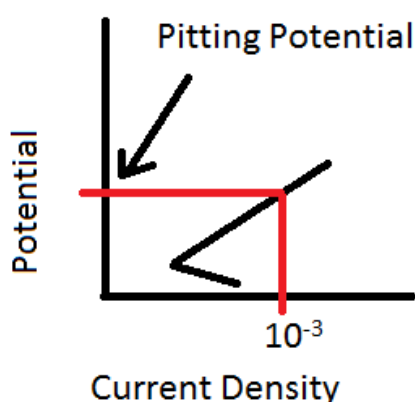
Figure 30 - Diagram showing how pitting potential was selected

It should be noted that "pitting potential" is an arbitrary term, set by the author in this thesis. The scientific definition of pitting potential is the potential at which the anodic dissolution rate is slightly higher than the repassivation rate (14). For the alloys studied the repassivation potential was in the catholic region of the polarization curves meaning that pitting could be observed at any anodic potential. In efforts to consistently and quickly pit the samples, a pitting potential correlating to a current density of 0.001 A/cm^2 was chosen.

While using the MAH yielded valid results many experiments were lost due to crevice corrosion. Attempts to control crevice corrosion by increasing the DIW flow rate to the MAH were unsuccessful. The MAH was replaced with a standard cell with 3 cm^2 exposed area. Polished samples were covered with microstop leaving a circular exposed area of 0.95 cm in diameter and 0.71 cm^2 area.

5.3.3 Pit Growth Experimental Procedures:

To pit samples, the potentiostat was programmed to hold samples at a pitting potential for 30 seconds and then hold the sample at a propagation potential for a desired time. The propagation time was the experimental variable.

A similar procedure to Section 5.3.2 Polarization Experiments Procedure was used for pitting. Flat samples were polished to 1200 grit and inserted into the standard cell. Cathodic polarization to remove air formed surface films was applied upon immersion for 30 seconds, followed by measuring OCP for 55 min with heating or argon deareation as necessary prior to electrochemical experimentation. The potentiostat was then programmed to hold the sample at a pitting potential

for 30 seconds to generate pitting damage and then hold the sample at a propagation potential for a 7.5 minutes. Preliminary pitting measurements were done at three and 30 minutes of propagation to see if pit growth was observed. After pitting was observed through the preliminary tests a propagation interval of 7.5 minutes was chosen.

At the conclusion of each propagation interval, the sample was removed from the cell and rinsed with DIW and rubbed with a piece of rubber to remove corrosion products and then dried with compressed air. The pitting damage was then measured using optical profilometry. Optical profilometry uses a interference pattern to scan though the focus of an optical microscope to measure depth of features. Optical profliometery is a nondestructive method, using a MicroXAM-100 optical microscope and is controlled using a PC with MapVue AE, version 1.25.3.

After measuring pit depth via optical profilometry samples were reinserted into the standard cell and propagated and remeasured until 45 minutes of propagation time has elapsed. The pH of the fresh solution was measured initially and at the conclusion of the experiment.

A plot of pit depth against polarization time was then constructed using the pit depths measured by the optical profilometry method.

5.4 Fatigue Lifetime Procedure:

Standard hourglass specimens using ASTM standard E-466 (31) were prepared for fatigue experiments. The samples had a gauge length of 0.4" (1.02 cm) with a diameter of 0.2" (5.1 cm) as shown on Figure 31. The gauge length on the fatigue specimens was polished to a 1200 grit (P4000) finish.
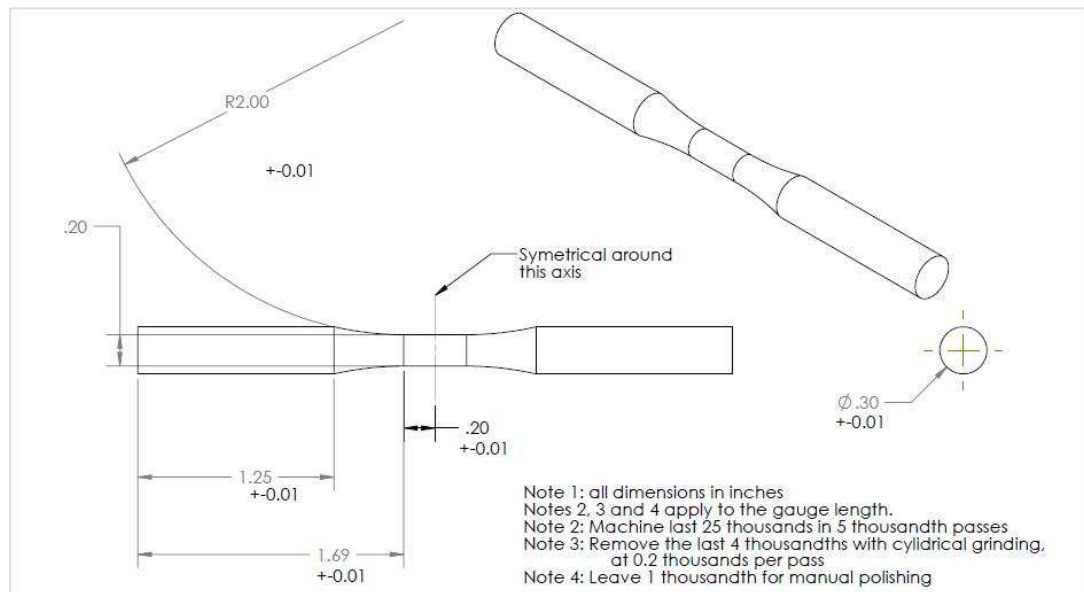
Figure 31 - Fatigue specimen design

An MTS 810 servo-hydraulic materials test system was used to stress the hourglass samples. The MTS 810 was controlled by a Fast Track 8800 Instron controller using console software version 8.2.149. Wave Matrix V1.3.232.0 software was programmed to stress the samples using a sine wave function from compression to tension (R=-1) at 15 hz. Samples were programmed to run to 10^6 cycles or until the input loading wave differed from the measured load by 10%, indicating failure.

A minimum of three samples were fatigued per stress level. Fatigue tests were done on polished (virgin) and pitted samples. Both cases used the procedure outlined above.

For UD-165, stress amplitude levels of 675, 700, 750, 825 and 875 MPa were used for pitted and virgin states. For samples pitted and then left in ambient environment for 2 weeks as outlined in section 5.4.2 Fatigue Specimen Pitting Procedure - Aging prior to stressing them at 700, 750 and 825 MPa were used.

For S-135, stress amplitude levels of 600, 625, 675, 725 and 775 MPa were used on virgin samples. For pitted samples stress levels of 600, 675, 725, and 775 MPa were measured. For pitted samples left in ambient environment for 2 weeks, stress amplitude levels of 600, 675 and 725 MPa were used.

5.4.1 Fatigue Specimen Pitting Procedure

The fatigue specimens were masked with microstop, leaving the gauge length exposed for pitting. Fatigue samples were pitted in a green cell instead of the standard cell due to the round geometry of the samples. The solution was left stationary in the green cell. No heating or deaeration was done. A diagram of the experimental setup can be seen in Figure 32**.**
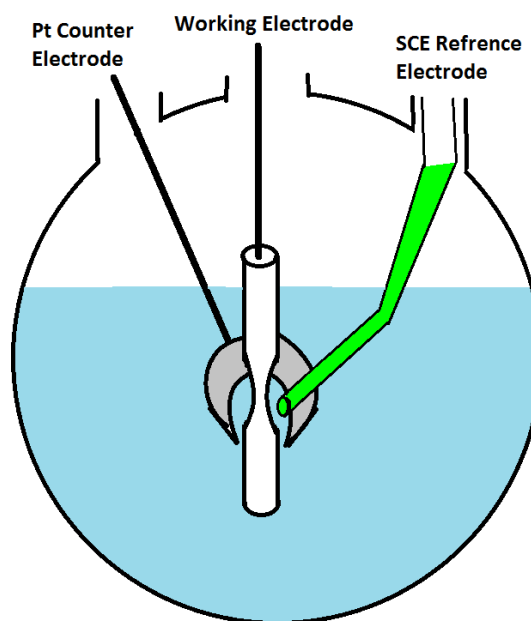
Figure 32 - Green cell setup

The results of the polarization curves studied from the flat samples in the standard cell indicated that no protective film was formed from heating or deaeration. Observing that no major changes in electrochemical behavior were seen by heating or deaeration, the simplest experimental set up was chosen for pitting the fatigue specimens.

Polarization was applied immediately upon immersion into the 6.7 M $CaCl_2$ solution. The potentiostat was programmed to hold the cell at a current density of 0.001 A/cm^2 for 5 minutes. After anodic polarization the sample was then removed from the green cell and rinsed with DIW and dried with compressed air.

After drying with compressed air, samples were fatigued as outlined in section 5.4 Fatigue Lifetime Procedure:.

A few samples were selected for optical profilometry. The same optical profilometer and software was used as in section 5.3.3 Pit Growth Experimental Procedures:**.** Twenty random areas measuring 173 by 128 square micrometers on the fatigue specimens were selected per alloy for pit depth measurement using optical profilometry.

Pit density was determined by counting pits per 173 by 128 square micrometer area and dividing the number of pits by the measured area. Pit depths were categorized in the following depths in micrometers: 1-1.4;1.5-1.9; 2-2.4; 2.5-2.9; 3-3.4; 3.5-3.9; 4-4.5; 4.5+.

5.4.2 Fatigue Specimen Pitting Procedure - Aging

It was selected to measure the effects of airborne corrosion on the fatigue specimens. Fatigue specimens were pitted as in section 5.4.1 Fatigue Specimen Pitting Procedure**.** They were then rinsed with DIW and dried with compressed air. After drying the samples were left in the lab at 20-25°C at 20-35% humidity for 14-18 days before fatigue testing.

6 Experimental Results

In this section the various results of electrochemical and fatigue data are presented. This project was split into two sections, the first studying the corrosion properties of the selected drillstring alloys and the second studying the fatigue properties for the selected drillstring alloys.

6.1 Selected Materials

S-135 is the highest strength alloy that meets American Petroleum Institute (API) requirements for High Strength Low Alloy (HSLA) steel as of 2008. Z-140 and V-150 have been produced but not widely used. UD-165 is being considered for UDD applications (2) (3) (32). For sour environments (H_2S containing), stainless steel alloys are used (32). HSLA steels are desirable over stainless steel and titanium alloys due to their low cost and increased fluid efficiencies (2).

6.1.1 Selected materials - Mechanical Properties

Five alloys were acquired from NOV Grant Prideco for this project. Alloys acquired are listed in Table 2. Ultimate Tensile Strength (UTS), Yield Strength (YS) , %Elongation, and reduction of area are reported data from the manufacturer for alloys. Hardness testing was done according to ASTM standard E-18 0b (33).

	UTS [Mpa]	Yield [Mpa]	Elongation [%]	Reduction Area [%]	Hardness [Rc]
S-135	1168	1096	19	69.7	35.1
XD-105	855	752	27.9	67.3	23.9
Z-140	1103	1018	19.5	65	33.7
V-150	1193	1094	17.7	63.3	34.9
UD-165	1278	1183	23.7	nf	40.1

Table 2 - Mechanical properties of various drilling alloys.

This project has chosen to study S-135 as it meets API requirements and UD-165 as it is had the highest yield strength of the drilling alloys acquired for this project. See Table 3 for the specific alloying elements for S-135 and UD-165. Chemical compositions were outsourced to IMR test labs.

Element	Al	B	C	Cr	Cu	Mn	Mo	N
S135	0.03	<0.005	0.26	1.39	0.02	0.78	0.68	0.005
UD165	0.03	<0.005	0.27	0.79	0.19	0.88	0.67	0.007
Element	Nb	Ni	P	S	Si	Sn	Ti	V
S135	<0.01	0.02	0.006	0.002	0.3	<0.01	<0.01	<0.01
UD165	0.02	0.81	<.005	0.007	0.26	<0.01	<0.01	0.07

Table 3 - alloy elements for S-135/UD-165 in weight percent. Sulfur and Carbon determined by combustion-infrared absorbance. Nitrogen determined by inert gas fusion-thermal conductivity. All other elements found by ASTM E1019-08 and CAP-017J (ICP-AES) (34).

6.1.2 Selected Materials - Microstructure

Samples of UD-165 and S-135 were polished and etched to reveal the microstructure. Samples were polished to 5 μm finish and etched with Nital. Both samples show martensitic microstructures as show in Figure 33 and Figure 34.
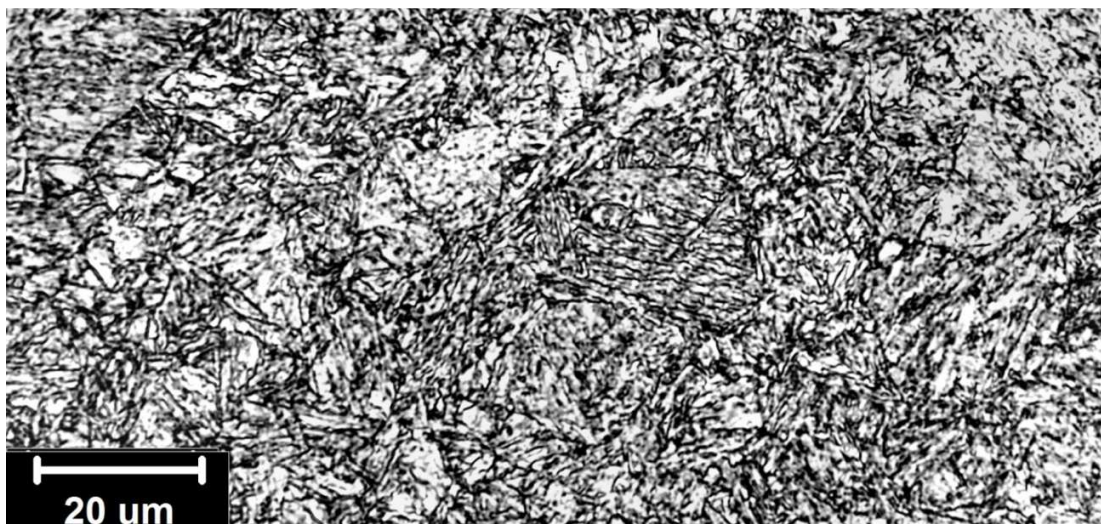
Figure 33 - Microstructure of S-135
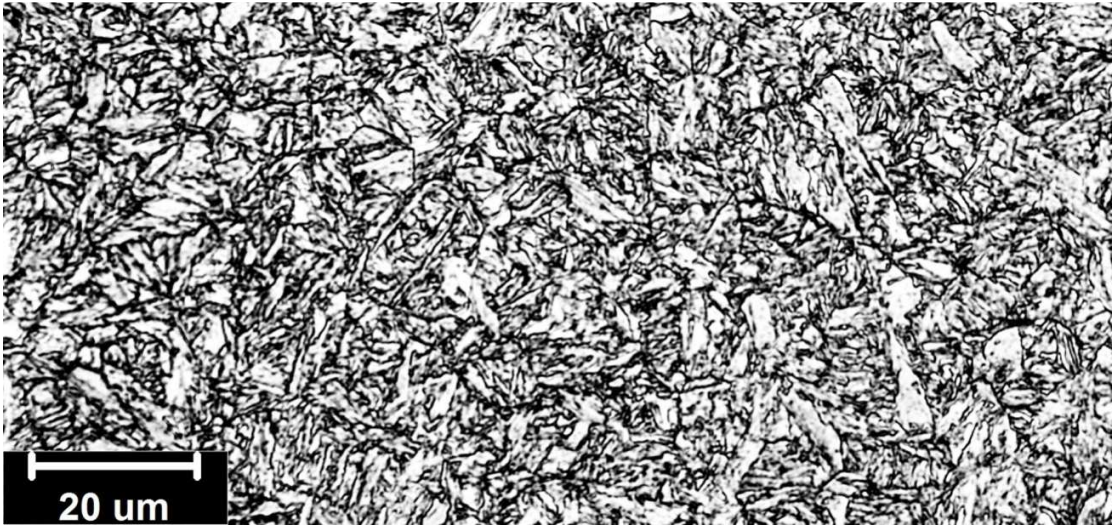
Figure 34 - Microstructure of UD-165

6.1.3 Selected Materials - Defects

Materials in the real world have defects. Defects arise from the manufacturing process and alloying elements. Non-metallic inclusions can form from alloying elements and dirt from the casting process. Once formed, these non-metallic inclusions have different coefficients of thermal expansion which may cause an internal fracture of the nonmetallic inclusion from the surrounding metal matrix.

Nonmetallic inclusions serve to block dislocation movement and are observed to initiate pitting corrosion. Figure 35 and Figure 36 show examples of inclusions found on S-135 and UD-165 respectively.
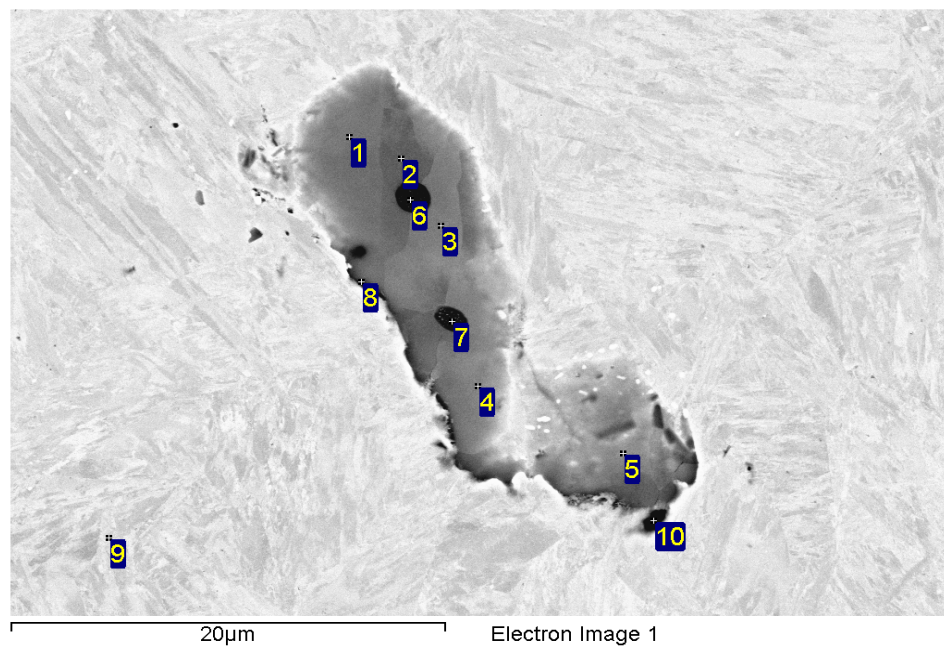
Figure 35 - SEM image of an inclusion in S-135. Manganese and Sulfur found using Electron Dispersive Spectroscopy (EDS).
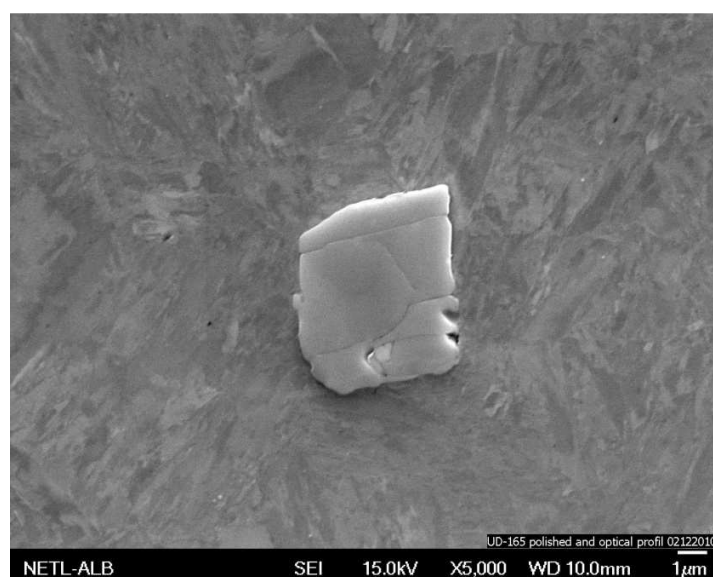
Figure 36 - SEM image of an inclusion in UD-165. Niobium and Carbon found using EDS.

Scanning Electron Microscopy (SEM) of the as polished surface revealed that approximately 0.1% of the surface has defects for both alloys. Both S-135 and UD-165 showed inclusions with traces of sulfur, manganese, aluminum, silicon, chromium and oxygen. S-135 had many

inclusions that were rich in Mn, S, and Al. Carbon and Silicon appeared to be coupled; one inclusion was found to be rich in C and Si, indicating polishing media may have embedded in the inclusion. The rest of the inclusions for S-135 seemed to show traces of Si and C. Likewise in other inclusions found on S-135 Mn and S were coupled, while only traces of Al, Si, and C were apparent. Elements were found using Energy Dispersion Spectrography (EDS).

For UD-165, Nb and C seemed to be coupled, as shown in Figure 36 where an inclusion was found to be rich in Nb and C. Other inclusions in UD-165 showed traces of C and no Nb. Other inclusions in UD-165 showed Fe, Al and O rich areas with only traces of C.

6.2 Experimental Results - Immersion Testing

Samples were immersed in 6.71 M $CaCl_2$ solution for 8 weeks to determine the susceptibility to corrosion. Localized pitting was observed underneath corrosion deposits. Through X-Ray Diffraction (XRD) the corrosion deposits show a FeOOH like phase. There was no measureable weight change in the samples therefore a corrosion rate was not calculated by weight loss measurements.
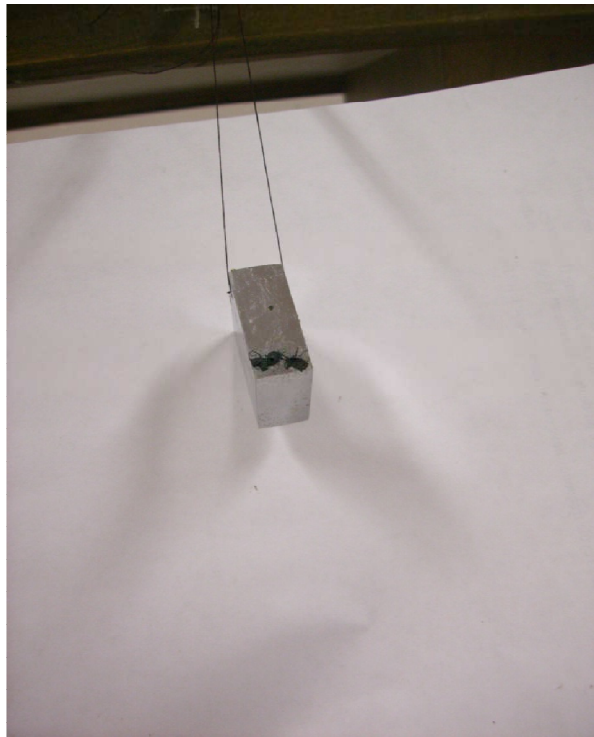
Figure 37 - Local corrosion observed from immersion testing. S-135 after 8 weeks of immersion. Thickness of sample is 0.4".
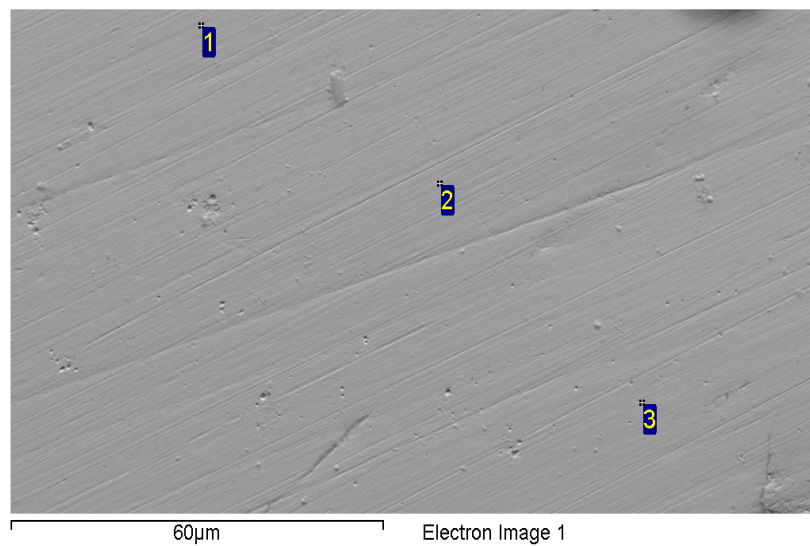
Figure 38 - SEM image of S-135 after 8 weeks of immersion, showing polished surface after immersion.
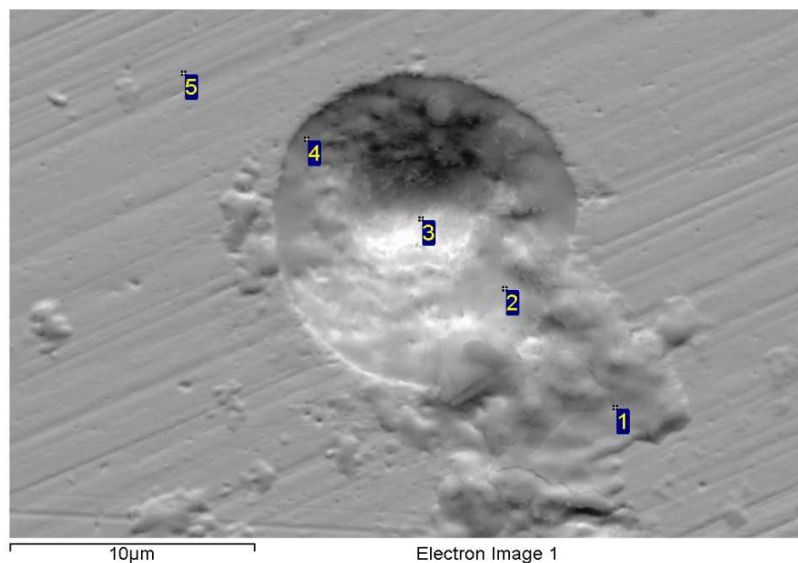
Figure 39 - SEM image of S-135 after 8 weeks of immersion, showing pit and local corrosion products

From Figure 37-Figure 39 it is apparent that the surface of the sample is still highly polished post immersion. This indicates that significant general corrosion did not occur. Presence of a FeOOH compound found from XRD indicates that a passive, non-protective film is formed at the sites of pits.

Very little control of pit density or pitting depth can be obtained through immersion testing. It is also undesirable to use this method for pitting due to the large amount of time per sample needed. The following sections are the results of the accelerated corrosion techniques.

6.3 Experimental Results 3.5 g/L NaCl

It was chosen to investigate the behavior of the steels in simulated sea water. Sea water is commonly used as a completion fluid. The chosen laboratory substitute for sea water is 3.5 g/L NaCl. Electrolyte was prepared by adding 3.5 g of laboratory grade NaCl to DIW. The experimental procedure is outlined in section 5.3.2 Polarization Experiments Procedure.
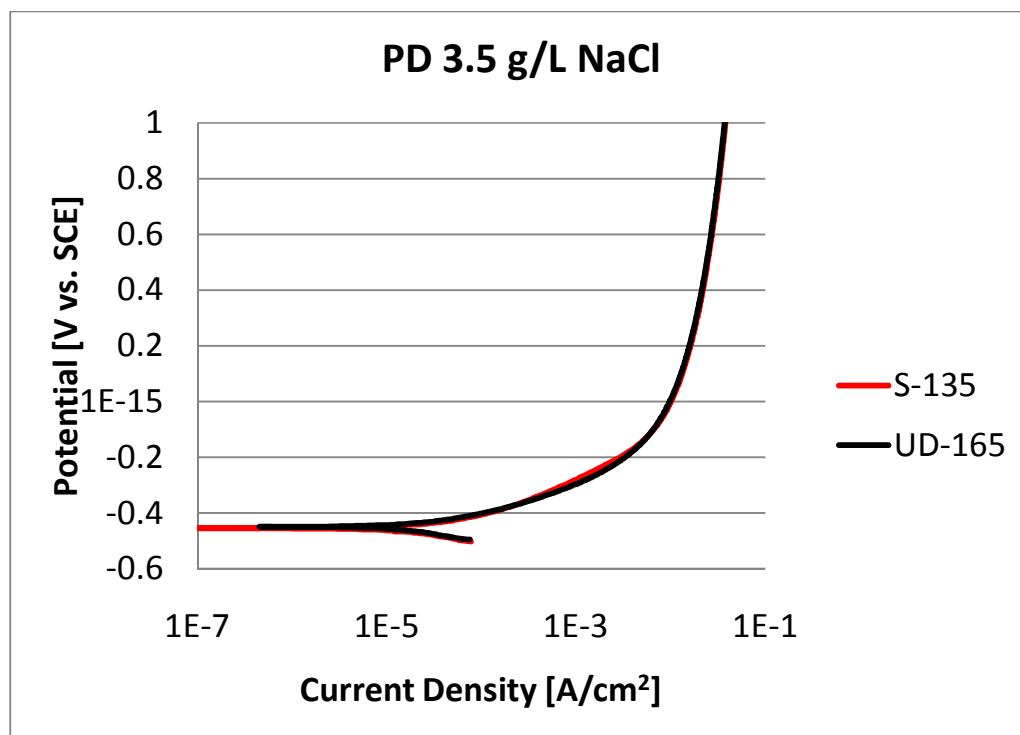
Figure 40 - PD scan of S-135 (red) and UD-165 (black) in 3.5g/L NaCl, at 16.7 mV/s at 20°C. Open Air solution.

As shown in Figure 40 only active dissolution followed by mechanical passivation is observed in laboratory sea seawater. This indicates no protective oxide film is developed on the surface.

Due to the lack of a passive oxide film formation, further investigation in simulated oceanic water was not performed.

6.4 Experimental Results - Polarization Curves for CaCl₂

Displayed in Figure 41-Figure 45 are the results of the PD scans for S-135 in 6.7 M CaCl₂. Displayed in Figure 46-Figure 50 are the results of the PD scans for UD-165. These results were performed using the procedures outlined in section 5.3.2 Polarization Experiments Procedure.
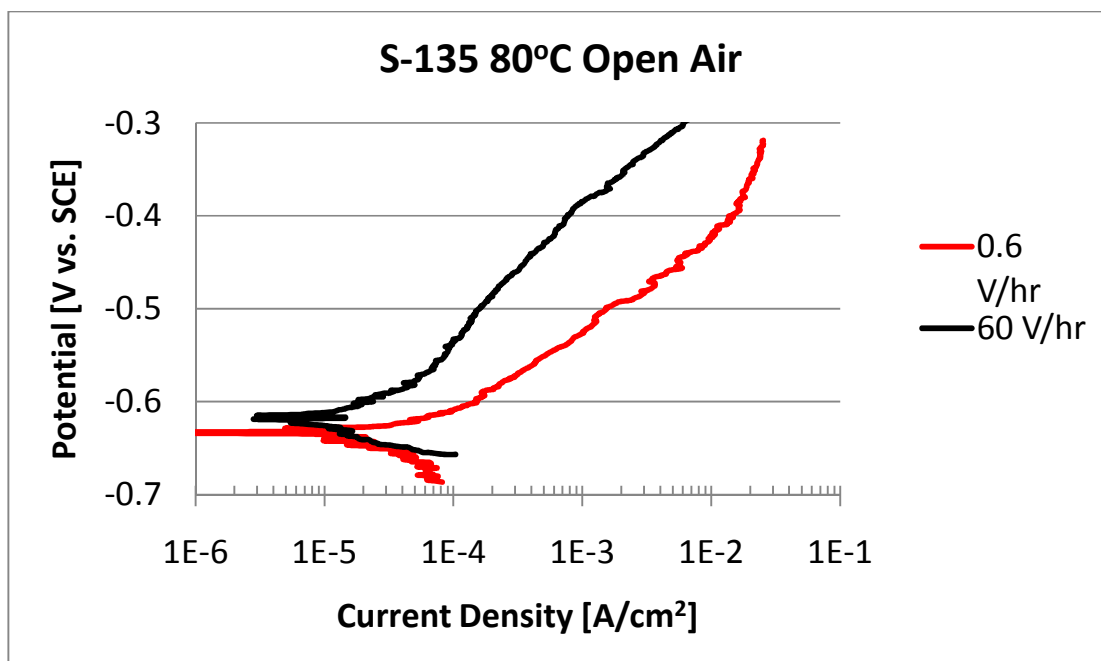
Figure 41 - PD scan of S-135 at 80°C in 6.71 M CaCl₂ solution in open air. Figure shows effect of increased scan rate.
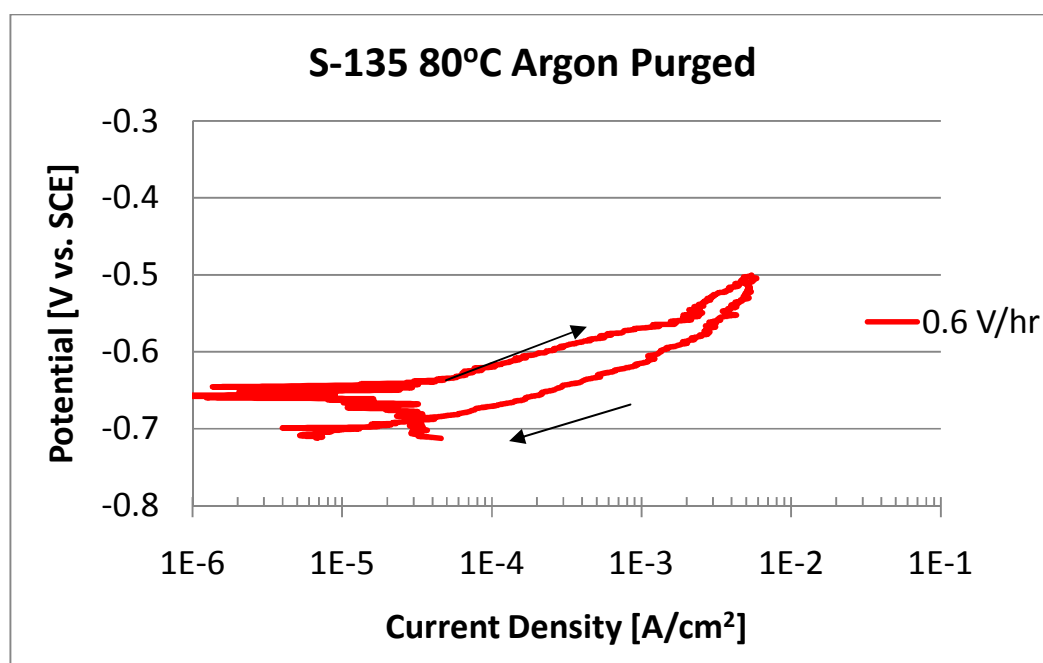
Figure 42 - PD scan of S-135 at 80°C with scan rate of 0.167 mV/s in 6.71 M CaCl₂ argon purged solution. Fast scan rates were not performed under this condition. Arrows indicate scan direction.
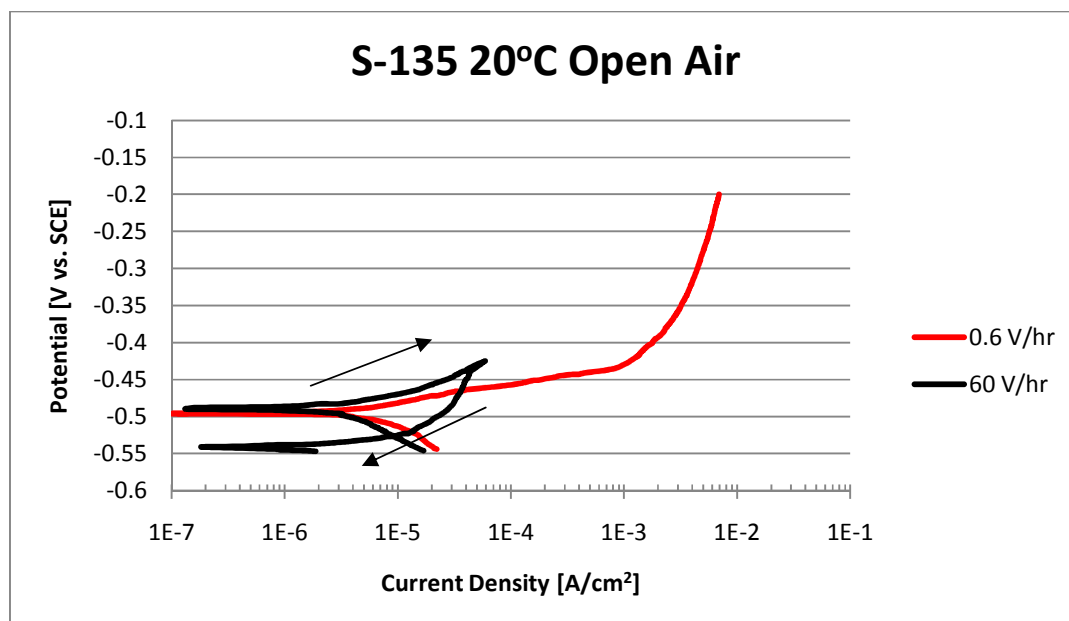
Figure 43 - PD scan of S-135 at 20°C in 6.71 M CaCl₂ solution in open air. Figure shows effect of scan rate. Arrows indicate scan direction.
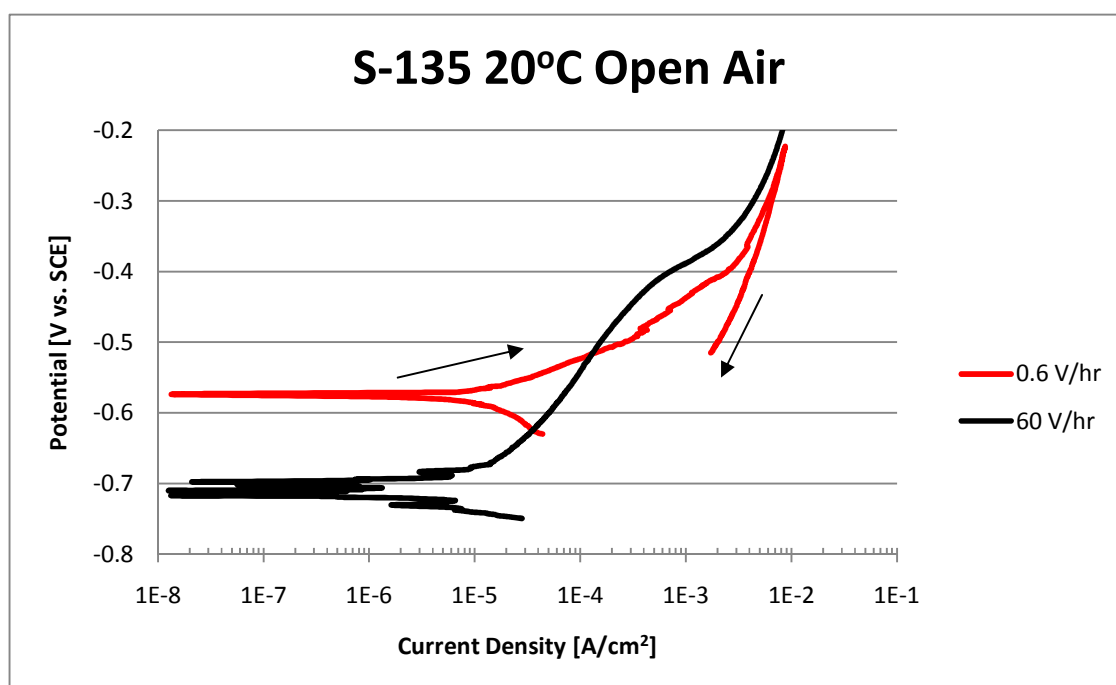
Figure 44 - PD scan of S-135 at 20°C in 6.71 M CaCl₂ argon purged solution. Figure showing effect of scan rate. Arrows indicate scan direction.
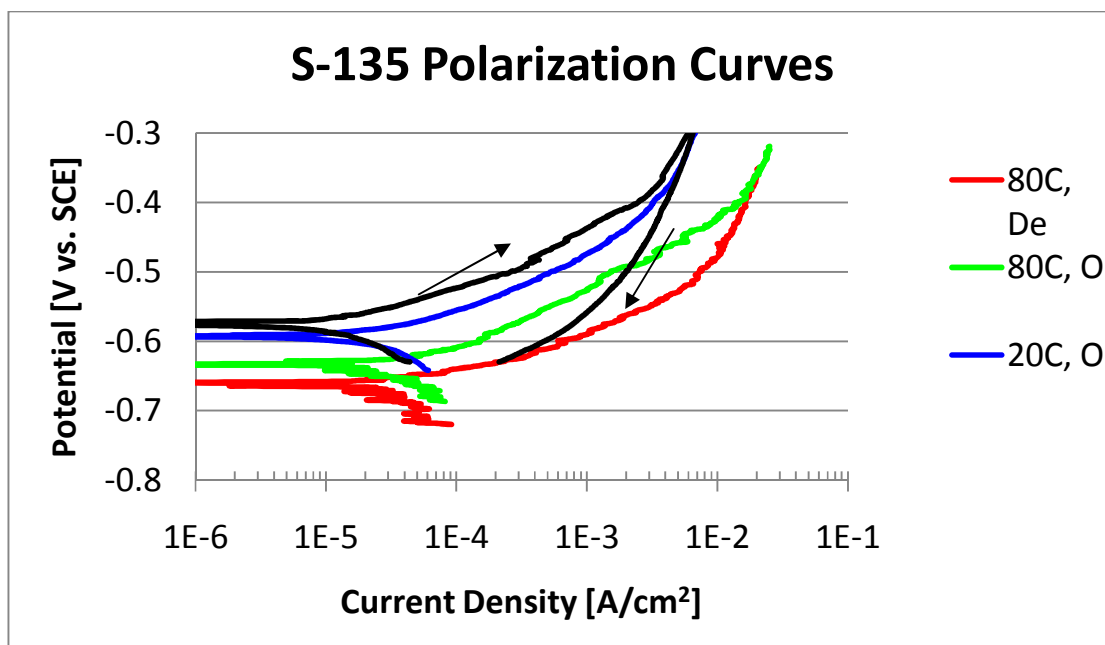
Figure 45 - PD scan of S-135 under various conditions with a scan rate of 0.6 V/hr. Figure shows effect of deaeration and temperature. DE = Deaeration, O = Open air. Arrows indicate scan direction.
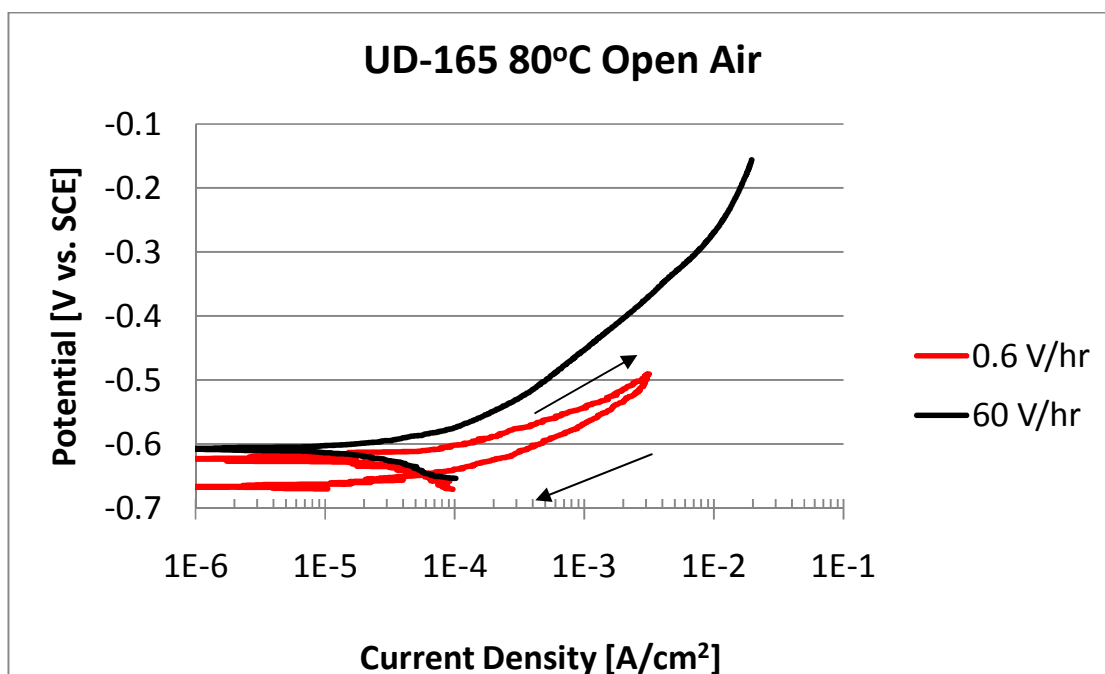
Figure 46 - PD scan of UD-165 at 80°C in 6.71 M CaCl₂ solution in open air. Figure showing effect of scan rate.   Arrows indicate scan direction.
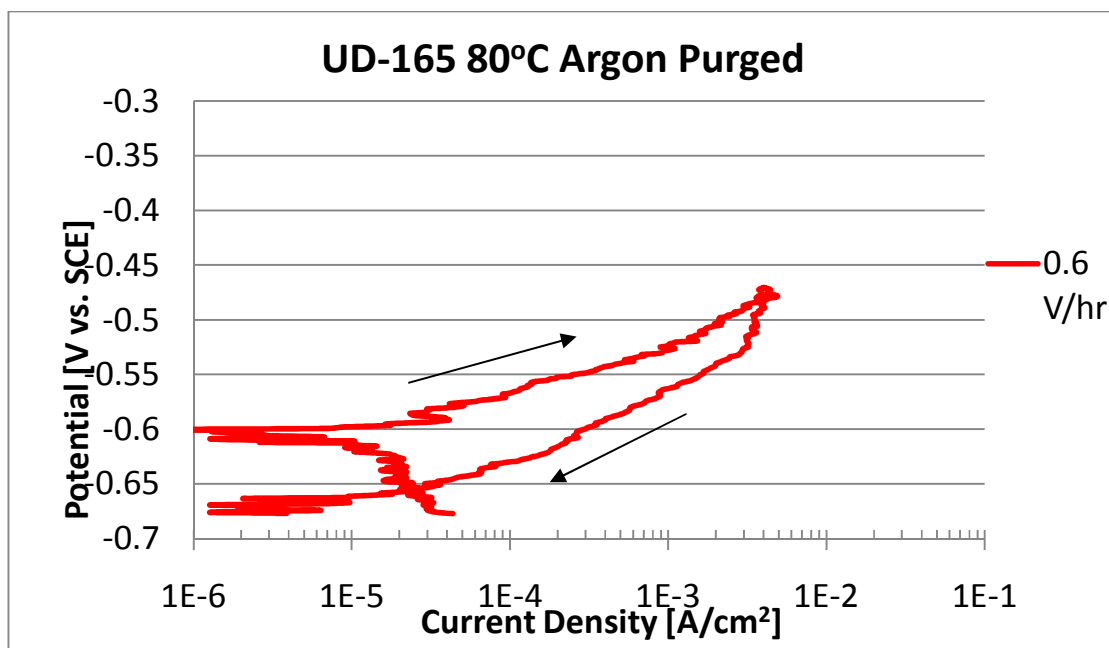
Figure 47 - PD scan of UD-165 at 80°C with scan rate of 0.167 mV/s in 6.71 M CaCl₂ argon purged solution. Faster scans were not performed for this condition. Arrows indicate scan direction.
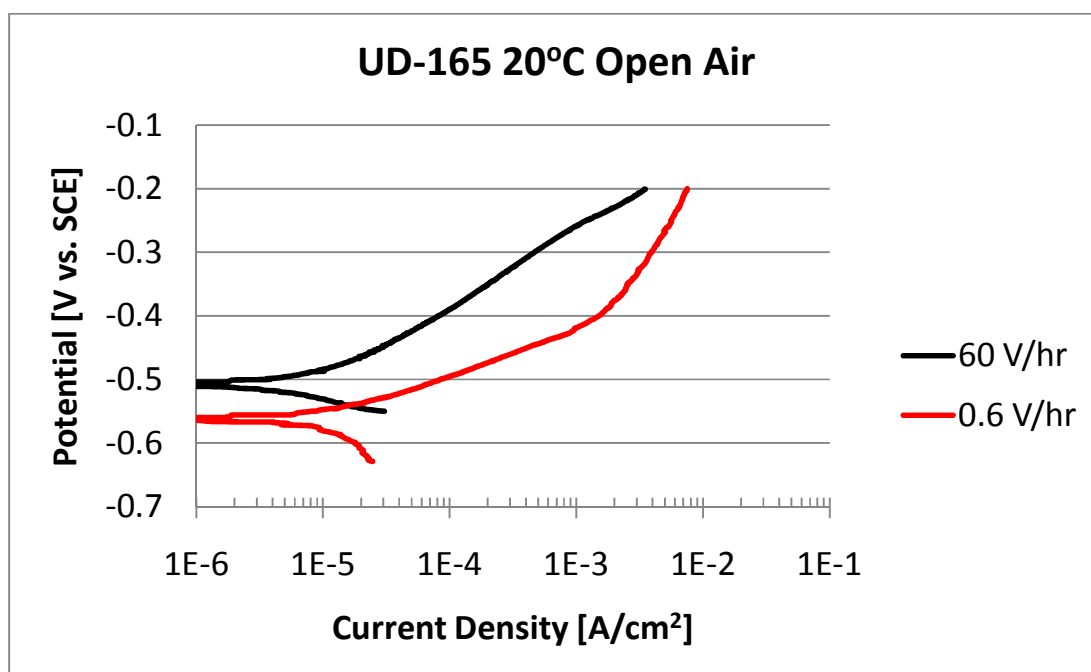
Figure 48 - PD scan of UD-165 at 20°C in 6.71 M CaCl₂ solution in open air. Figure shows effect of scan rate.
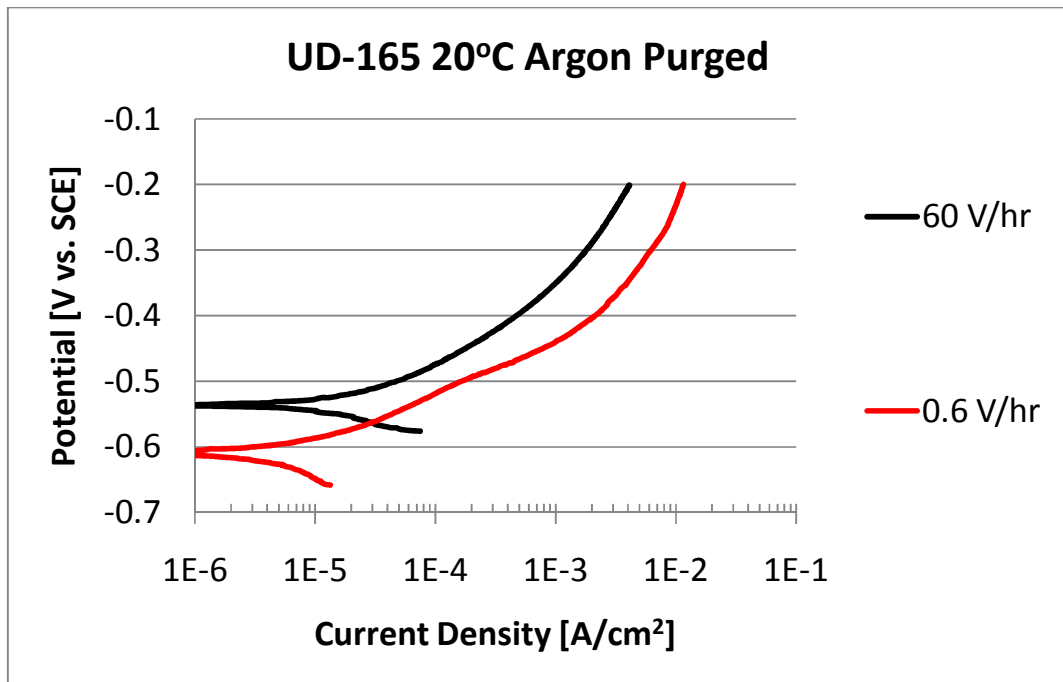
Figure 49 - PD scan of UD-165 at 20°C in 6.71 M CaCl$_2$ solution argon purged. Figure showing effect of scan rate.
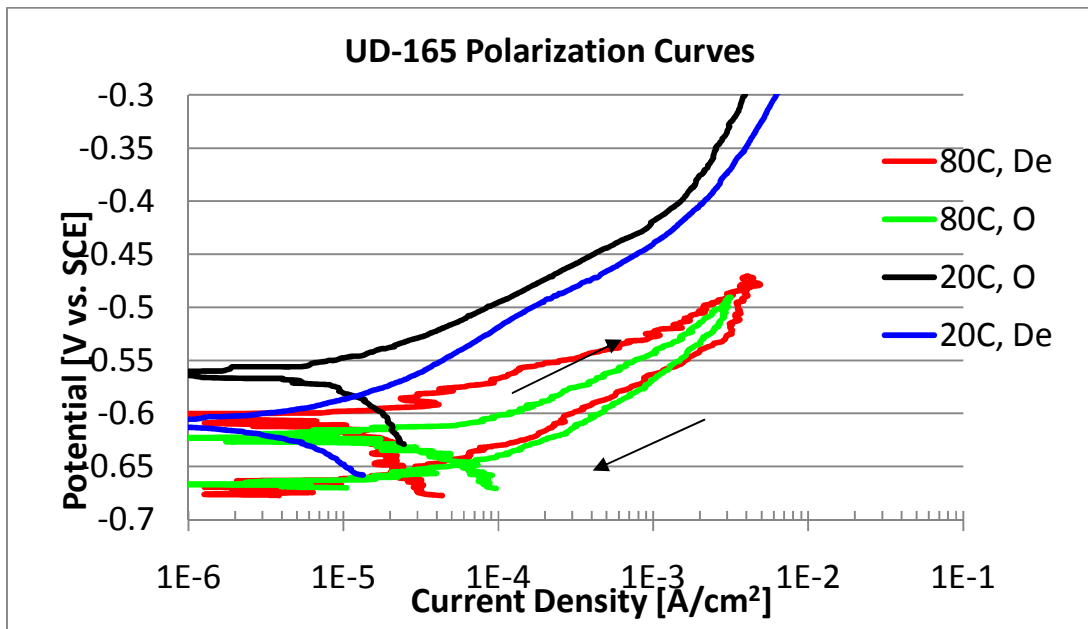
Figure 50 - PD scan of UD-165 under various conditions with a scan rate of 0.6 V/hr. Figure shows effect of deaeration and temperature. DE = Deaeration, O = Open air. Arrows indicate scan direction.

Displayed in Table 4 are the pitting potentials found using the general polarization procedure.

PITTING POTENTIALS		OPEN AIR		DEAERATED	
		0.6 [v/hr]	60 [v/hr]	0.6 [v/hr]	60 [v/hr]
S-135	20 [c°]	-0.44	-0.40	-0.44	-0.47
	80 [c°]	-0.53	-0.38	-0.38	nf
UD-165	20 [c°]	-0.42	-0.26	-0.44	-0.35
	80 [c°]	-0.54	-0.45	-0.53	nf

Table 4 - Pitting potentials of selected alloys. Reported voltages are against SCE.
Nf = Not Found

After experimentation the surface of the samples showed pitting damage and areas of general corrosion depending on the final voltage reached in the PD scans. It was observed that after holding samples at current densities around, or greater than, 10^{-2} A/cm^2 that mechanical passivation was observed.

Because the reverse scan of the CV scans crosses in the cathodic region, the cell has enough energy to form pits anywhere upon the anodic region. Because of the crossing in the cathodic region a repassivation potential is not observed and a conventional "pitting potential" defined as the potential at which the anodic dissolution rate is slightly higher than the repassivation rate (14) was not found. A pitting potential correlating to a current density of 10^{-3} A/cm^2 was chosen to quickly initiate pits on fatigue samples.

From optical investigations, Figure 51 and Figure 52**,** pits were observed on the surface after PD/CV scans.
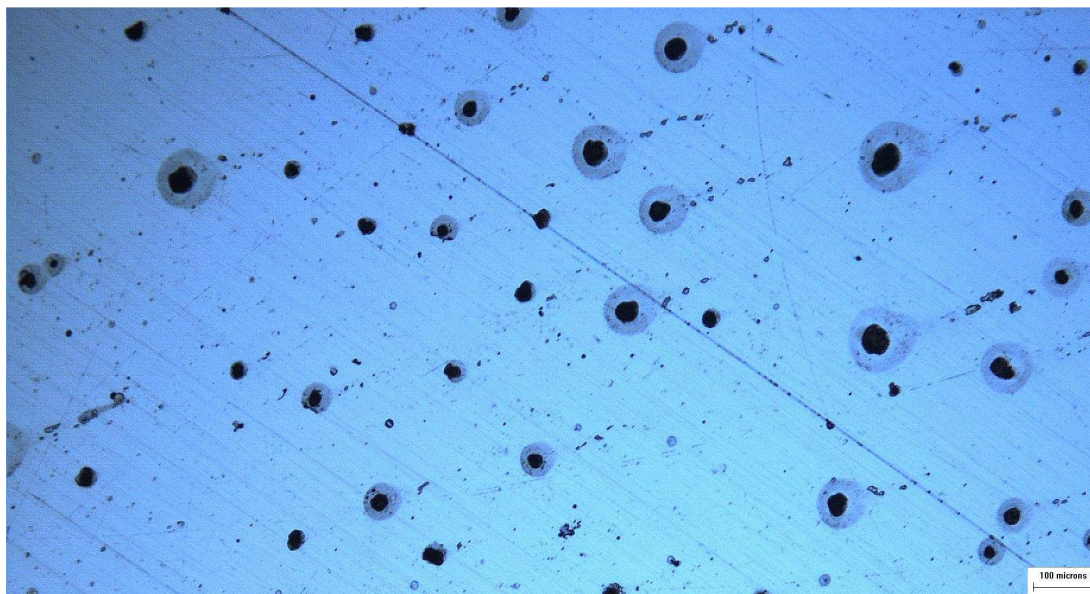
Figure 51 - Optical photograph of surface after PD scan 20°C open air solution 0.6 V/hr, S-135. Evidence of pitting corrosion is present.
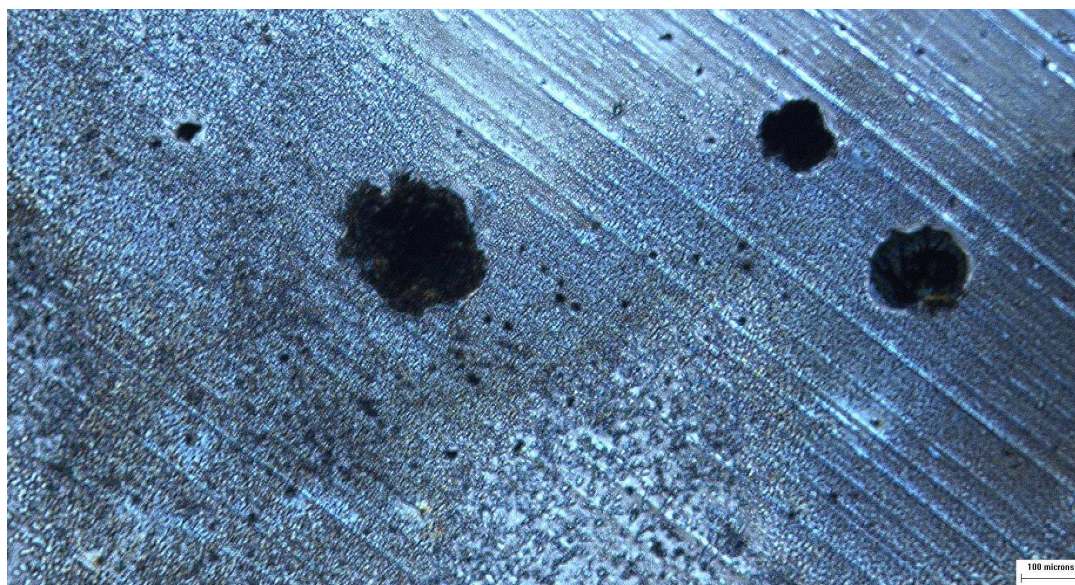
Figure 52 - Optical photograph of surface after PD scan 20°C open air solution 0.6 V/hr, UD-165. Evidence of pitting corrosion is present.

Indication of a protective oxide layer was not observed under any condition tested (temperature, oxygen concentration, scan rate) for 6.7 M $CaCl_2$ solutions. An attempt to form a protective film and control pit growth was attempted by making the electrolyte more basic by the addition of $Ca(OH)_2$.

6.5 Experimental Results - 0.023 M Ca(OH)₂ Solution

By looking at the Pourbaix diagram (Figure 8,p10) for iron in water the presence of a protective oxide film is observed under high pH solutions. Investigations inducing a protective oxide film are described in this section. As outlined in section 2.4 Pitting Corrosion, in Wranglen's pit growth model, a protective film is needed for an auto-catalytic pit growth. It was attempted to study the effects of a protective film in order to achieve pit growth and control.

The experimental procedure and preparation for experiments is outlined in section 5.3.2 Polarization Experiments Procedure. In the interest of time the only solution conditions explored were with solution open to air with a temperature of 20°C.
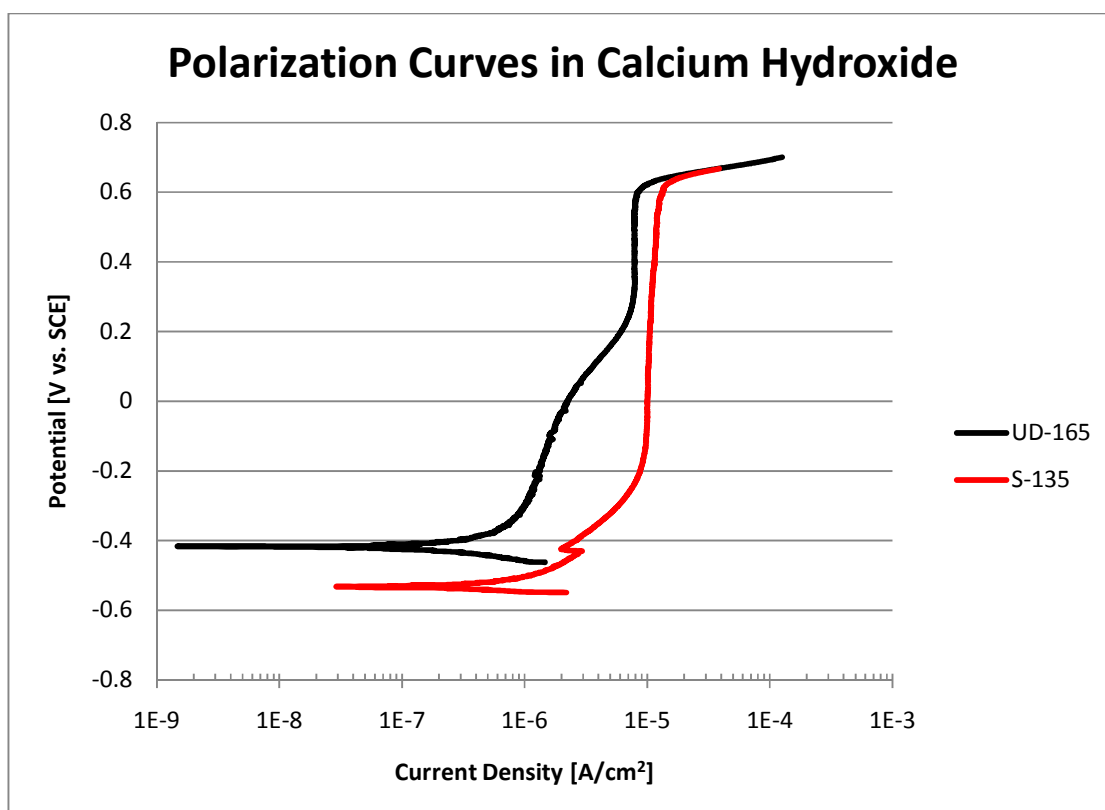
Figure 53 - PD scan of S-135 and UD-165 in 1.8g/L Ca(OH)₂, at 16.7 mV/s at 20°C.

As seen in Figure 53 an increase in electrode potential does not correlate to an increase in current density for a solution of 0.23 M Ca(OH)₂. This correlates to a protective passive film formation. From the affirmation of forming passive layer in Ca(OH)₂ solution, it was decided to investigate the effect of chlorine ions in the solution to see if it could break down the passive film.

Calcium chloride was added to the Ca(OH)$_2$ solution to attempt to break down the passive film. Experiments with an addition of 74.5g/L, 7.5g/L, 5g/L, 4g/L, 3g/L 2g/L and 1g/L of CaCl$_2$ with 1.8g/L Ca(OH)$_2$ were performed. Hysteresis loops were present in all CV scans with the exception of the addition of 1g/L of CaCl2. Therefore the breakdown concentration of CaCl$_2$ was in between the addition of one and two grams of CaCl$_2$.

Potentiodynamic scans and subsequent pitting experiments were performed in this solution of: 0.7 M CaCl$_2$ (7.5 g CaCl$_2$) and 0.023 M Ca(OH)$_2$ per liter of DIW. This solution will be referred to as "basic salt". It was chosen to increase the concentration of chlorine ions from 2g/L to 7.5 g/L to guarantee hysteresis.
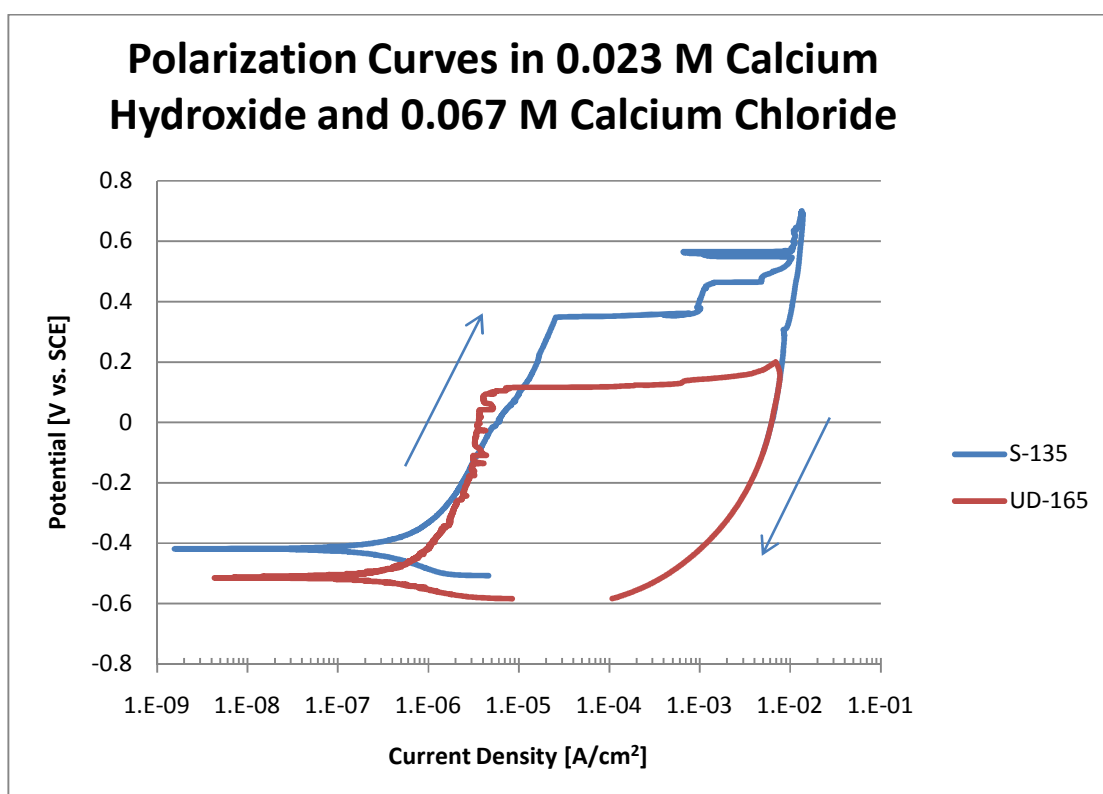
Figure 54 - CV scan of UD-165 and S-135 in basic salt solution. Experiments preformed at room temperature, (20°C) and in open air solution.

From Figure 54 both alloys are susceptible to pitting corrosion in the basic salt solution as shown by the observed hysteresis loop. Optical investigation showed a mix of general corrosion and pitting (Figure 55).
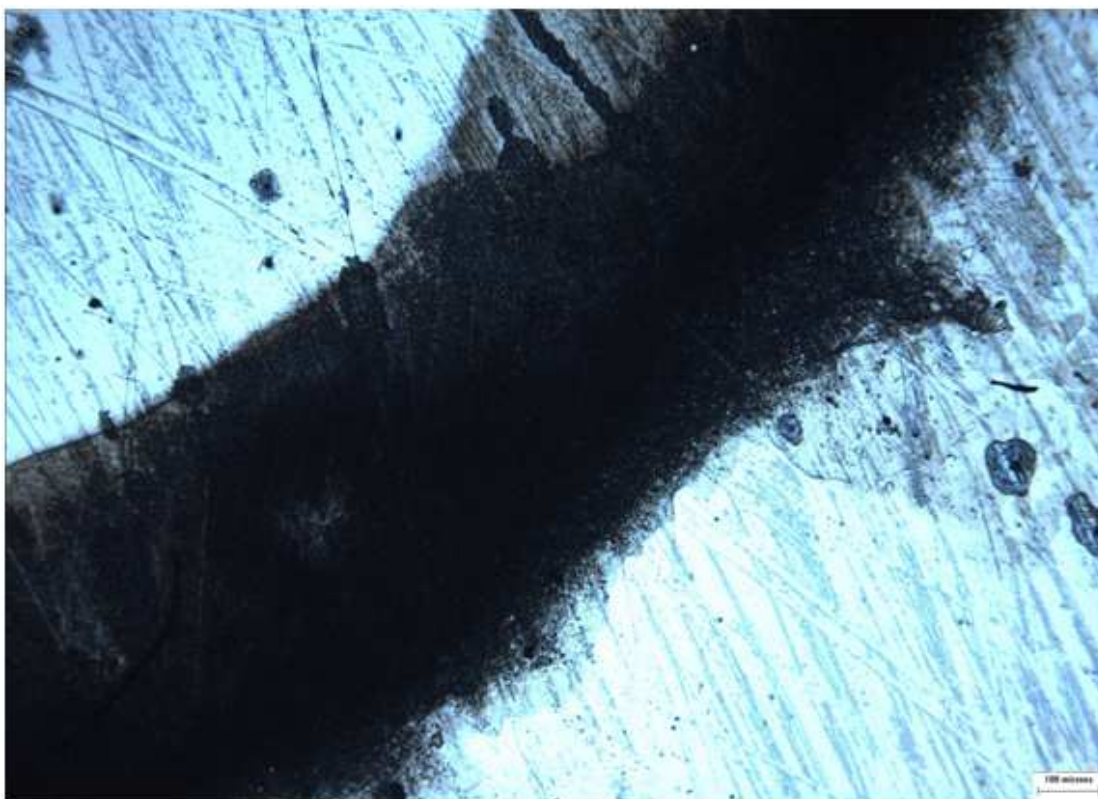
Figure 55 - Optical photograph of surface after PD/CV scans in basic salt solution, S-135. General corrosion and pitting are present.

Pit growth experiments were performed at 3 min and 30 min on 2 different samples for each alloy and pit depth was investigated by optical profilometry. It was found that the samples had too much general corrosion after 3 min (Figure 56) for this method to be a viable pit growth method. After 30 min the samples were completely covered in general corrosion approximately 30 microns in depth uniformly.
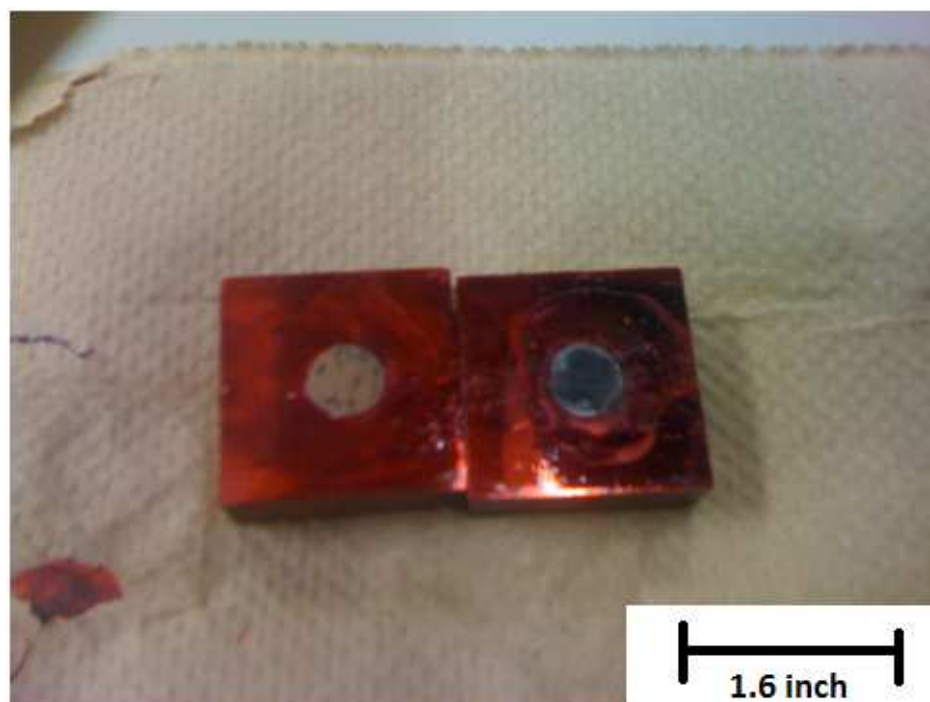
Figure 56 - Left: sample after 3 min of propagation in basic salt solution. Right: sample after 30 min of propagation in basic salt solution. Each sample's edge is 1.6 inches.

Due to the aggressive nature of this "basic salt" environment it was decided that pitting damage investigations were best left to a solution of 6.71 M $CaCl_2$.

6.7 Pit Growth Results

A pitting potential was chosen correlating to a current density of 10^{-3} A/cm^2 for reasons stated in section 5.3.3 Pit Growth Experimental Procedures:. A propagation potential was chosen correlating to a current density of 10^{-4} A/cm^2. For UD-165 the pitting potential was -0.42V vs SCE and the propagation potential was -0.6V vs SCE. For S-135 the pitting potential was -0.44V vs SCE and the propagation potential was -0.6V vs SCE.

A solution of 6.7 M $CaCl_2$ was chosen at room temperature in open air environment for pitting experiments, since the experimental setup was the simplest for this case. A protective film was not experimentally observed by deareation or heating thus; no advantage existed with more complicated experimental setups.

Below in Figure 57-Figure 58 are the results of the PS pit tracking procedure in room temp aerated 6.71 M CaCl$_2$.
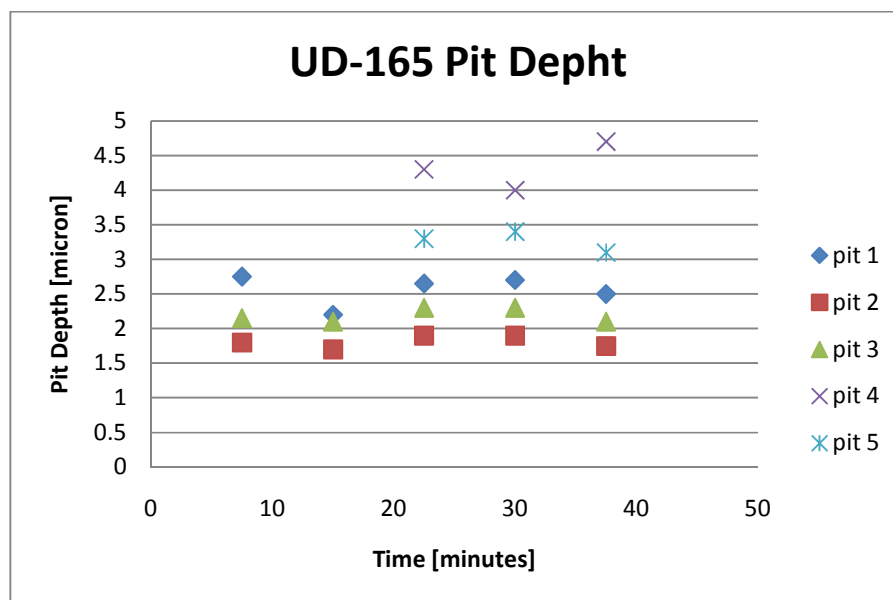
Figure 57 - tracking of individual pits on UD-165 using Potentiostatic pit tracking procedure. E$_{pit}$ = -0.42 V vs. SCE for 30 sec. E$_{prop}$ = -0.6 V vs. SCE for 7.5 min intervals.
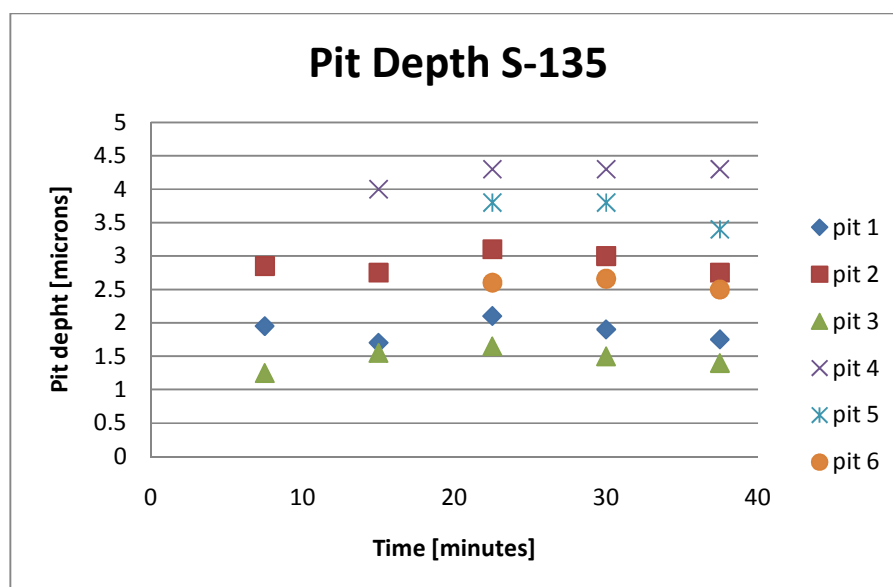
Figure 58 - Tracking of individual pits on S-135 using Potentiostatic pit tracking procedure. E$_{pit}$ = -0.44 V vs. SCE for 30 sec. E$_{prop}$ = -0.6 V vs. SCE for 7.5 min intervals.

Upon examination of Figure 57-Figure 58, pit growth with respect to anodic polarization time was not observed. Pits were measured by optical profilometry, which produces a cross section such as in Figure 59.
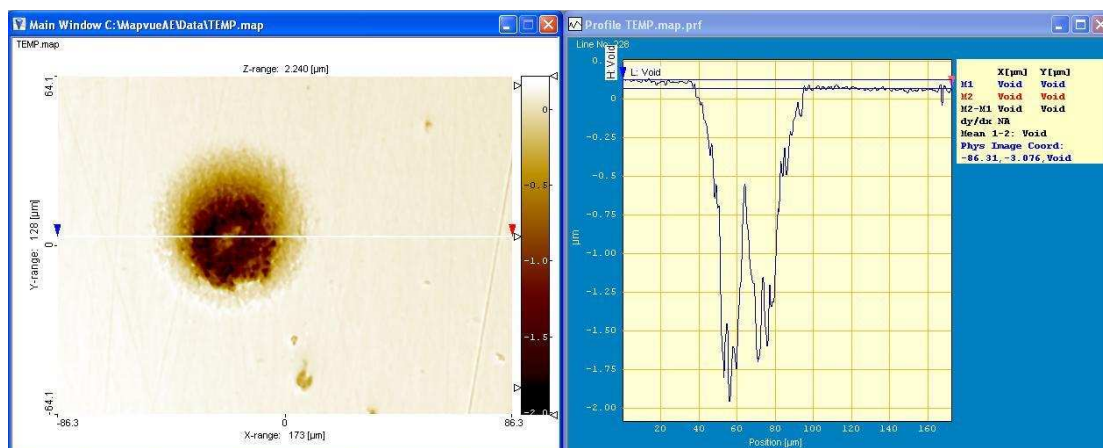
Figure 59 - Resulting cross section found from optical profilometery. Pit on UD-165 after 7.5 min of propagation.

Pit growth was also investigated in 0.7 M $CaCl_2$ at 20°C open-air and in 6.71 M $CaCl_2$ at 95°C deaerated solution. According to Jones (7) magnetite, a protective passive surface film, is stable on carbon steels when the solution is void of oxygen. To void the electrolyte of oxygen, the electrolyte was purged with argon and raised to 95°C. Samples were pitted then propagated for 3 and 30 min and then pit depth was measured via optical profilometery. No growth was observed in 95°C 6.71 M $CaCl_2$ deaerated solution.

6.8 Pit Density Measurements

Optical profilometry was performed on pitted fatigue samples. Below in Figure 60 are the results of the measurements. Figure 61 and Figure 62 show example cross sections of S-135 and UD-165 respectively as found via optical profilometry.
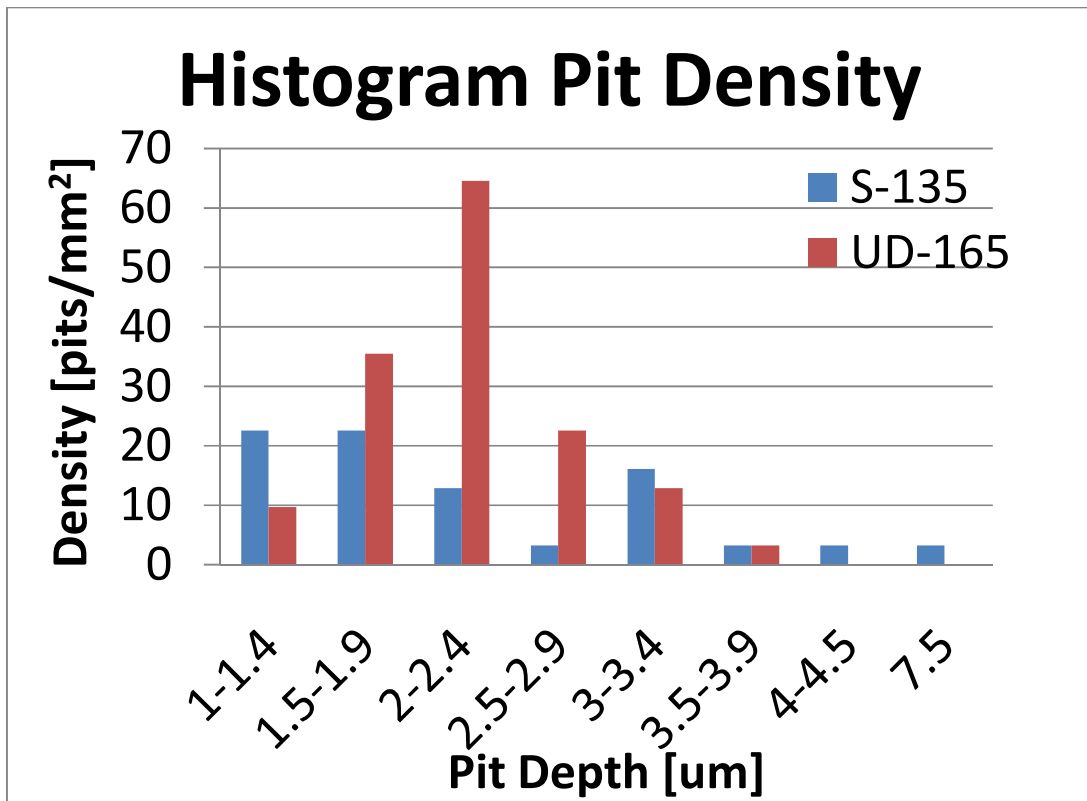
Figure 60 - Histogram of pit density on fatigue specimens. Measurements made on fatigues samples pitted at 0.001 A/cm^2 for 5 min in open air at 20°C 6.7 M CaCl$_2$ solution.
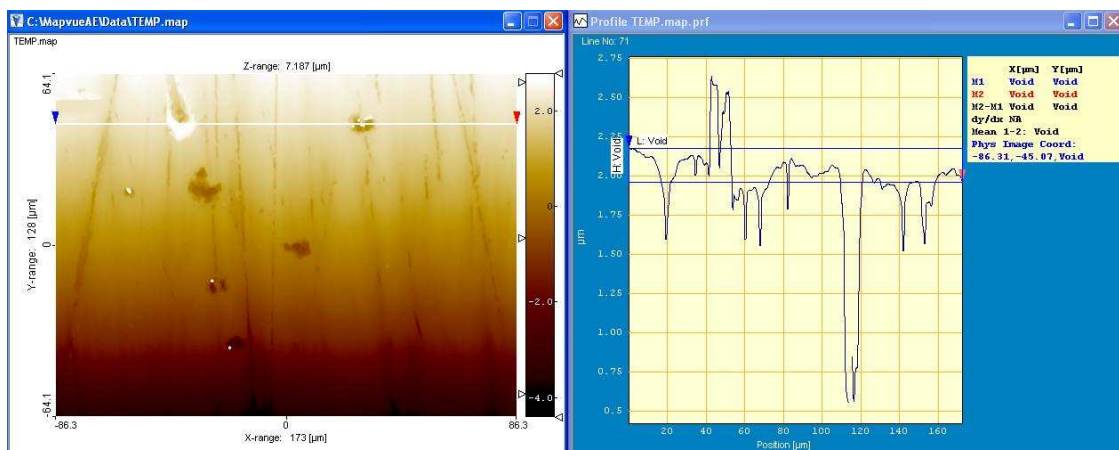
Figure 61 - example optical profile of S-135. Pitted for 5 min at 0.001 A/cm^2 in open air at 20°C CaCl$_2$ solution. Area = 0.022 mm^2.
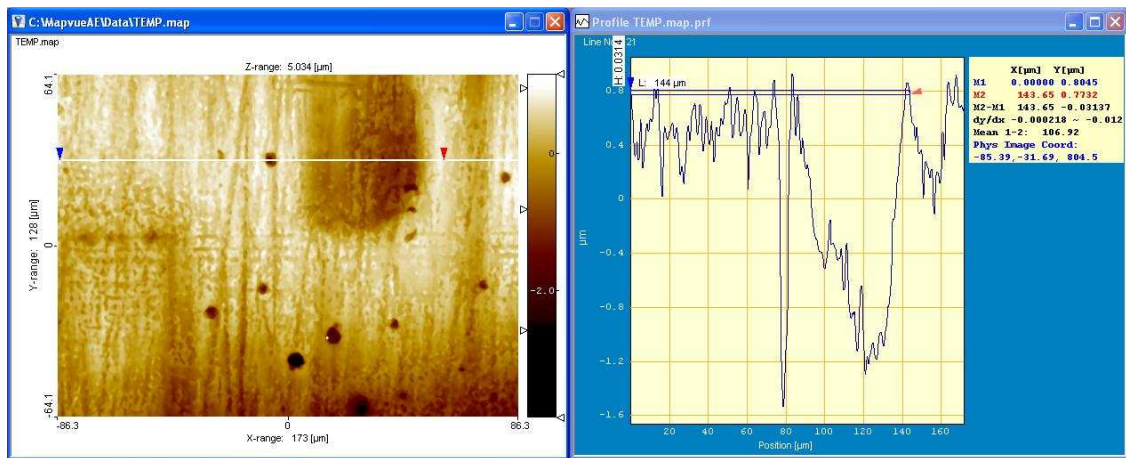
Figure 62 - Example optical profile of UD-165. Pitted for 5 min at 0.001 A/cm^2 in open air at 20°C CaCl$_2$ solution. Area = 0.022 mm^2.

Twenty areas were taken at random for each alloy with example results shown in Figure 61 and Figure 62 for S-135 and UD-165 respectively. Ignoring depth of pits, the average pit density for each alloy is as follows:

S-135: 89 pits/mm^2

UD-165: 155 pits/mm^2

It was observed that UD-165 had a large density of pits about 2-2.5 μm deep and about 5-30 μm in diameter. S-135 was observed to have wider pits measuring 5-50 μm in diameter, while a large density at a particular depth was not observed.

6.9 Fatigue Results

It was decided that lifetime fatigue tests were to be performed on:

1) virgin samples
2) pitted samples
3) pitted samples left in 20°C, 30-40% humidity for 2 weeks before testing

Baseline data for virgin S-135 and UD-165 was gathered and is shown below in Figure 63. Experiments were performed according to the section 5.4 Fatigue Lifetime Procedure:, Figure 63 - Figure 66 show the fatigue lifetime data gathered for S-135 and UD-165.
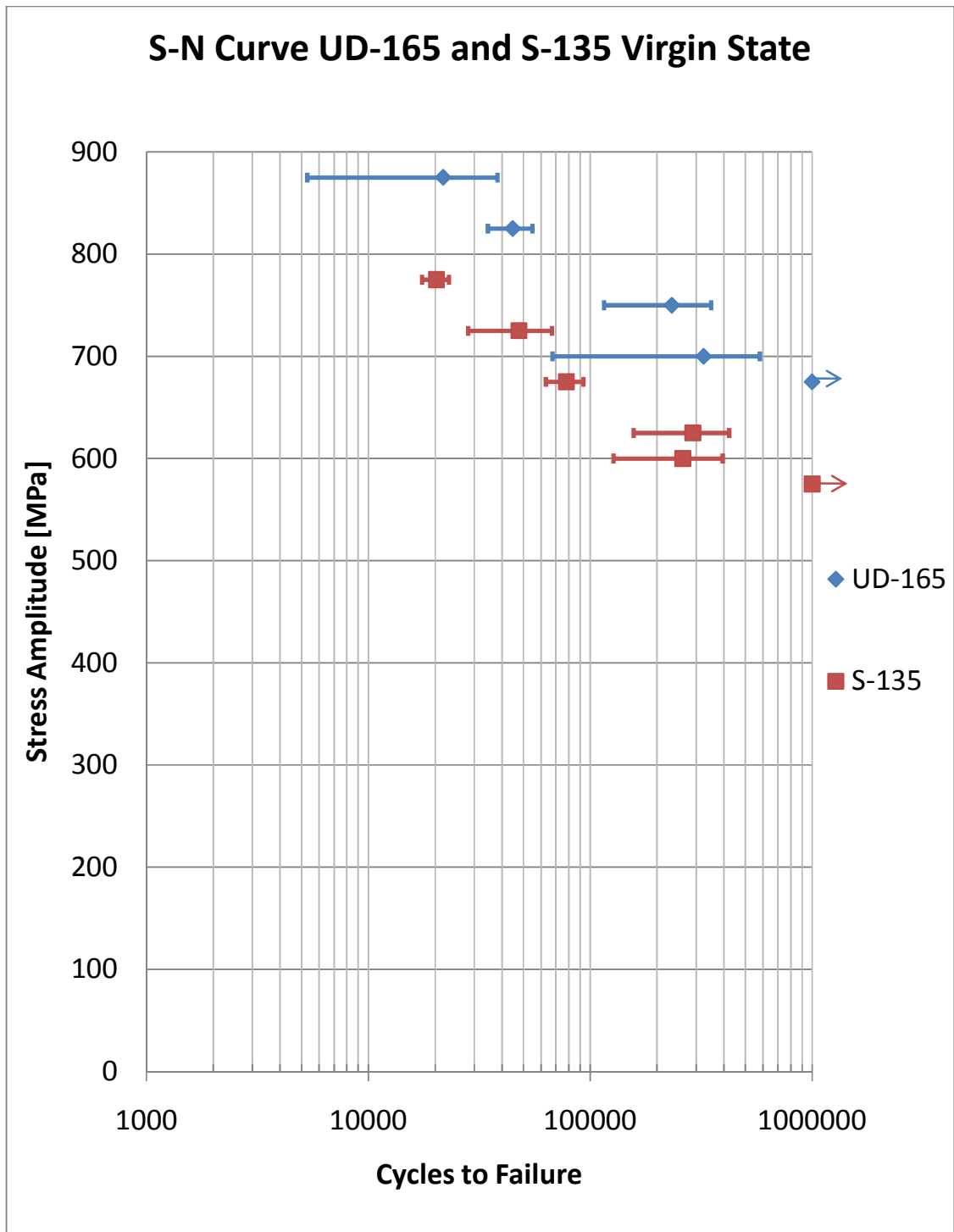
Figure 63 - The fatigue limit was set to 10^6 cycles. Experiments were done at 23^oC at 30-40% humidity. Arrows indicate samples which did not fail.
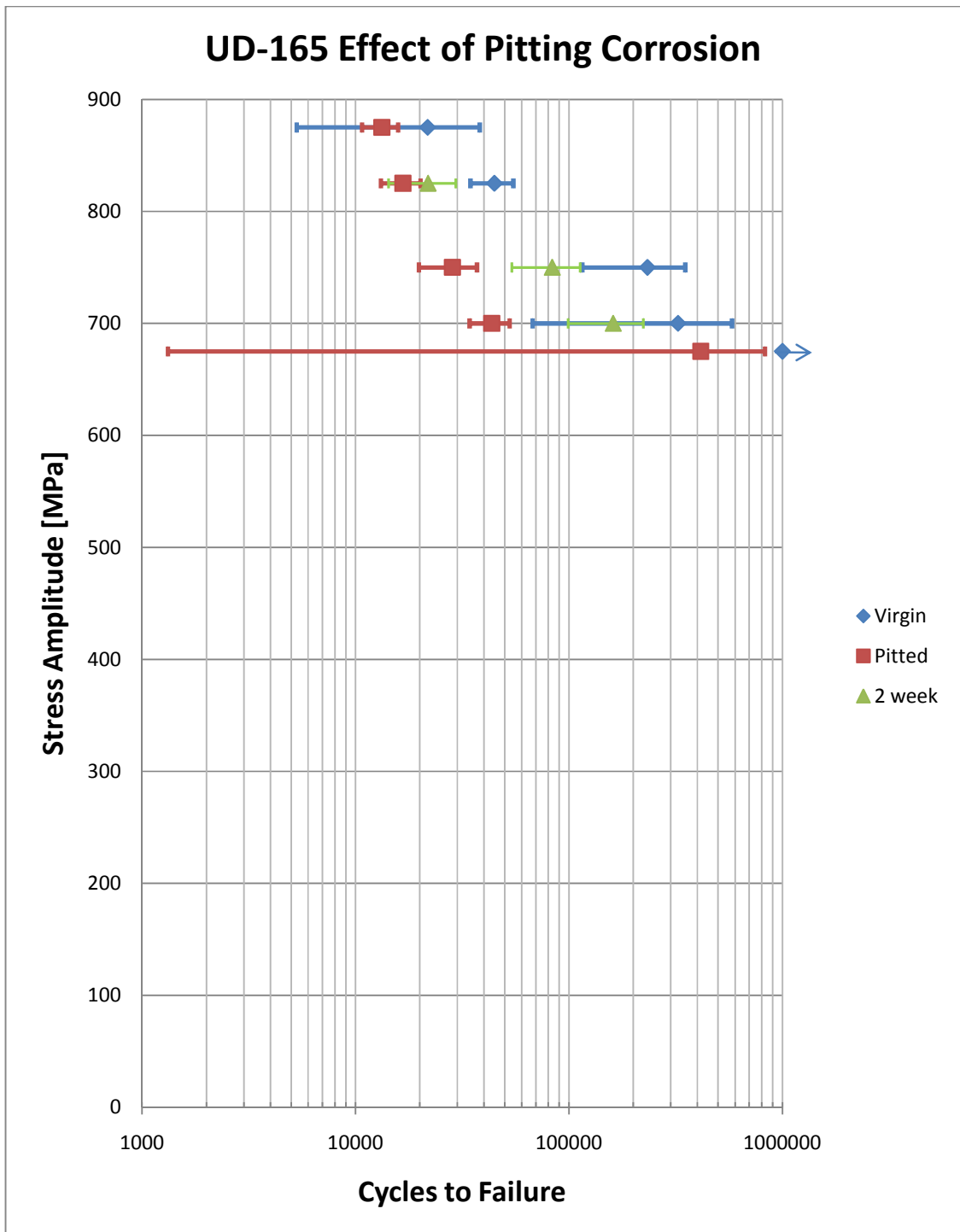
Figure 64 - Effect of pitting damage on UD-165. The fatigue limit was set to 10^6 cycles. Experiments were done at 23°C at 30-40% humidity Arrows indicate samples which did not fail.
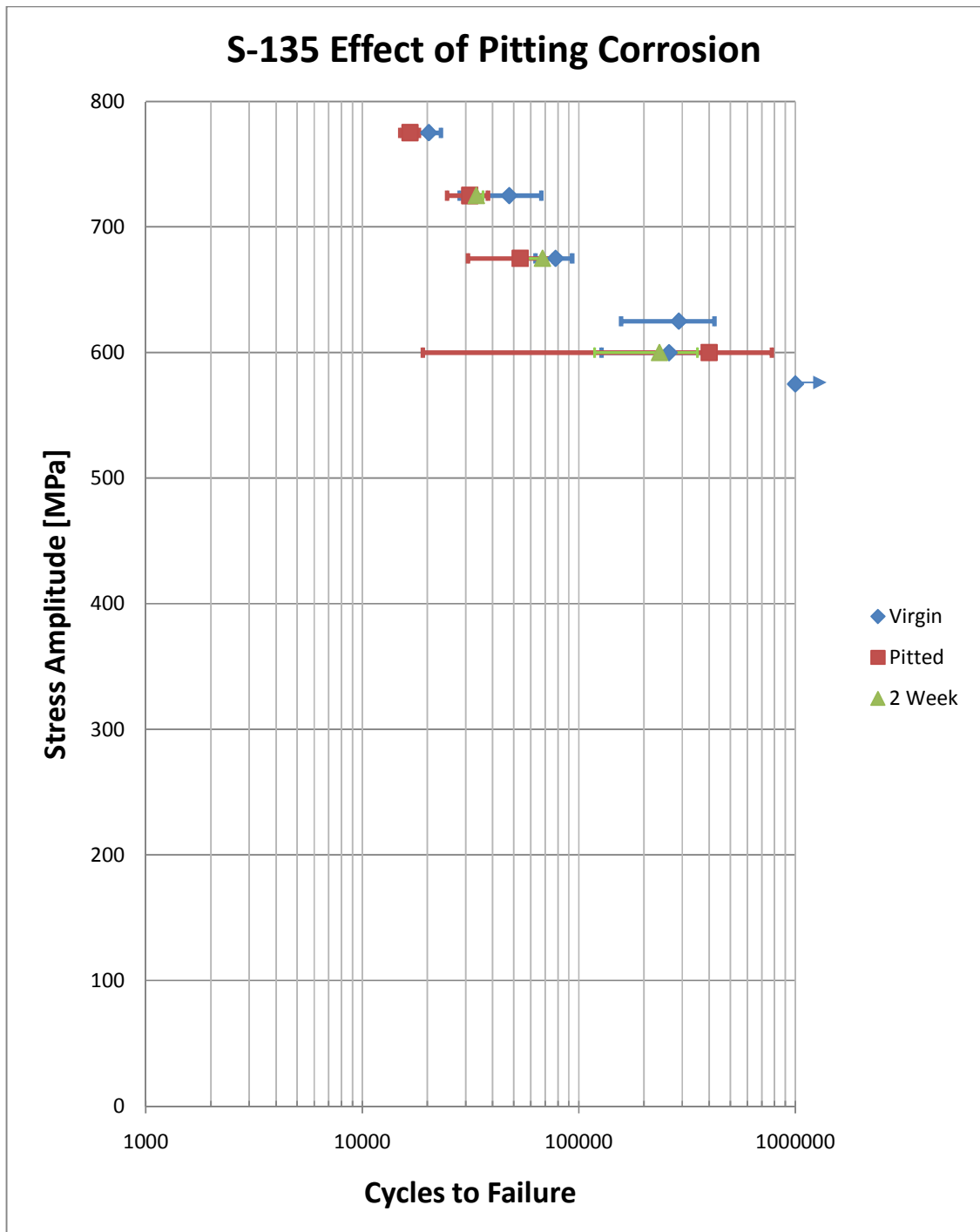
Figure 65 - Effect of pitting damage on S-135. The fatigue limit was set to 10^6 cycles. Experiments were done at 23$^{\text{o}}$C at 30-40% humidity. Arrows indicate samples which did not fail.
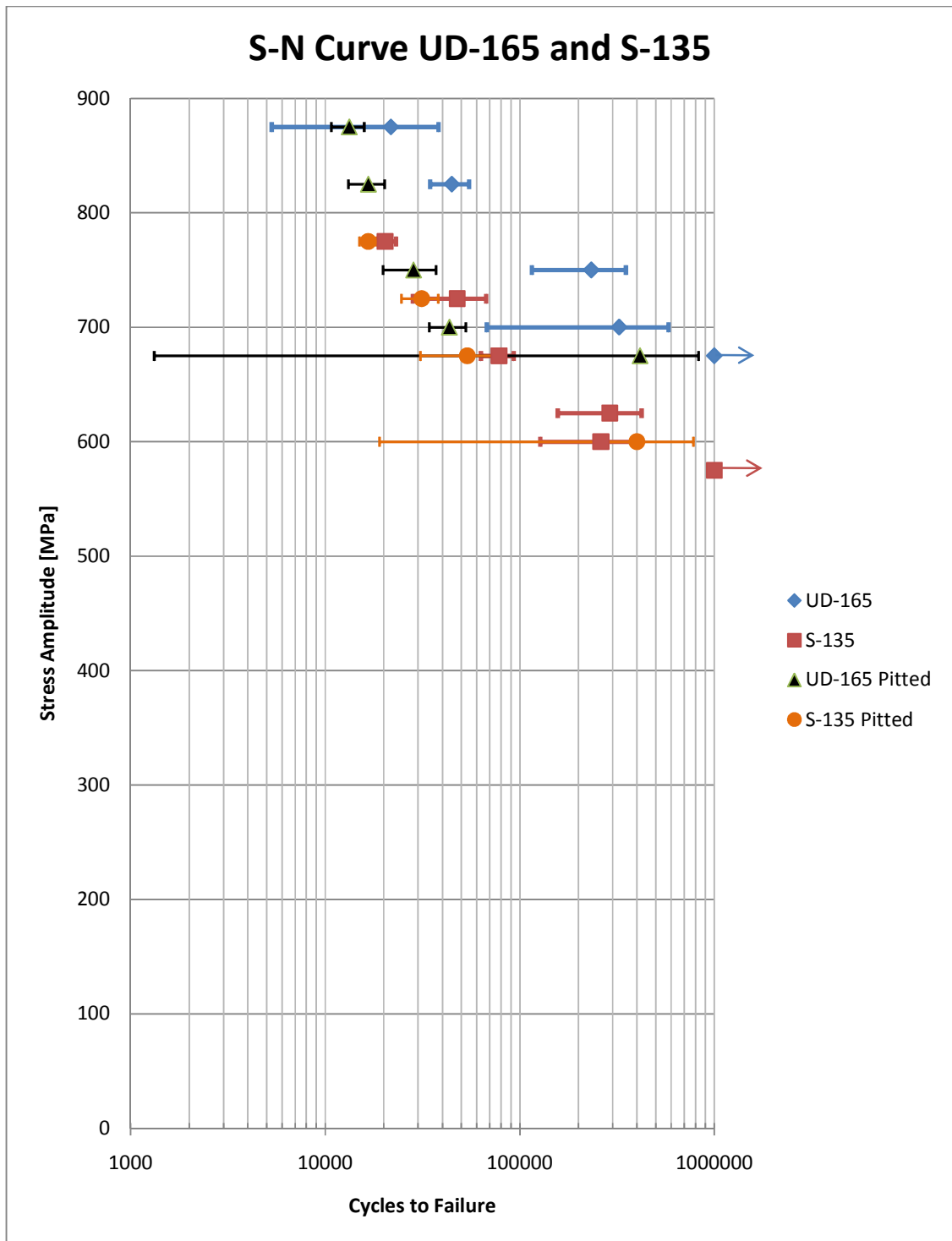
Figure 66 - The fatigue limit was set to 10^6 cycles. Experiments were done at 23°C at 30-40% humidity. Arrows indicate samples which did not fail.

From Figure 63 - Figure 66, it is apparent that pitting by anodic polarization caused a decrease in fatigue life for UD-165. Statistical testing revealed no statistically significant effect on S-135, more details will be presented in section 7.6 Fatigue Results Discussion.

6.10 Fractography

Images of the fracture surfaces were taken in a Scanning Electron Microscope (SEM) in attempt to explain the observed changes in fatigue life due to corrosion damages.

6.10.1 UD-165 Fracture Images

The following Figure 67 - Figure 73 show the fracture surfaces of UD-165 found for the lifetime fatigue samples.
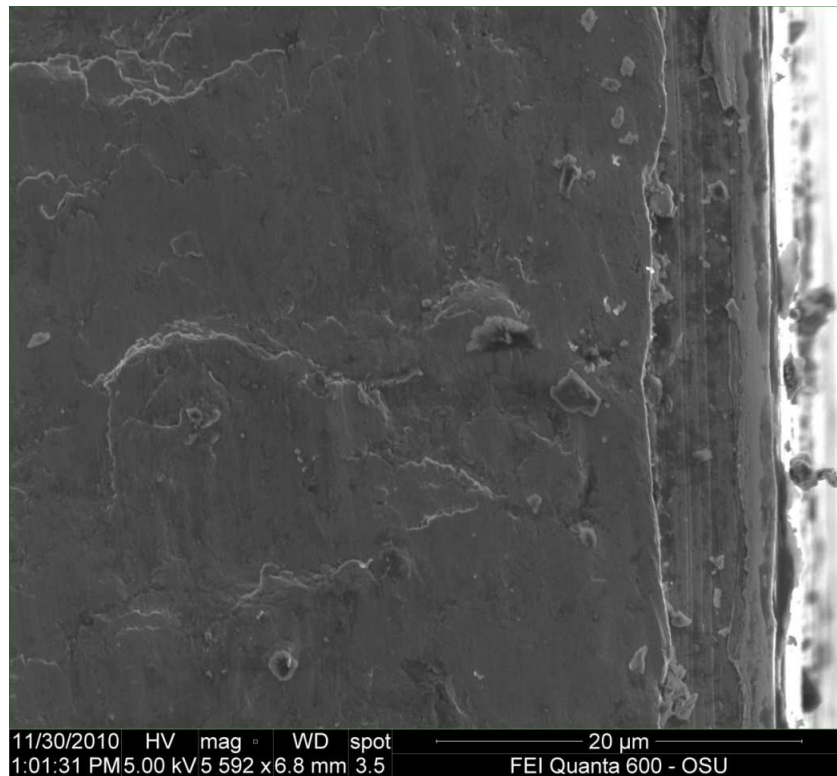
Figure 67 - Fracture surface of UD-165 virgin sample with stress amplitude of 700 MPa and failure at 189004 cycles (average failure at 324277 cycles for 700 MPa).

The sample featured in Figure 67 likely failed due to tooling mark ~8 μm deep. The Tooling mark covered 1/3-1/4 of the circumference.
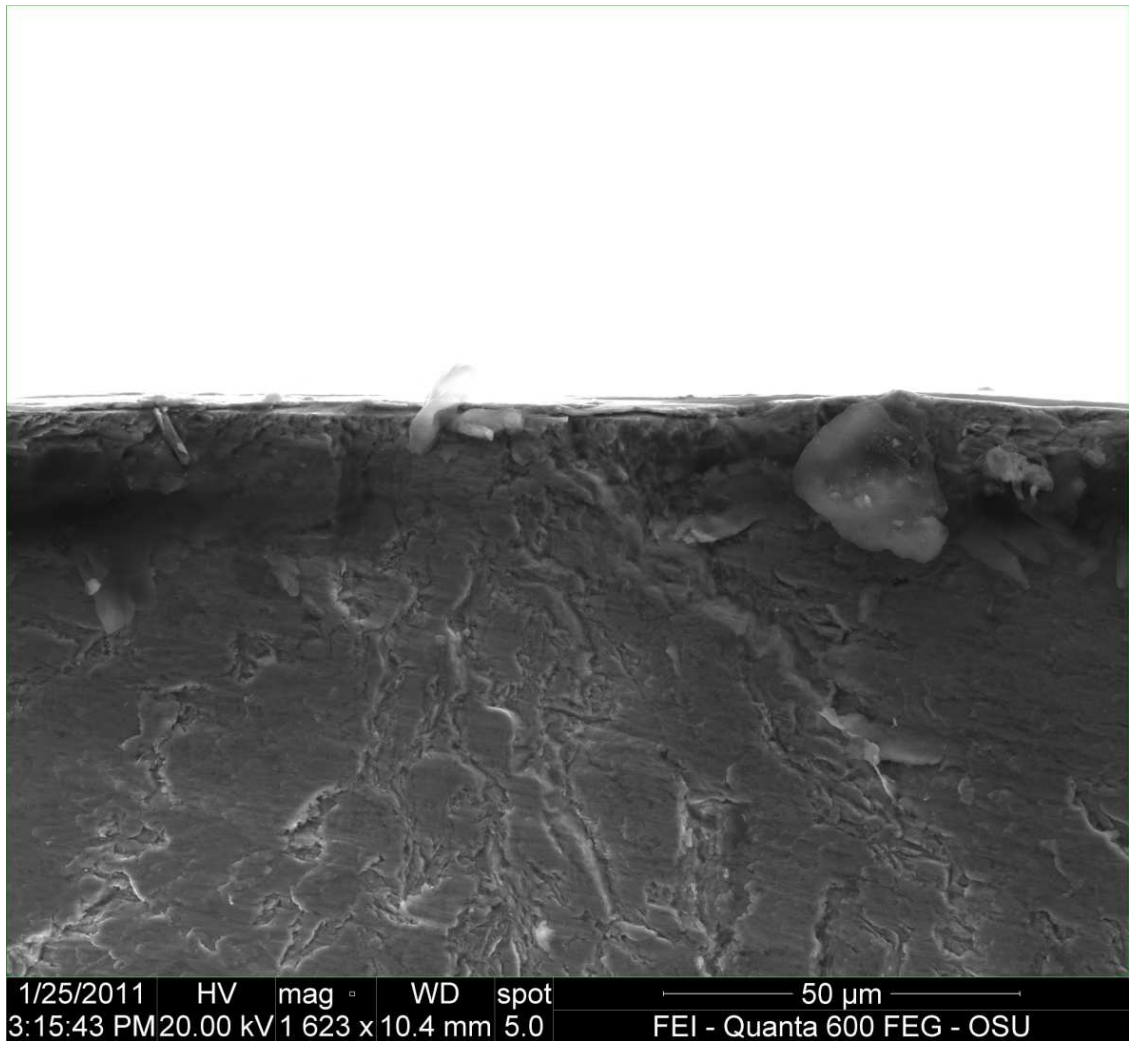
Figure 68 - Fracture surface of UD-165 virgin sample with stress amplitude of 750 MPa and failure at 357175 (average failure at 233137 for 750 MPa).

The sample featured in Figure 68 likely failed due to tooling mark.
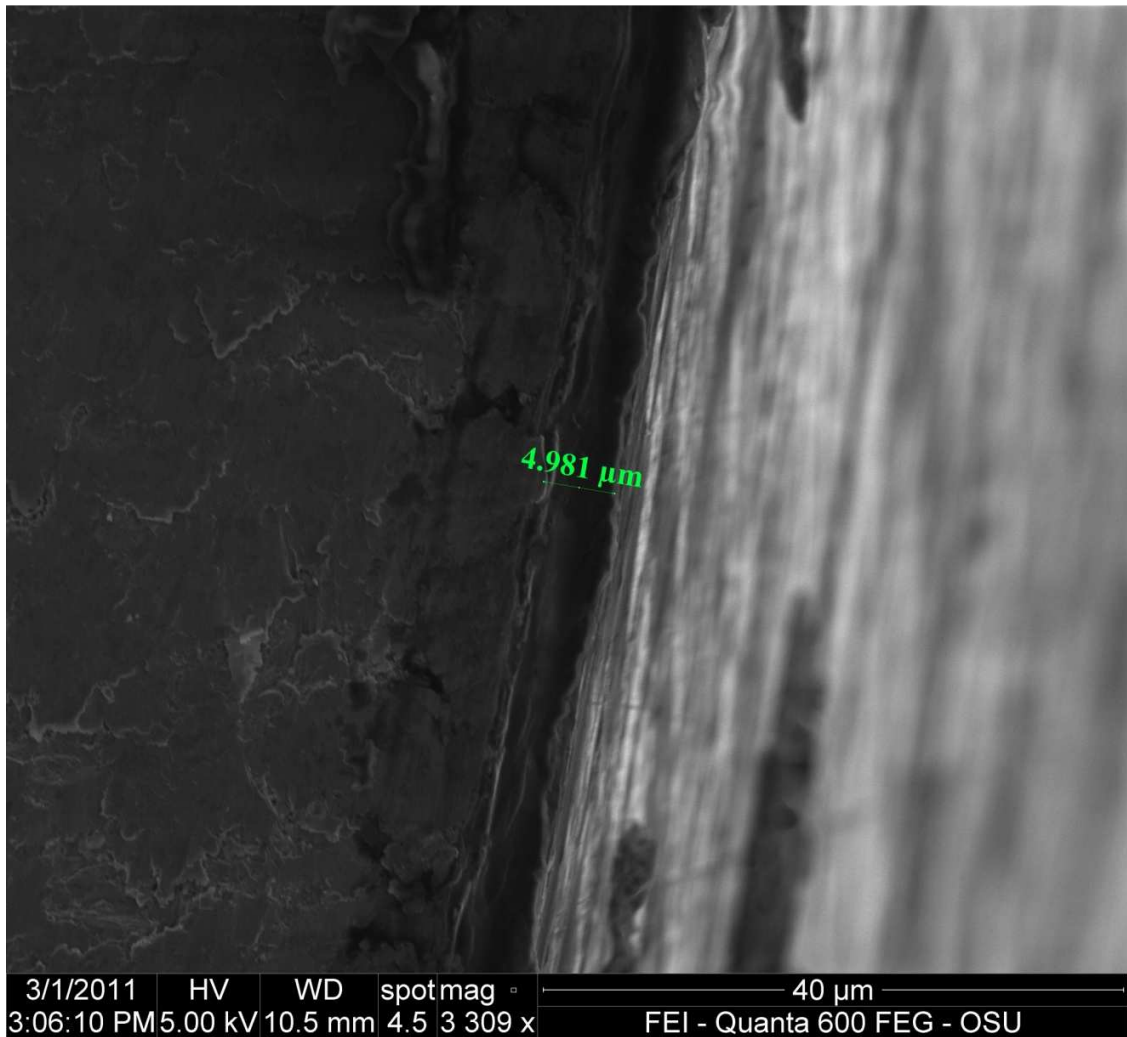
Figure 69 - Fracture surface of UD-165 virgin sample with stress amplitude of 825 MPa and failure at 32977 cycles (average failure at 44724 cycles for 825 MPa).

The sample featured in Figure 69 shows tooling mark approximately 5 μm deep.

11/29/2010 | HV | mag ◻ | WD | spot | ──────── 10 µm ────────
4:03:43 PM | 5.00 kV | 10 162 x | 9.2 mm | 5.0 | FEI Quanta 600 - OSU
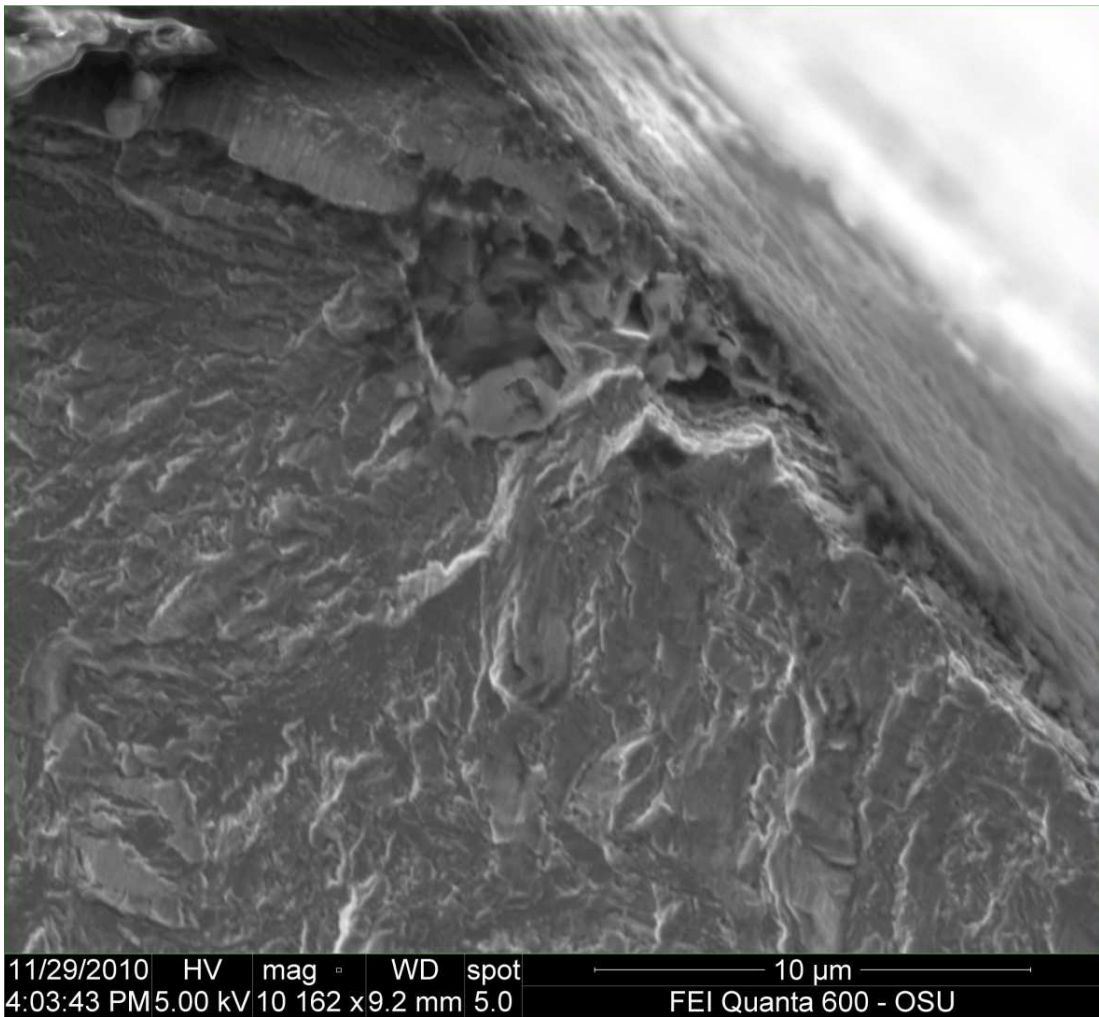
Figure 70 - SEM image of small pit ~ 3 µm wide and ~3 µm deep on UD-165 after pitting corrosion. Sample fatigued at 700 MPa and failed at 50849 cycles (average failure at 43500 cycles for 700 MPa).

The sample featured in Figure 72 shows a small corrosion pit. Energy Dispersion Spectroscopy (EDS) detected presence of oxygen around the pit indicating a corrosion reaction has occurred.
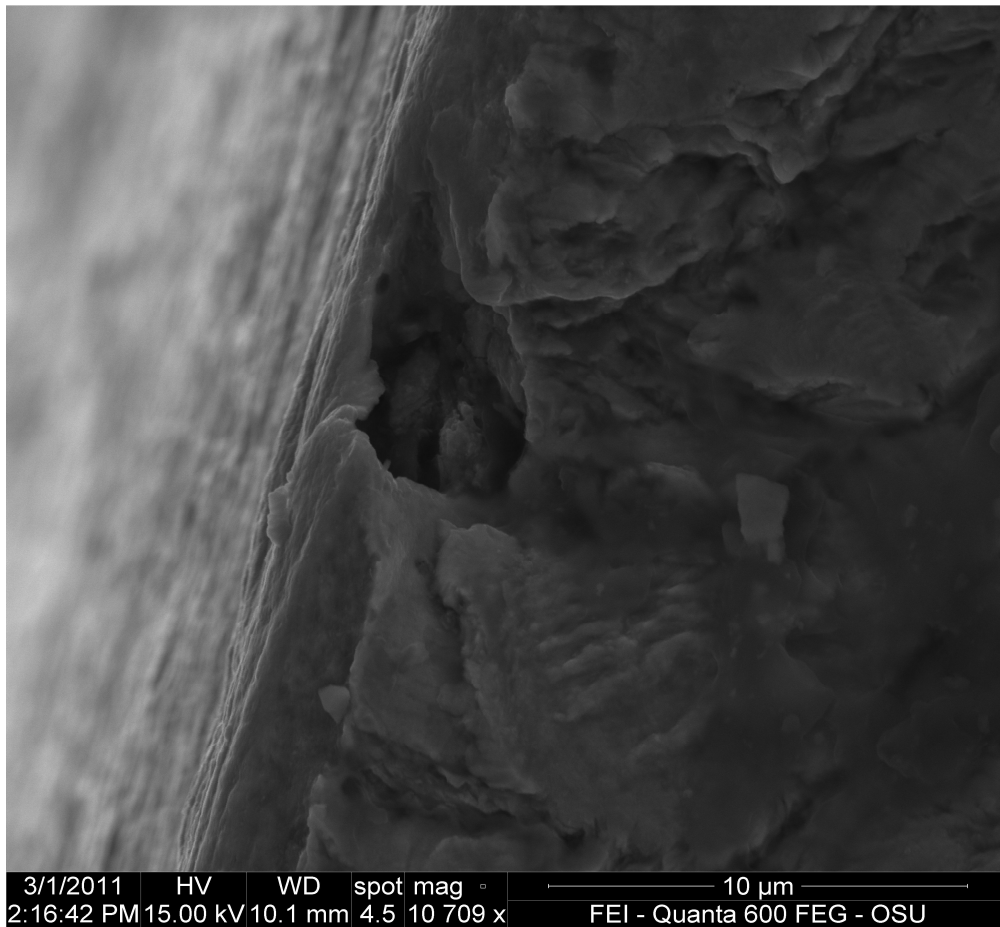
Figure 71 - SEM image of fractured surface on UD-165 after pitting corrosion at 750 MPa. Sample failed at 22804 cycles with the average at 28500 cycles.

The sample featured in Figure 71 had a corrosion pit which likely influenced fatigue life. Pit appears to be undercut, or have a horizontal displacement from the pit mouth which would make measurement of pit depth by the optical profilometry method difficult.

12/10/2010 | HV | WD | spot | mag □ | tilt | ⟵——— 20 μm ———⟶
2:56:42 PM | 30.00 kV | 9.0 mm | 4.5 | 3 903 x | 0 ° | FEI - Quanta 600 FEG - OSU
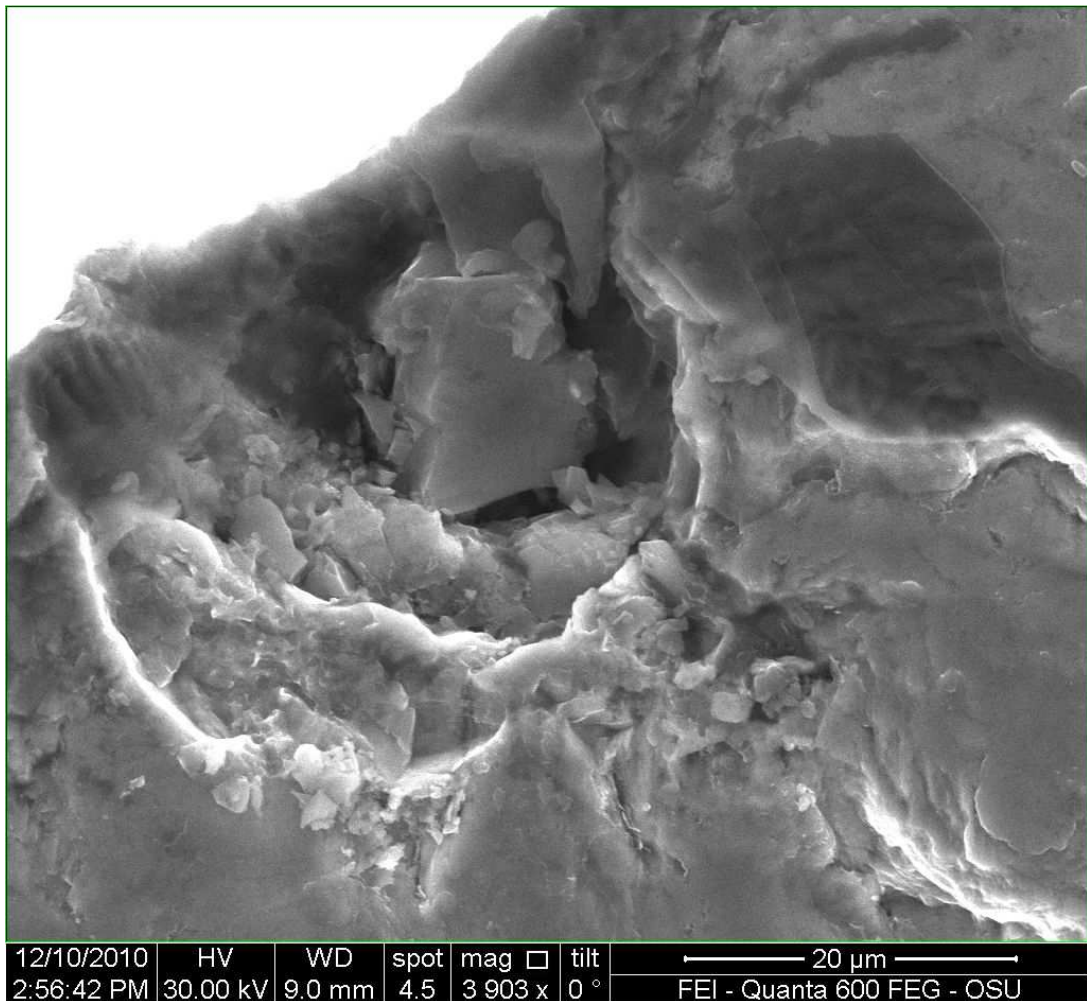
Figure 72 - Fracture surface of UD-165 pitted sample after two week ambient exposure with stress amplitude of 750 MPa and failure at 61093 cycles (average failure at 83470 cycles for 750 MPa).

The sample featured in Figure 72 shows a corrosion pit ~ 25 μm deep. EDS detected presence of oxygen around pit indicating a corrosion reaction has occurred.
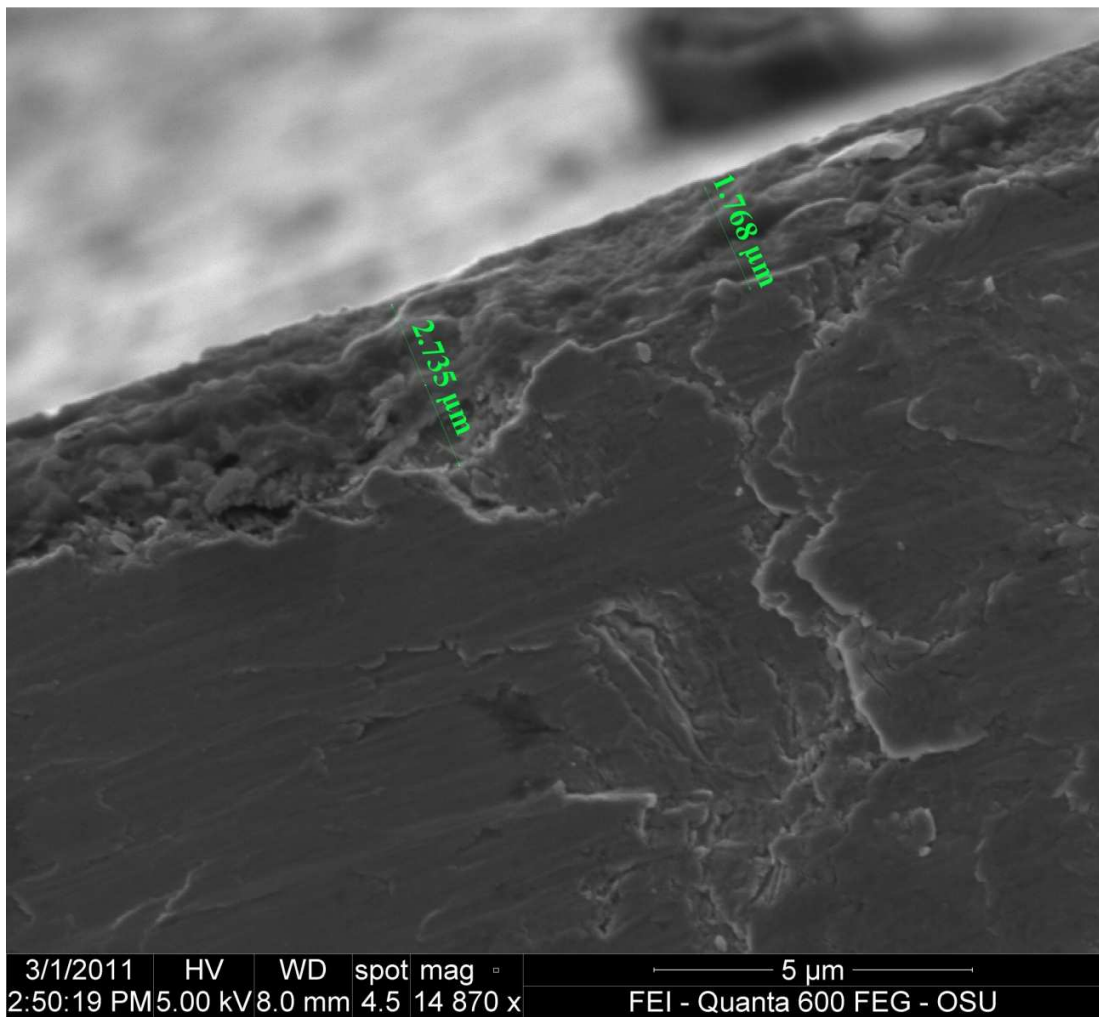
Figure 73 - Fracture surface of UD-165 pitted sample with stress amplitude of 825 MPa and failure at 20631 cycles (average failure at 16672 cycles for 825 MPa).

The sample featured in Figure 73 shows presence of a tooling mark ~2 μm deep. Anodic polarization appears to have increased the depth of the tooling mark.

6.10.2 S-135 Fracture Surfaces

The following Figure 74 -Figure 77 show the fracture surfaces of S-135 found for the lifetime fatigue samples.
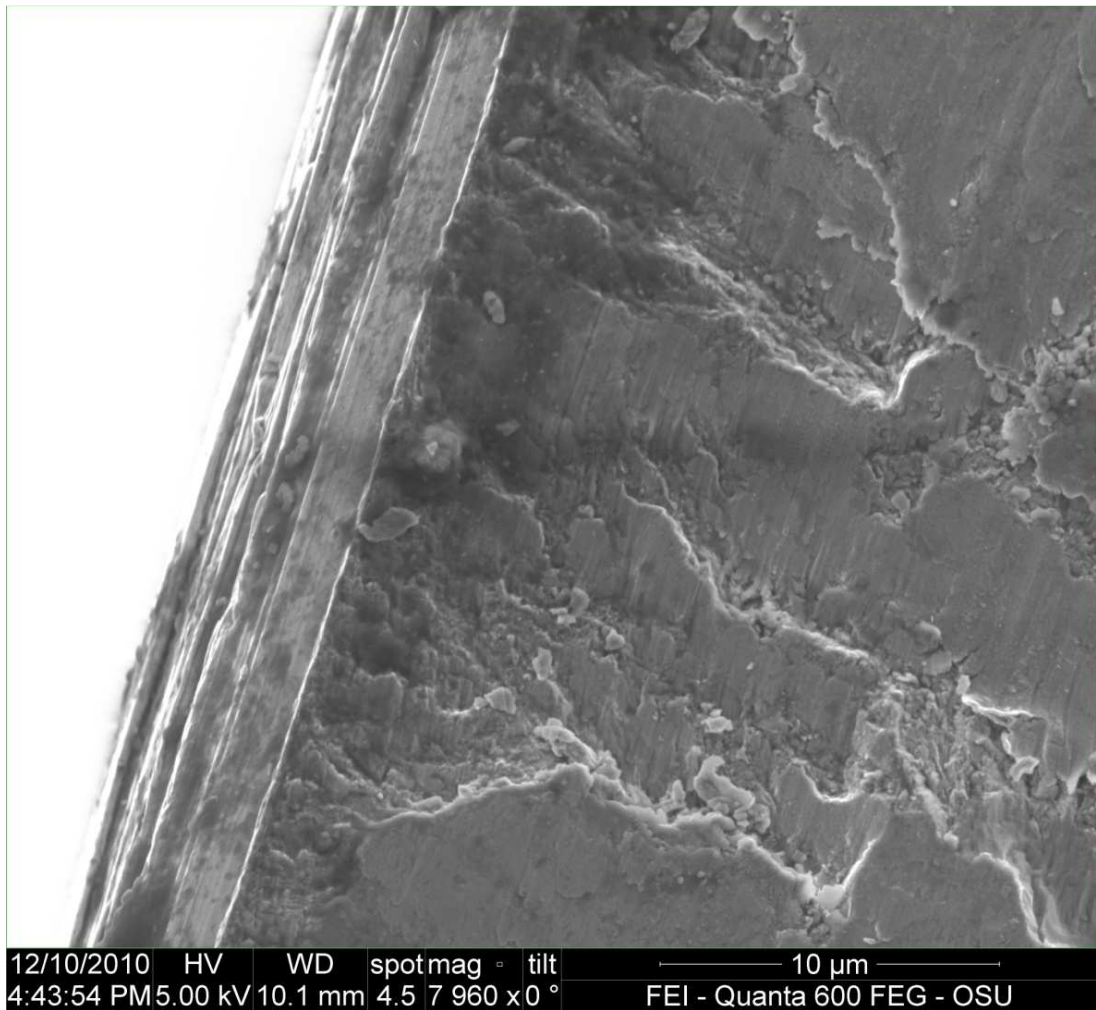
Figure 74 - Fracture surface of S-135 virgin sample with stress amplitude of 625 MPa and failure at 428347 cycles (average failure at 289688 cycles for 625 MPa).

The sample featured in Figure 74 failed due to a tooling mark ~6μm deep.
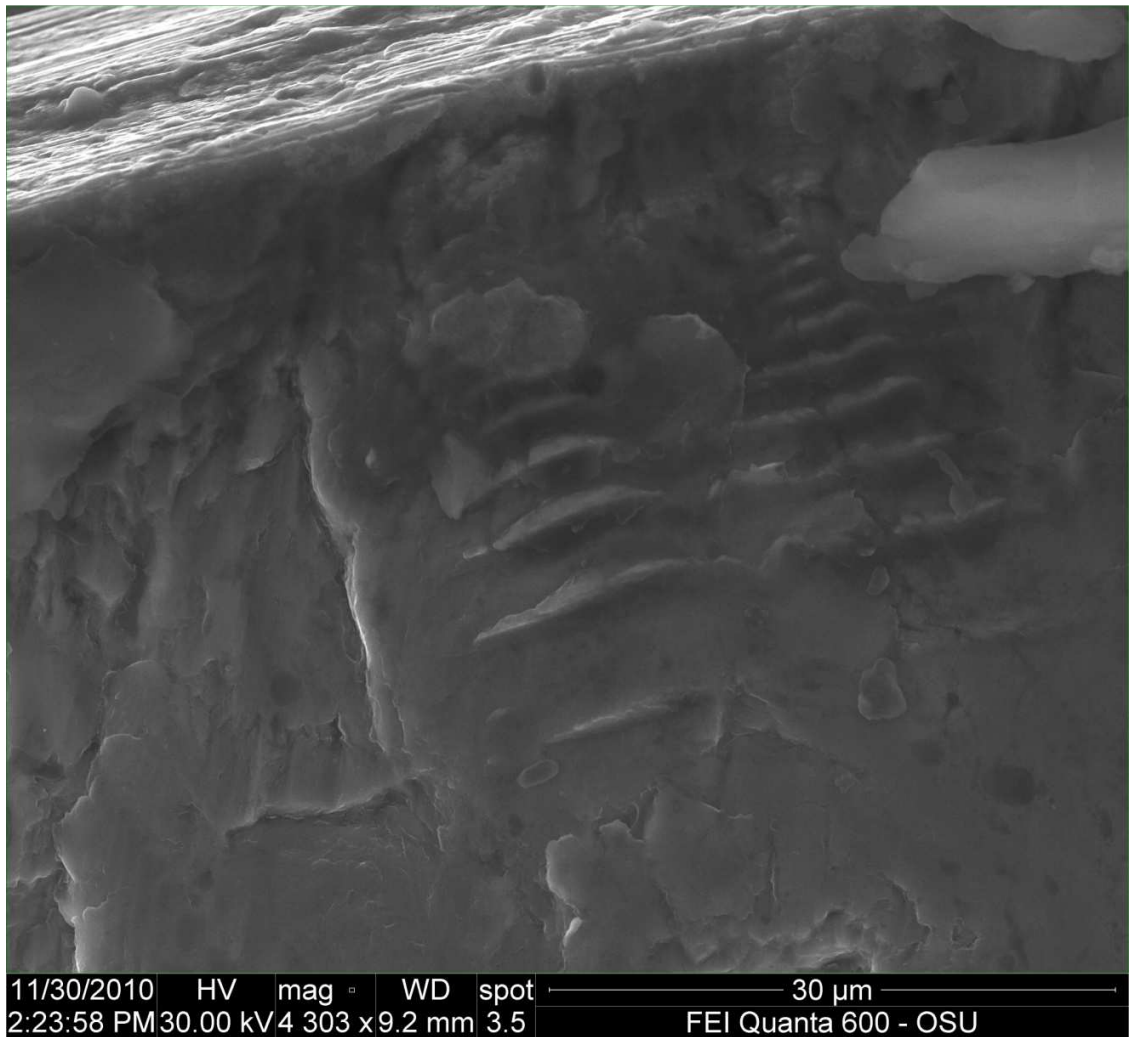
Figure 75 - Fracture surface of S-135 virgin sample with stress amplitude of 725 MPa and failure at 29106 cycles (average failure at 47662 cycles for 625 MPa).

Failure initiation for Figure 75 is undetermined.

11/22/2010 | HV | mag ⊞ | WD | ⊢————— 50 μm —————⊣
1:43:37 PM | 20.00 kV | 1 257 x | 11.7 mm | FEI Quanta 600 - OSU
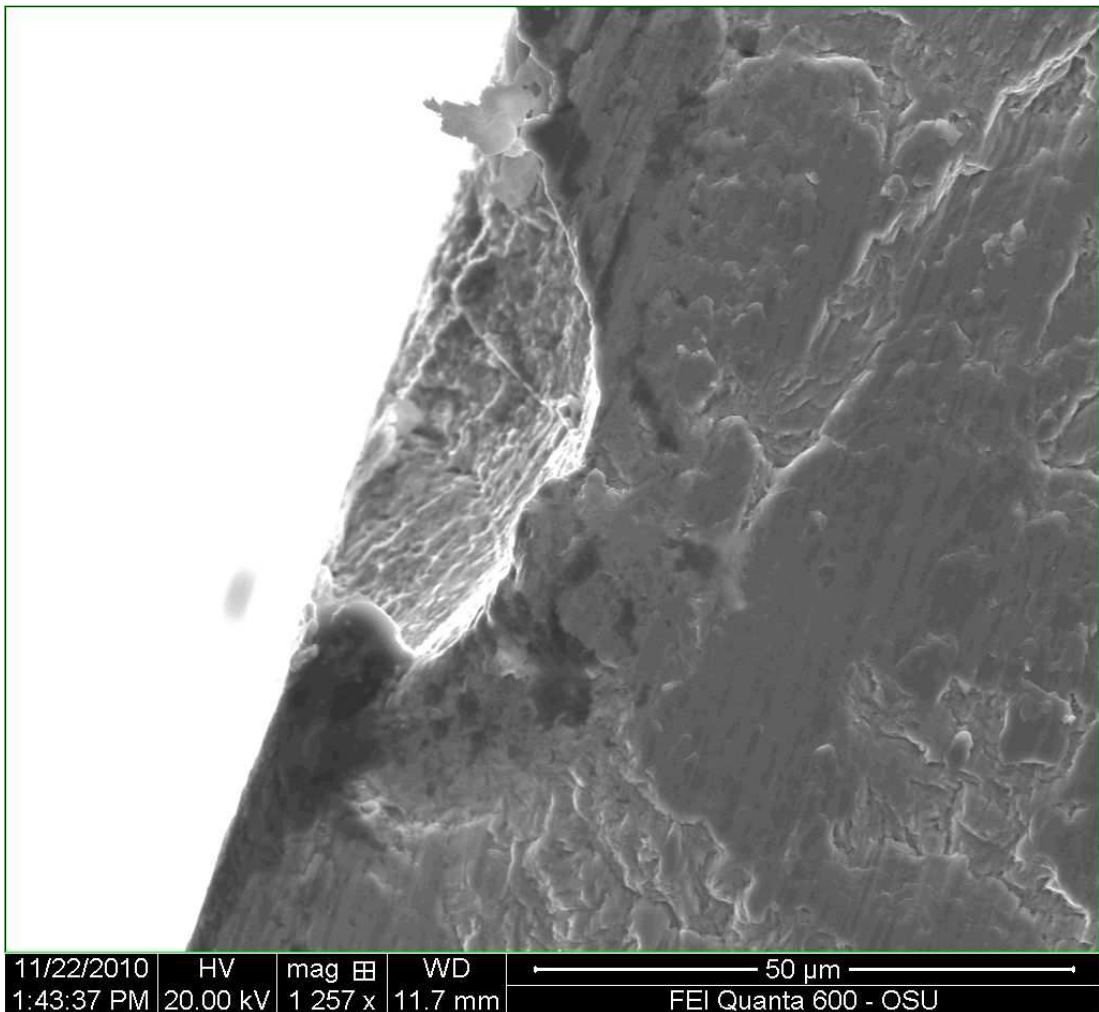
Figure 76 - Fracture surface of S-135 pitted sample with stress amplitude of 600 MPa and failure at 172787 cycles (average failure at 399291 cycles for 600 MPa).

The sample featured in Figure 76 shows a corrosion pit ~40 μm wide and ~20 μm deep. EDS showed presence of oxygen around pit indicating corrosion processes. Corrosion pits like this were rare and did not influence the average fatigue life as it was the only corrosion pit of three samples measured for the stress amplitude.
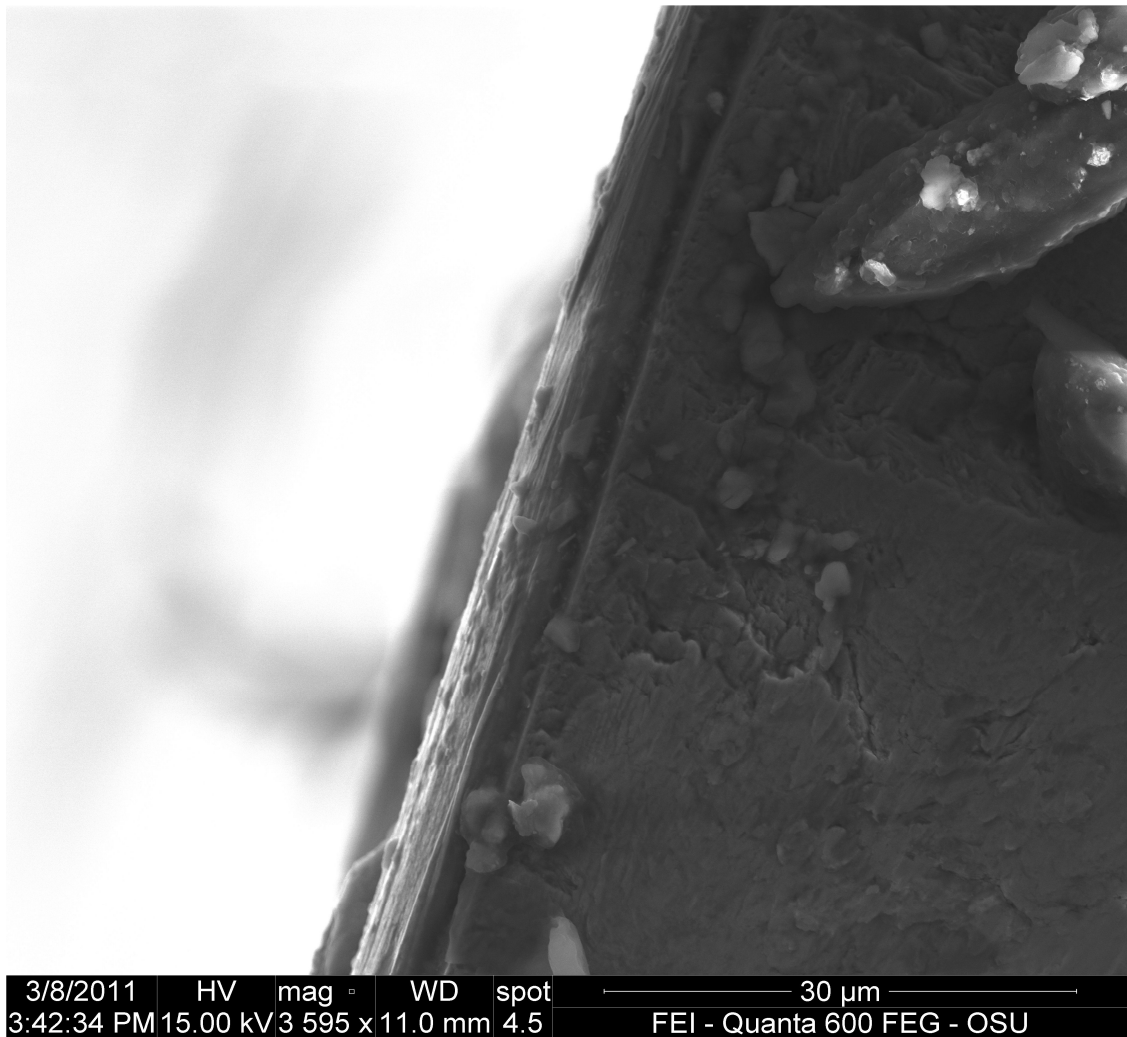
Figure 77 - Fracture surface of S-135 pitted sample with stress amplitude of 725 MPa and failure at 25819 cycles (average failure at 31325 cycles for 725 MPa).

The sample featured in Figure 77 failed at a tooling mark.

7 Experimental Results Discussion

In this section the experimental results are discussed and analyzed. There were two phases to this project. The first phase involved gathering corrosion data. The second stage involved gathering fatigue data.

7.1 Material Defect Discussion

Inclusions are the initiation sites for pitting corrosion. Figure 60 shows that UD-165 is more susceptible to pitting corrosion than S-135. The increase in susceptibility to pitting corrosion in UD-165 is likely to be explained through analysis of inclusions.

A non-exhaustive study on surface defects was performed. For S-135 inclusions tended to have high amounts of Mn and S found by EDS. It is very likely that MnS inclusions form in S-135 due to the high amount of Mn (30-40%(at)) and S (30-40%(at)) found. However for UD-165 only traces of Mn and S are found. UD-165 showed inclusions rich in Nb and C or rich in Fe, Al and O with traces of Mn and S. Presence of Al and O in inclusions indicate polishing media removed inclusions and contaminated the left void on UD-165. Traces of Mn and S indicate that a MnS inclusion may have been present but was removed by the polishing process. It is expected that further investigations would reveal inclusions rich in Mn and S for UD-165.

Many different sulfide compounds influence pitting, however MnS and FeS are the most active. Gainer noted that the higher the concentration of FeS in the inclusions, the more active the inclusion (11). Active inclusions lead to pit initiation. FeS is a highly conductive and detrimental inclusion in steel (13). FeS is formed from the solidification process. During solidification the sulfides are in a mixed state (Mn,Fe)S and during cooling the iron diffuses out leaving pure MnS. FeS can be introduced into the matrix by rapid cooling, such as in the martensitic phase transformation or by having a Mn:S ratio of lower than 4:1 (13).

For S-135, the Mn:S ratio is 390:1 and for UD-165 the ratio is 126:1 based on the chemical compositions shown in Table 3, page47. It is very likely that there was enough Mn to absorb S to form MnS rather than FeS. However, due to the rapid cooling of the martensitic phase transformation it is likely that some FeS was formed. If FeS was found abundant in UD-165, it may explain why UD-165 had approximately 1.75 times as many pits per area as S-135 from anodic dissolution.

No electrochemical data was found regarding the activity and influence of Nb and C rich inclusions had on pitting initiation on UD-165.

7.2 Immersion Sample Discussion

As shown in section 6.2 Experimental Results - Immersion Testing the immersion samples showed pitting corrosion. A FeOOH product was formed. FeOOH is a non-protective film which allows for further corrosion to take place. FeOOH can be formed in the following process outlined by Wranglen (10), in chloride containing solutions Equation 27-Equation 31.

$$Fe \rightarrow Fe^{2+} + 2e^-$$
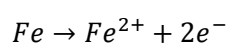
Equation 27 - Anodic dissolution of Iron

$$Fe^{2+} + H_2O \rightarrow FeOH^+ + H^+$$
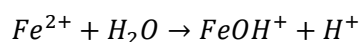
Equation 28 - Hydrolysis of Iron ions

$$2FeOH^+ + \frac{1}{2}O_2 + 2H^+ \rightarrow 2FeOH^{2+} + H_2O$$
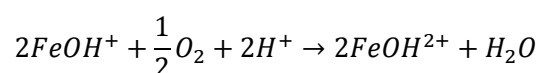
Equation 29 - Oxidation of Iron (II) hydrate

$$2FeOH^{2+} + H_2O \rightarrow Fe(OH)_2^+ + H^+$$
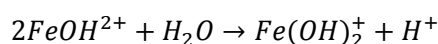
Equation 30 - Hydrolysis of Iron (III) hydrate

$$Fe(OH)_2^+ + OH^- \rightarrow FeOOH + H_2O$$
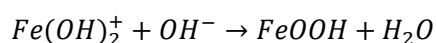
Equation 31 - Precipitation of rust

The solution of 6.7 M $CaCl_2$ had a pH of around 8.6. Looking at the Pourbaix diagram, Figure 8, page 10, iron shows passive behavior with Fe_2O_3 as the stable compound. This means that UD-165 and S-135 will tend to form a non-protective film and are susceptible to pitting corrosion in 6.7 M $CaCl_2$ environments near neutral to slightly basic pH.

7.3 Polarization Curves Analysis

As shown in Figure 41-Figure 50, pages 54-58, anodic dissolution and mechanical passivation was observed though polarization methods. The effect of scan rate, temperature and oxygen concentration was investigated.

Scan rates will show if activation or concentration polarization control the corrosion process. If fast and slow scan rates overlap then activation polarization is controlling. If slow scan rates show a decrease in current density with respect to the fast scan rate then concentration polarization is controlling. Figure 78 shows the effect of scan rate when concentration polarization is controlling the corrosion process. Figure 41-Figure 50 show a decrease in current density with slower scans indicating corrosion is controlled by concentration polarization.
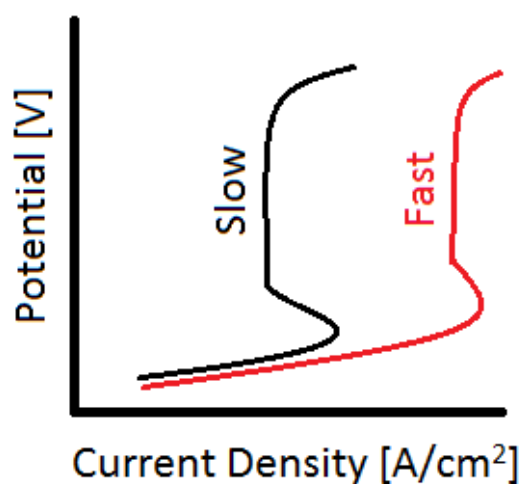
Figure 78 - Effect of scan rate

Tafel slopes, corrosion rates, and corrosion potentials were determined by Corrware. Listed in, Table 5 are the corrosion variables found under various conditions correlating to a scan rate of 0.6 V/hr. Constants were found using Corrware's analysis tool. The user selected the anodic and cathodic regions of the polarization curves to base the measurements on and Correware would output the Tafel slopes (β_a,β_c), corrosion current (I_{corr}) and the corrosion potential (E_{corr}) also referred to as OCP throughout this thesis.

Alloy	Oxygen Content	Temperature [^{o}C]	E_{corr} [V vs SCE]	I_{corr} [A]	β_a [mV]	β_c [mV]
S-135	De	80	-0.67	1.67E-05	33	-69
S-135	O	80	-0.64	1.69E-05	32	-71
S-135	O	20	-0.6	2.81E-05	76	-129
S-135	De	20	-0.57	1.30E-05	54	-121
UD-165	De	80	-0.61	6.50E-06	58	-79
UD-165	O	80	-0.63	3.79E-05	64	-82
UD-165	O	20	-0.56	1.23E-05	71	-241
UD-165	De	20	-0.63	5.60E-06	84	-92

Table 5 - Various variables found though analysis of polarization curves. De = Deaerated; O = Open air

Raising the temperature of a system will generally increase the corrosion rate. This is because raising the temperature increases the Tafel slopes (Equation 32) of the half reactions on the Evan's diagram, Figure 9 (7).

$$\beta_c = 2.3\frac{RT}{\alpha nF}$$

Equation 32 - Equation for slope of the cathodic reaction in the Evan's diagram - Where: R = Standard gas constant; T = Temperature; α = 0.5; n = number of equivalents exchanged; F = Faraday's constant

From Table 5 it is shown that temperature has minor effects on the corrosion current and corrosion potential for both UD-165 and S-135. For S-135 temperature had a large effect on Tafel slops, with the slopes decreasing almost by half by increasing the temperature from 20°C to 80°C. For UD-165 it appears that increasing the temperature had minor effects on Tafel slopes. For the UD-165 polarization curve open to air at 20°C showing -241 mV for β_c is likely an outlier and either a better curve should have been chosen or there was user error in selecting the linear region in the cathodic scan or a combination of the former and latter. See Figure 79, p89 for a diagram of the scatter in polarization scans.

Dissolved oxygen tends to increase the corrosion rate for steels, for temperatures below 80°C. Above 80°C the solubility of oxygen in water is decreased as the temperature is increased. At these high temperatures void of oxygen, the half-cell reduction reaction for the corrosion system changes from oxygen reduction to water reduction Equation 33 (35).

$$2H_2O + 2e^- \rightarrow H_2 + OH^-$$
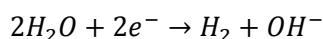
Equation 33 - Water reduction

From Table 5 it is shown that oxygen content has little influence on the Tafel slopes for both alloys. This is surprising because the reduction reaction has changed from reduction of oxygen to the reduction of water. Changing the reduction mechanism should have a large influence on the cathodic reaction rate, β_c. No explanation is given.

7.3.1 Polarization Curves Discussion

For every condition studied CV scans showed a cross over in the cathodic region. This means that pit growth and initiation may occur anywhere in the anodic scan.

It should be noted that much variability was involved in gathering the polarization data. A consistent OCP was not achieved sample to sample which influenced polarization curves. See Figure 79. Both S-135 and UD-165 had inconstant results. To have experimentally valid fatigue testing a surface treatment with no variation sample to sample is required.

The OCP changed sample to sample because samples were allowed to corrode and change the surfaces for 60 minutes before experiments were run. A range of 150 mV is too wide for experimental error and shows that the surfaces were inconsistent due to the procedure outlined in section 5.3.2 Polarization Experiments Procedure. Different surface conditions can change activation polarization and change Tafel slopes. This means that pitting may occur at different potentials sample to sample, which is highly undesirable.
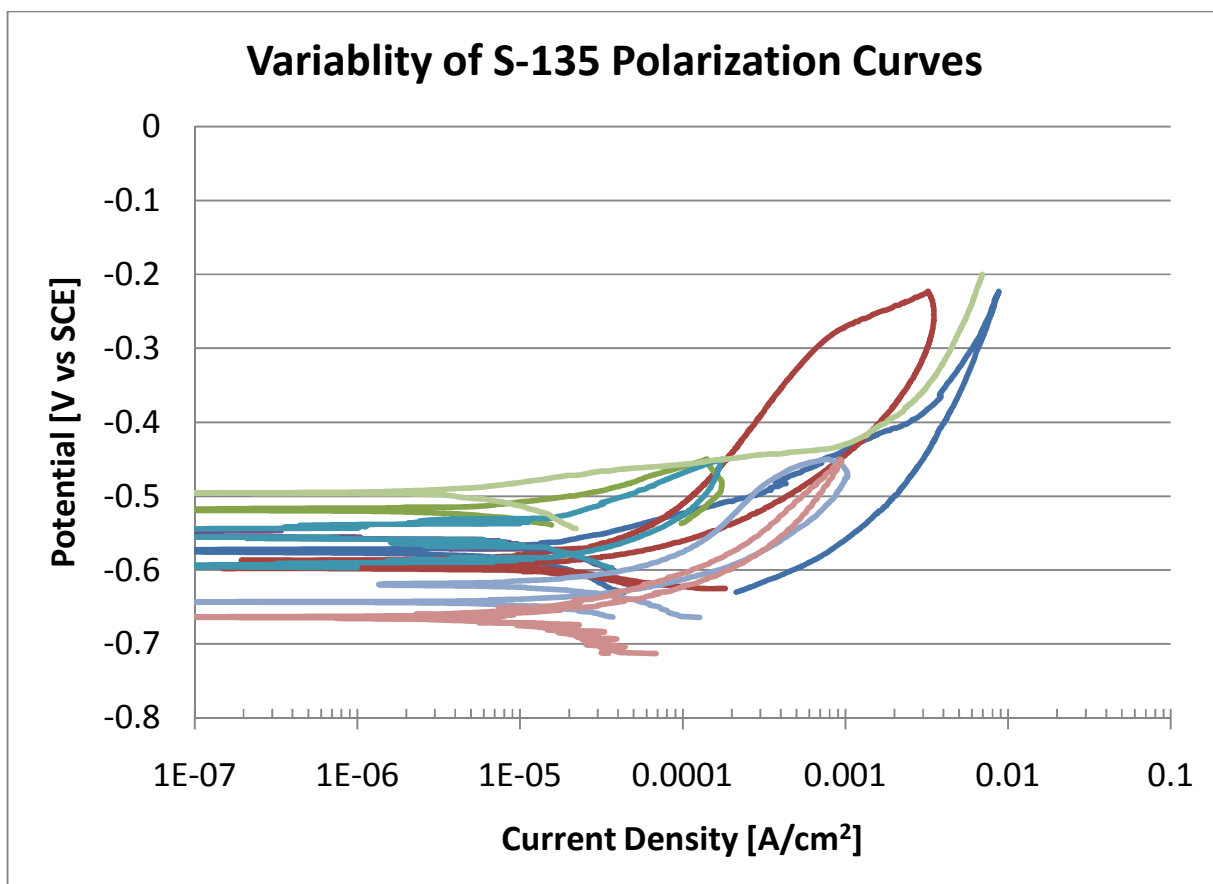
Figure 79 - Showing the variability of polarization data for S-135. 20°C in 6.71 M CaCl₂ solution open to air.

The inconsistency in OCP means that pitting potentials may change from sample to sample. This is undesirable as some samples may not pit and some may undergo mechanical passivation when held at one common "pitting potential". Because a pitting potential was chosen correlating to a current density of 0.001 A/cm² the pitting procedure was altered to hold the samples at 0.001 A/cm² rather than hold them at a specific pitting potential which may vary sample to sample.

7.4 Pit Growth Results Discussion

As shown in Figure 57-Figure 58, page 65, pit growth appeared nonexistent and each time the sample was held at the propagation potential new pits formed. Also new pits were formed during the propagation period, indicating samples had enough energy to pit. This suggests pitting may happen at any anodic polarization between the OCP and mechanical passivation.

Upon investigation it was found that potentiostatic methods were a non-ideal method to generate pits. Current fluctuated wildly sample to sample for potentiostatic testing. This means that pitting damage will not occur in a repeatable manner, see Figure 80. Also shown in Figure 80, some samples increase in current density while others decrease. Again this is undesirable as in some cases pit growth is observed while in other cases pit growth is not.
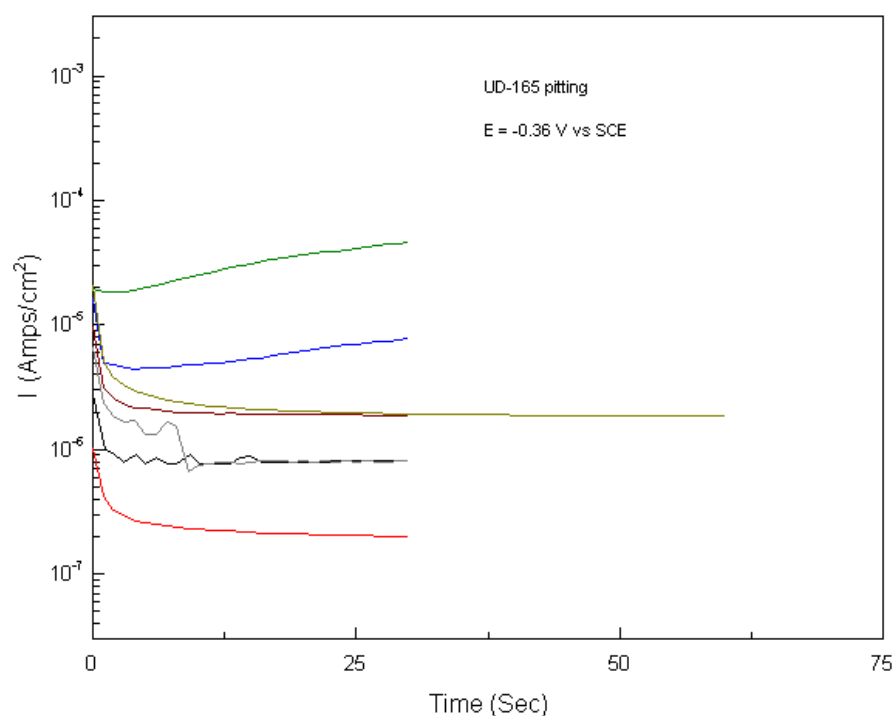
Figure 80 - Current against time plot for pitting UD-165 at -0.36 volts for 30 seconds to 60 seconds.

Having a few decades of variance when holding samples at a pitting potential is very undesirable. Fatigue testing should have as similar surface damage as possible sample to sample. This is unachievable though potentiostatic methods. Current controlled methods proved successful in limiting the sample to sample variance in surface damage. Shown below in Figure 81-Figure 82 are the potential against time plots for the fatigue samples. These galvenostatic (constant current) show small fluctuations in the voltages and consistent gradual decrease in potential without discontinuities. Increasing the pitting time from 30 seconds to 300 seconds helped to decrease variability as well.
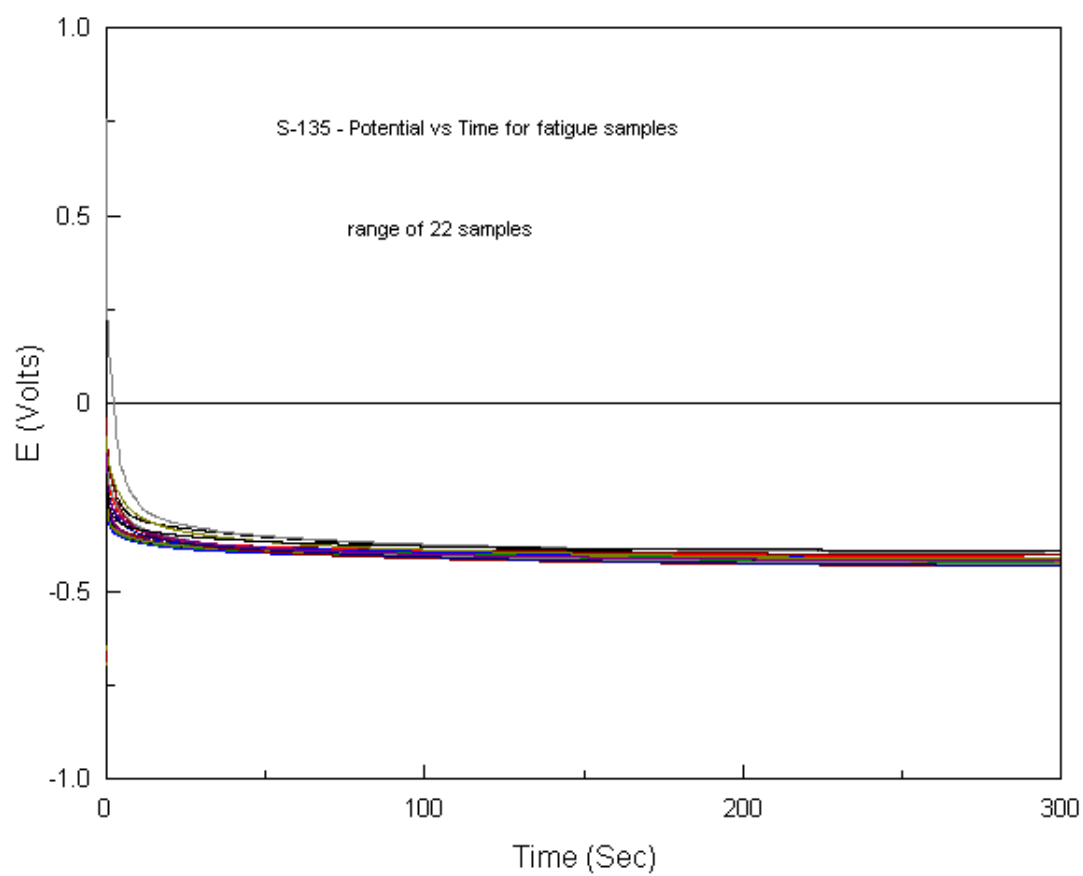
Figure 81 - Potential vs. time plot for fatigue specimens for S-135. Fatigue samples held at 0.001 A/cm^2.

UD-165 Potential vs time for fatigue speicmens
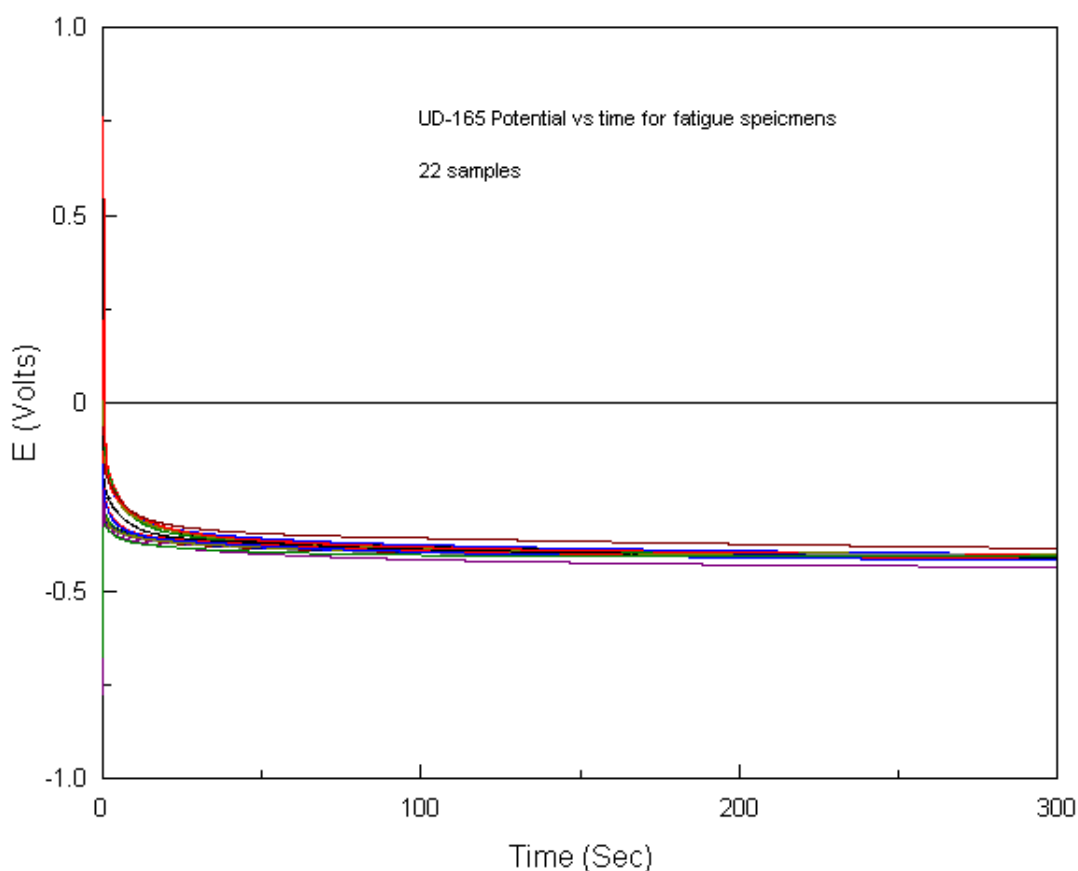
22 samples

Figure 82 - Potential vs. time plot for fatigue specimens for UD-165. Fatigue samples held at 0.001 A/cm^2.

To measure pitting damage optical profilometry was employed. It should be noted that there are limitations to the optical profliometer method. First the optical profliometer cannot measure subsurface features such as horizontal undercut pits, Figure 83. Also if corrosion products lay in the bottom of these pits the optical profilometer will only measure the depth of the pit to the corrosion product, not the true depth of the pit. If the optical profilometer cannot see the bottom of the pit then accurate measurements cannot be made. The crevices of pits are dark (light is not easily reflected) with corrosion products and cannot be easily cleaned due to their small size.

Figure 83 - Limitations of the optical profilometry method.

Due to the limitations of the optical profilometer it is possible that pit growth was occurring undetected. However this is unexpected. Zhou and Turnbull show for stainless steels pit growth occurs in a geometric manner increasing in depth from ~100 μm to 450 μm in 40 minutes of anodic polarization (36). If pit growth occurred in UD-165 and S-135 it would be expected to grow in a similar geometric manner found by Zhou and Turnbull.

Fractography indicates that pits depths up to ~ 20 μm can be generated using anodic polarization, however both optical profilometery and fractography show that pits deeper than 5 μm are abnormal.

7.6 Fatigue Results Discussion

It is apparent that pitting corrosion by anodic polarization dropped the fatigue life for UD-165. However statistical testing must be done to determine the probability the means for each surface treatment are indeed different. A confidence of 95% is considered statistically significantly different.

Statistical testing of the means of UD-165 by the Student's T method yielded that for a stress level of 825 MPa the mean's of pitted compared to virgin samples were different by a confidence of 95% and the means for 750 MPa were different by a confidence of 97% for the virgin and pitted states. For stress level of 700 MPa the confidence that the pitted and virgin means were different was 88%. No other stress levels showed statistically significant drops in fatigue life for virgin

against pitted states. While 88% confidence is less than 95% there is much scatter in the virgin data for 700 MPa it is expected that the confidence interval would increase with further data acquisition.

Statistical testing of the means for UD-165 by the Student's T method yielded no statistical significance in the drop of fatigue life for pitting corrosion followed by two weeks of ambient exposure against the virgin state.

Statistical testing of the means for S-135 by the Student's T method yielded no statistical significance in the drop of fatigue life for pitting corrosion or two week exposure against the virgin state.

Below in Figure 84 is shown the fatigue data normalized by the Ultimate Tensile Strength (UTS). Normalizing the data by dividing the stressing amplitude by the UTS of the material shows what percentage of strength in contributed.

Figure 84 - Fatiuge data normalized by ulitmate tensile strength. Arrows indicate samples which did not fail.

By normalizing the data by the Ultimate Tensile Strength (UTS), it is apparent from Figure 84, that UD-165 after pitting corrosion performs slightly worse than S-135 in both pitted and virgin states. No statistical studies were performed to confirm this as different stress levels were studied for S-135 and UD-165. Considering Figure 66, page 72, where pitting corrosion appears to put UD-165 fatigue life in line with the fatigue life of S-135, it is apparent that the increase in strength UD-165 provides can be nullified by exposure to simulated completion fluid (6.7 M $CaCl_2$) .

Fractography on UD-165 has shown there are at least 2 different methods of failure initiation due to pitting corrosion. At high stress levels, 825 MPa it is shown that failure initiated at tooling marks. Fracture surfaces show anodic polarization increased the depth of the tooling mark. For lower stress levels at 700 and 750 MPa pitting was apparent on fracture surfaces. Deepening of tooling marks and presence of pitting damage at crack initiation points indicate that pitting has the effect of increasing the local stress concentration, leading to faster crack initiation which leads to faster failure.

S-135 shows similar failure initiation to UD-165. Both pits and corrosion of tooling marks are present though fractography studies on S-135. However a statistically insignificant drop in fatigue life was measured for S-135.

Very little fractography was done on samples pitted and left in the laboratory for two weeks. No statistically significant drop in fatigue life was observed for theses samples on either alloy therefore the majority of time spent was investigating fracture surfaces of UD-165, as polished and with pitting corrosion.

Before conjectures upon why UD-165 showed a drop in fatigue life due to pitting while S-135 did not, it should be noted that tooling marks 3-8 μm in depth were present on all samples. Optical profilometry and fractography show that the majority of pits generated were less than 5 μm in depth. If pitting damage is less than the tooling mark then no effect of pitting is expected.

UD-165 is shown to be approximately 1.75 times more susceptible to pitting corrosion than S-135. This means that the chance a pit will form on UD-165 due to anodic polarization is approximately 1.75 times as likely then S-135 under the same anodic polarization. If the chance that a pit large enough to cause initiation is equal in both UD-165 and S-135 then UD-165 will have 1.75 times as many failure initiating pits than S-135. This is not exactly true because from

Figure 60, p67, UD-165 appears to have a pitting profile following a normal distribution around 2 μm where S-135 has a much more flat distribution, meaning that the chance of a pit "x" μm deep is not equal.

Looking at Figure 65, p2, at a stress level of 600 MPa the mean for the pitted samples preformed better than the mean for the virgin samples. This is not an anticipated result. While only three samples were fatigued for each surface treatment, the overlapping of virgin and pitted failure cycle ranges indicate that pits and corrosion damage due to anodic dissolution likely did not surpass the depth of tooling marks for S-135.

Given the increase in susceptibility of pitting corrosion for UD-165 due to anodic polarization, it is likely that pits and corrosion of tooling marks on UD-165 is due to the alloys increased ease to pitting where S-135 had a more difficult time forming pits. Hence the pitting damage on S-135 was not as detrimental as of UD-165.

Due to the lack of fractography studies on samples pitted and left in the laboratory for 2 weeks prior to fatigue, a definitive conclusion cannot be made as to why the statistically significant drop in fatigue life is erased for UD-165. One possible explanation is that corrosion further occurs and rounds tooling marks and pits, lessening the stress concentration.

While it is apparent that the strength advantage UD-165 shows can be nullified by simulated completion fluid it is unknown what corrosion fatigue effects may be observed. For this project samples were pitted and then fatigued. In oil wells drillstrings are fatigued and corroded at the same time. Important to note is that this project did not study the corrosion fatigue life of UD-165 or S-135. Because UD-165 is more susceptible to pitting corrosion than S-135, it is anticipated that UD-165 would perform worse under corrosion fatigue conditions than S-135 but no experimental evidence for this has been acquired.

8 Conclusions

It has been noted that industry drill pipes have been failing due to corrosion fatigue initiated by pitting corrosion (3). This project has revealed the susceptibility of pitting corrosion on HSLA drilling steels UD-165 and S-135 though immersion testing. This project has investigated the electrochemical behavior of these drilling alloys in corrosive completion fluids (6.7 M $CaCl_2$) though the use of polarization diagrams. Both UD-165 and S-135 showed active dissolution behavior followed by mechanical passivation under anodic polarization. Mechanical passivation was observed around current densities of 10^{-2} A/cm^2. Raising the solution temperature and voiding the solution of oxygen by argon bubbling had no effect on the passivity of the alloys. Pitting corrosion was verified by a hysteresis loop in cyclic voltammetry.

Pitting was accelerated by polarization methods. While pitting damage could be induced into both alloys, growth of the nucleated pits could not be achieved in a 6.7 M $CaCl_2$ 20°C, open air environment. New pits were observed during the propagation period.

UD-165 showed a higher pitting density than S-135. Nonmetallic sulfide inclusions are responsible for the initiation of pitting corrosion (7) (10) (11). The increased susceptibility to pitting corrosion is due to differences in inclusions between UD-165 and S-135. A non-exhaustive study on the inclusions was performed showing S-135 had inclusions rich in Mn and S, while UD-165 had Nb and C rich inclusions. UD-165 had many pull out inclusions with traces of Mn and S. It is well known that FeS accelerates pitting (13). It is conjectured that UD-165 may have slightly more FeS inclusions than S-135.

UD-165 showed a statistically significant drop in fatigue life for two of the measured stress levels for the pitted against virgin treatments. Fractography revealed that pitting corrosion as well as corrosion deepened tooling marks was at fault for crack initiation. This suggests corrosion acts in a mechanical manner, increasing the local stress concentration.

For S-135 a statistically significant drop in fatigue life was not found for any surface treatment. It is likely due to the decrease in susceptibility of pitting for S-135 that pits did not form deeper than tooling marks, hence showing less effect of corrosion damage.

Comparing the fatigue lifetime data for UD-165 and S-135 show that on a stress basis the fatigue life of UD-165 in the virgin state is superior to S-135, while the fatigue life of UD-165 in the pitted state is on par with S-135. Comparing the fatigue lifetime data for UD-165 and S-135

show that on a normalized stress basis the fatigue life of UD-165 in the virgin state outperforms S-135, while the fatigue life of UD-165 in the pitted state falls on the short end of S-135. This suggests that while UD-165 may be stronger than S-135, any potential strength benefits will be nullified once corrosion has occurred.

Bibliography

1. **Skeels. "**The Impact of HPHT on the Oil Industry." <u>DOT</u>, 2008, p. 1.

2. **Chandler, Jellison.** <u>World Oil.</u> Vol. 4, October 2006

3. **Macdonald, Bjune. "**Failure analysis of drillstrings". <u>Engineering Failure Analysis</u>, Vol. 14, 2006, p. 1641.

4. **Fanning.** API's History. *API Energy.* [Online] 2010 January. http://www.api.org/aboutapi/history/index.cfm.

5. **Videm, Kjeller. "**Report KR-149". <u>Institutt for Atomenergi.</u> 1974,

6. **Vaisberg, Vincke, Perrin. "**Fatigue of Drillsting: State of the Art." <u>Oil and Gas Science and Technology</u> , Vol. 7, 2002

7. **Jones.** <u>Principles and Prevention of Corrosion</u>, Macmillan Publishing Company, 1992. 0-02-361215-0.

8. **Pourbaix.** <u>Atlas of Electrochemical Eqlibria in Aqueous Solutions.</u> 0915567989.

9. **G46-76.** "Standard Guide for examination and evaluation of pitting corrosion" <u>ASTM</u>. 2009. 9780803163072.

10. **Wranglen. "**Pitting and Sulphide Inclusions in Steel". <u>Corrosion Science</u>, Vol. 14, 1974, p. 331.

11. **Gainer, Wallwork. "**The Effect of Nonmetallic Inclusions on the Pitting of Mild Steel." , <u>Corrosion</u> 1979, Vol. 35, p. 435.

12. **Ray. "**The Influence of Non-metallic Inclusions on the Corrosion Fatigue of Mild Steel." , <u>Corrosion Science</u>, Vol. 25, p. 171.

13. **Wranglen. "**Review Artical on The Influence of Sulphide Inclusions on the Corrodiblity of Fe and Steel." , <u>Corrosion Science</u> 1969, Vol. 9, p. 585.

14. **Flis.** <u>Corrosion of Metals and Hydrogen Related Phenomena</u>, Warsaw, Polish Scientific Publishers, 1991. 0444416854.

15. **Gerasimov, Shyvalo.** 1972, Zaschita Met., Vol. 8, p. 450.

16. **Heusler, Fisher.** 1976, Werkstoffe u. Korrosion, Vol. 27, p. 551.

17. **Seyes, Haute.** 1973, Werkstoffe u. Korrosion, Vol. 25, p. 663.

18. **Wranglen.** Corrosion and protections of metals. 0412260506.

19. **Scribner.** Corrware for Windows v2.1. southern pines, NC , 1998.

20. **Suresh.** Fatigue of Materials. Cambridge : Cambridge University Press, 1998. 0521570468.

21. **Hull, Bacon.** Introduction to Dislocations. 2001. 0750646810.

22. **Lu.** "Crack Initition and Early Propagation of X70 Steel in Simulated Near Neutral pH Groundwater." Corrosion, Vol. 62, p. 723.

23. **Murtaza.** "Corrosion Fatigue Short Crack Growth Behavior in High Strenght Steel.", Int. J. Fatigue, Vol. 18, p. 557.

24. **Akid.** "Fatigue Damage Accumulation: The role of Corrosion on the Early Stages of Crack Development.", Corrosion Engineering Science and Technology, 2006, Vol. 41.

25. **Wang.** "Role of Non-metalic Inclusions in Fatigue Pitting and Corrosion.", Corrosion, Vol. 52, p. 92.

26. **Spatz.** Basic Statistics: Tales of Distributions., Brooks/Cole Publishing Company, 1993. 0534192458.

27. **Anderson.** Fracture Mechanics Fundamentals and Applications., CRC Press, 2005. 0849316561.

28. **Paris, Erdogan.** "A Crictical Analysis of Crack Propagation Laws." Jounal of Basic Engineering, 1960, Vol. 85, p. 528.

29. **Prowse, Waymen.** "Effect of Environment on Fatigue Behavior of a Medium Carbon Steel." Corrosion,1974, Vol. 30, p. 280.

30. **G-5.** "Making Potentiostatic and Potentiodynamic anodic polarization measurements." ASTM 2009. Vol. 3.02. 978080319309-6.

31. **E-466.** "Conducting force controlled constant amplitude axial fatigue tests for metallic materials." <u>ASTM</u>, 2009. Vol. 3.01. 9780803163072.

32. **Payne, Chandler. "**Recent Key Advances in Drillstring Technology." <u>World Oil</u>, 2003,

33. **0b, E-18.** "Standard test methods for rockwell hardness of metallic materials." <u>ASTM</u> Vol. 3.01. 9780803163072.

34. **E-1019-08.** "Standard Test methods for determining Carbon, Sulfur, Nitrogen and Oxygen in steel, Cobalt, and Nickle alloys." <u>ASTM</u> 2009. Vol. 3.01. 9780803163072.

35. **Uhlig.** <u>Corrosion and Corrosion Control</u>, *3rd Edition.* 1985. 0471078182.

36. **Zhou, Turnbull. "**Influence of pitting on fatigue life of turbine blade steel.", <u>Fatigue Fract Engng Mater Struct,</u> Vol. 22, 1999, p. 1083.

37. **Bockris, Reddy.** <u>Modern Electrochemsitry.</u> New York , 1970.

38. **Wranglen.** <u>An Introduction to Corrosion and Protection of Metals</u>. London, Chapman and Hall, 1973.

Appendix A: List of Acronyms

MAH - Modified Avesta Head

SCE - Saturated Calomel Electrode

DIW - Deionized water

PD - Potentiodynamic

CV - Cyclic Voltammetry

PS - Potentiostatic

Basic salt - 0.7 M $CaCl_2$ 1.8 g $Ca(OH)_2$ per liter of DIW.

UTS - Ultimate Tensile Strength

SEM - Scanning Electron Microscope

EDS - Electron Dispersion Spectroscopy

MAH - Modified Avesta Head

OCP - Open Circuit Potential

HE - Hydrogen Embrittlement

SSC - Sulfide Stress Cracking

EAC - Environmentally Assisted Cracking

PAGS - prior austenite grain size

XRD - X-Ray Diffraction

LEFM - Linear Elastic Fracture Mechanics

PSB - Persistent Slip Band

Appendix B: List of Symbols

ΔG = Free energy

ΔG^o = Initial free energy

R = Standard gas constant

T = Temperature

e = Electric potential

e^o = Reduction potential for metal

m = mass reacted

I = current flow

F = Faraday's constant

n = number of equivalents exchanged

a = atomic weight

t = time

I_c = Cathodic current

I_a = Anodic Current

A_c = Cathodic area

A_a = Anode area

s = Standard deviation

N = number of samples

x_i = cycles to failure for specific sample

X = mean cycles to failure

X_1 = mean of population 1

X_2 = mean of population 2

N_1 = size of population 1

N_2 = size of population 2

K_I = stress intensity

Y = dimensionless constant dependant on loading mode and geometry

σ = characteristic stress

a = characteristic crack length

r = Distance from the crack tip

da/dN = crack growth rate

C = material constant

m = material constant

ΔK = stress intensity range

M = Atomic weight of Fe

n = number of electrons transferred

ΔH = Activation enthalpy

F = Faraday constant

I_{po} = Pit current

t_{pit} = time for pit to reach threshold size

a_0 = initial pit depth

ρ = density

β_a = Anodic Tafel slope

β_c = Cathodic Tafel slope